UNIVERSITÀ
DEGLI STUDI
DI PADOVA

Sede Amministrativa: Università degli Studi di Padova

Dipartimento di Fisica e Astronomia

SCUOLA DI DOTTORATO DI RICERCA IN FISICA

CICLO XXVI

Supernova remnants observed by the *Fermi* Large Area Telescope: the case of HB 21

Direttore della Scuola: Prof. Andrea VITTURI

Supervisore: Dott.Denis BASTIERI

Dott. Luigi TIBALDO

Dottorando: Giovanna PIVATO

Preprint

January 29, 2014

To my father Ugo

Abstract

Since their discovery, cosmic rays (CRs) are one of the most studied phenomena in the Universe. The origin of the spectrum, which extends for more than 12 orders of magnitude, is still debated. Up to $\sim 10^{15}$ eV, CRs are accelerated in the Galaxy, and Supernova Remnants (SNRs) are the most likely candidates to accelerate them. If an expanding SNR interacts with molecular clouds, particles accelerated in the expanding shock can produce high-energy photons, the observation of which can provide valuable information about the accelerated particles population. Of particular interest are combined γ-ray and radio observations: accelerated particles emit radio waves via synchrotron emission and γ rays via bremsstrahlung, inverse Compton and nucleon-nucleon interaction.

Thanks to its unprecedent angular resolution and sensitivity, the *Fermi Gamma-ray Space Telescope* is the γ-ray detector ideal for the study of extended structures in the Galaxy.

We present the analysis of *Fermi* Large Area Telescope γ-ray observations of HB 21 (G89.0+4.7). We detected significant γ-ray emission associated with the remnant: the flux above 100 MeV is $9.4 \pm 0.8(stat) \pm 1.6(syst) \times 10^{11}$ erg cm^2 s^{-1}. HB 21 is well modeled by a uniform disk centered at $l = 88.^\circ75 \pm 0.^\circ04, b = +4.^\circ65 \pm 0.^\circ06$ with a radius of $1.^\circ19 \pm 0.^\circ06$.

The γ-ray spectrum shows clear evidence of curvature, suggesting a cutoff or break in the underlying particle population at an energy of a few GeV.

We complement γ-ray observations with the analysis of the WMAP 7 yr data from 23 to 93 GHz, achieving the first detection of HB 21 at these frequencies. In combination with archival radio data, the radio spectrum shows a spectral break, which helps to constrain the relativistic electron spectrum, hence parameters of simple non-thermal radiation models.

In one-zone models multi-wavelength data favor the origin of γ rays from nucleon-nucleon collisions. A single population of electrons cannot produce both γ rays through bremsstrahlung and radio emission through synchrotron radiation. A predominantly inverse-Compton origin of the γ-ray emission is disfavored because it requires lower interstellar densities than the ones inferred for HB 21.

In the hadronic-dominated scenarios, accelerated nuclei contribute a total energy of $\sim 3 \times 10^{49}$ erg, while, in a two-zone bremsstrahlung-dominated scenario, the total energy in accelerated particles is $\sim 1 \times 10^{49}$ erg.

Sommario

Fin dalla loro scoperta, i raggi cosmici sono uno dei fenomeni piú studiati nell'Universo. L'origine del loro spettro, che si estende per piú di 12 ordini di grandezza, è ancora incerta e dibattuta. Fino ad energie dell'ordine di 10^{15} eV, si ipotizza che i raggi cosmici siano accelerati all'interno della Galassia, e che i resti di supernova siano i principali acceleratori. Espandendosi, un resto di supernova può interagire con le nubi molecolari presenti nel mezzo circostante, in questo caso le particelle accelerate possono produrre fotoni di alta energia la cui osservazione può fornire informazioni sulla popolazione dei raggi cosmici. Di particolare interesse sono le osservazioni combinate nella bade γ e radio: le particelle accelrate emettono nel radio tramite radiazione di sincrotrone, e nel γ tramite Bremsstrahlung, effetto Compton inverso e interazione inelastica nucleone-nucleone.

Grazie alla sua ottima risoluzione angolare e precisione spaziale, il Telescopio Spaziale *Fermi* è il rivelatore di raggi gamma ideale per lo studio di sorgenti estese.

La tesi presenta l'analisi effettuata con dati *Fermi* della sorgenet estesa HB 21 (G89.0+4.7). Riveliamo significativa emissione γ associata al resto di supernova: il flusso sopra 100 MeV è di $9.4 \pm 0.8(stat) \pm 1.6(syst) \times 10^{11}$ erg cm^2 s^{-1}. Dal punto di vista morfologico, l'emissione è ben modellata da un disco uniforme, centrato alle coordinate Galattiche $l = 88.^\circ75 \pm 0.^\circ04, b = +4.^\circ65 \pm 0.^\circ06$ di raggio $1.^\circ19 \pm 0.^\circ06$.

Lo spettro γ mostra un'evidente curvatura che suggerisce un taglio o un'interruzione dello spettro nella popolazione di particelle che generano lo spettro γ, ad energie di qualche GeV.

Insieme ai dati γ , sono stati inclusi anche dati provenienti dal radio usando 7 anni di dati raccolti dall'esperimento WMAP da 23 a 93 GHz,

che hanno portato alla prima osservazione di HB 21 a queste frequenze. Unendo tali dati ai quelli di archivio, si è potuto osservare come lo spettro radio presenti un'interruzione. Tale caratteristica aiuta a determinare lo spettro degli elettorni relativistici e, quindi, anche i parametri dei modelli di radiazione non termica.

Nei modelli di singola zona, i dati su piú lunghezze d'onda favoriscono un'origine dei raggi γ da collisioni nucleone-nucleone. Una singola popolazione di elettroni non può spiegare contemporaneamente sia l'emissione di Bremsstrahlung nel γ che quella di sincrotrone nel radio. L'effetto Compton inverso, invece, non può riprodurre bene lo spettro γ perché richiederebbe basse densità del mezzo interstellare, molto piú basse di quelle calcolate intorno a HB 21.

Quindi, nello scenario adronico, i nuclei accelerati forniscono un'energia di $\sim 3 \times 10^{49}$ erg, mentre in uno scenario in cui le zone di emissione di radio e γ siano diverse e l'emissione γ è dominata dal Bremsstrahlung, l'energia totale in particelle accelerate è di $\sim 1 \times 10^{49}$ erg.

Chapter 1

Introduction

Cosmic Rays (cosmic rays (CRs)) are very high-energy particles, mainly originating outside the Solar System. They produce showers of secondary particles that impact and penetrate the Earth's atmosphere and sometimes even reach the surface. They are composed primarily of high-energy protons and atomic nuclei, and, since their discovery in 1912 by Victor Hess, their origin is still debated. Their spectrum extends for $\sim$ 12 order of magnitude but, just a fraction of it (up to $\sim 10^{15}$ eV) is of Galactic origin.

In the Galaxy, one class of objects that can provide such big energy to the particles are Supernova Remnant (SNR). A SNR is the structure resulting from the explosion of a star in a supernova. The supernova remnant is bounded by an expanding shock wave, and consists of ejected material expanding from the explosion, and the interstellar material it sweeps up and shocks along the way. The connection between SNRs and CRs was first suggested by Walter Baade and Fritz Zwicky in 1943. The mechanism that can accelerate particle up to $\sim 10^{18}$ eV was first proposed by Enrico Fermi and it is known as "shock wave acceleration". Indeed, Enrico Fermi proposed in 1949 a model for the acceleration of CRs through particle collisions

with magnetic clouds in the interstellar medium. This process, known as the "Second Order Fermi Mechanism", increases particle energy during head-on collisions, resulting in a steady gain in energy. A later model to produce Fermi Acceleration was generated by a powerful shock front moving through space. Particles that repeatedly cross the front of the shock can gain significant increases in momentum. This process is known as "First Order Fermi Mechanism". The modeling of SNRs can provide useful information on the acceleration mechanism of CRs, the maximum energy reached and the physical processes involved.

In particular, combined observations in γ-ray and radio waveband can help to model the spectrum of SNRs: accelerated particles emit in radio via synchrotron emission and in gamma via bremsstrahlung, inverse Compton and nucleon-nucleon interaction.

The most recent and sensitive detector in the so-called *High Energy* (HE) γ-ray band is the *Fermi* Large Area Telescope (LAT) telescope. *Fermi* LAT provides a continuous scan of the sky from 20 MeV to 300 GeV with unprecedent sensitivity and angular resolution. These characteristics make *Fermi* LAT a good instrument to investigate the γ-ray sky and, in particular, extended sources in the Galactic plane.

This thesis is the product of the last three years in which I worked in the *Fermi* LAT collaboration, in particular performing the analysis of the region around HB 21, a mixed morphology SNR interacting with molecular clouds.

This class of SNRs are of particular interest for the study of the CRs acceleration processes. Molecular clouds can be target of the particle accelerated in SNR shock, revealing that SNRs can accelerate energetic particles.

This thesis is divided into two parts: the first one deal with general information about SNRs, *Fermi* LAT and the diffuse background.

In chapter 2 I will describe the common features of the SNRs, their classification and evolution. Particular emphasis will be given at the mechanism for the particle acceleration at the shocks and to the non-thermal emission processes in SNRs. This last section will be useful for the modeling of the source I will analyze using the *Fermi* data. Finally, I will describe how SNRs can accelerate Galactic CRs and the observation that confirm this hypothesis.

In chapter 3, I will give an overview on the *Fermi* LAT and its performance including the calculation of the systematic uncertainty due to effective area. I will also describe the high-level data analysis used for the thesis.

Finally, in chapter 4, I will describe the Galactic interstellar emission in the γ-ray band, including information on multi-wavelength tracers of interstellar matter and an overview of models of interstellar emission for the analysis of *Fermi* LAT data. A section will be devoted to the discussion on the alternative models the collaboration developed for the estimation of the systematic uncertainties due to the modeling of diffuse emission.

The second part of the thesis deals with the *Fermi* LAT analysis I performed during these three years. In particular, in chapter 5, using 4 yr of *Fermi* data, I will describe the morphological and spectral analysis on HB 21 whose goal is to determine the best spatial and spectrum shape that model the γ-ray emission. Then, using also 7 yr of WMAP data combined with archival radio data, I will describe how we model the multi-wavelength spectrum of HB 21.

Chapter 7 summarizes the results of our analysis on SNR HB 21 and discuss the future work on SNRs.

To help the reader, a list of acronyms (section Acronyms) and the table of contents (Contents) is present at the end of the thesis.

Part I

Supernova Remnants and the *Fermi* Large Area Telescope

Chapter 2

Supernova Remnants

This chapter is devoted to the description of SNRs. SNRs are structures resulting from the explosion of stars in supernovae (SN). SNRs are delimited by the expanding shock waves. They consist of ejected materials and by all the interstellar medium the shock sweeps up and accelerates during the expansion. Starting from a brief history of the discovery of these objects, I will move to the classification looking at the morphological structure of SNRs. Then I will describe, in section 2.2, the evolution of a shell type SNR and, in section 2.3, I will describe the particle acceleration processes and the physical information one can obtain from the modeling. In section 2.4, I will explain the mechanism that produce the particle spectrum and i will discuss the energetics required to assert that SNR are the main candidates to explain the origin of Galactic cosmic rays (2.5).

2.1 Supernova remnants

The first evidence of SNRs consisted in observations of optical nebulae associated with historical and known SN. A big step toward the understand-

ing of these objects was made when radio interferometry developed in the early 1950's. With this technique, populations of extended objects with non-thermal radio spectra were discovered. The spectrum of these sources was determined to be a power-law ($S_\nu \propto \nu^\alpha$) with index $\alpha \sim -0.5$. A power law distribution cannot be generated from particles in thermal equilibrium which is described by Planck's law. In 1953, Shklovskii associated the synchrotron unresolved radiation with remnants of unseen SN (Shklovskii, 1953). The most complete radio catalog of SNRs was made in 2009. The Green (2009) catalog provides the radio features of almost 250 Galactic SNRs. According to Shkolovskii (Reynolds, 2008), SNRs are sources of non-thermal populations of electrons with a power-law distribution in momentum. Standard synchrotron physics relates a power law electron population with the photon population. If the first has a distribution $N(E) = kE^{-s}$, the latter is described with a power law with index $\alpha = (1 - s)/2$. From observations, the photon index, α, is close to -0.5, so $s \sim 2$, close to 2.7 which is the slope observed for CRs at GeV energies. The discrepancy suggests that SNRs may be the sources of CRs, once the effect of diffusion to the Earth which soften their spectrum, is taken into account.

In 1949, Fermi proposed collisionless shock acceleration as a mechanism to accelerate charged particles: it consisted in collisions through magnetic mirror between charged particles and interstellar clouds. This idea was proposed for SNRs as well, but it presents a number of problems for this application: the acceleration is too slow, and the spectrum depend on a free parameter, the escape timescale (Reynolds, 2008). For further details on acceleration of charged particles see section 2.3.1.

In 1981 Reynolds and Chevalier proposed that diffusive shock acceleration (DSA) could accelerate electrons to the synchrotron-X-Ray-emitting energy

in the shell of an historic SNR, the SN 1006 AD to explain the absence of features in the X-ray spectrum. In 1983 Lagage and Cesarsky calculated the maximum energy attained by DSA to be almost 10^{14} eV.

The ASCA satellite resolved SN 1006 AC showing that the spectral features of this source vary with position. In the late '90s, two synchrotron dominated shell SNRs were discovered: RX J1713.7-3946 (Koyama et al., 1997; Slane et al., 1999) and Vela Jr (Aschenbach, 1998; Slane et al., 2001).

Esposito et al. (1996) published a list of possible associations between known SNRs and unidentified Galactic-plane γ-ray sources, observed with the EGRET space telescope. The *Fermi* LAT improves the situation because it has a better angular and energy resolution compared with the previous space born γ-ray experiment.

The discovery of the TeV photon occurred in the early 2000s. Although earlier γ-ray satellites such as SAS-2 and COS-B had imaged the γ-ray sky with angular resolution of few degrees and located several discrete sources, predictions of γ-ray emission from shell SNRs began in earnest under EGRET stimulus (Reynolds, 2008). Enomoto et al. (2002) reported the emission from G 347.3-0.5 emission with the CANGAROO air-Cherenkov telescope in Australia and Aharonian et al. (2007) the emission from G 266.2-1.2 with the HESS experiment in Namibia.

SNRs are the most likely candidates to accelerate Galactic CRs: observations of these objects can provide valuable information on such a process. In particular, high-energy γ-ray emission can pinpoint the presence of energetic leptons or ions, constraining the acceleration efficiency and the maximum energy of accelerated particles.

2.1.1 Classification of Supernova remnants

The explosion of a SN, progenitor of a SNR, deposits its energy in the nearby medium in a shell. Both initial conditions (such as mass and progenitor) and environment (density enhancements and Rayleigh-Taylor instabilities) could affect the morphology of the remnant.

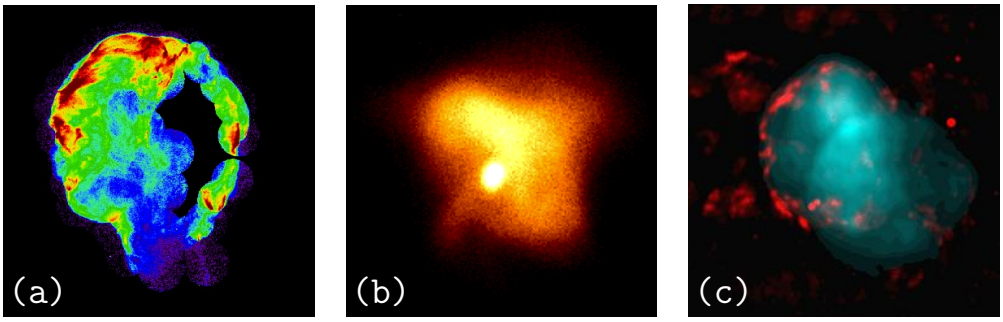

Figure 2.1: Three different examples of SNRs: a) Cygnus Loop is an example of shell-like SNR. Image credit: Levenson et al. b) Crab Nebula is an example of filled center SNR. Image credit: S. L. Snowden (USRA, NASA/GSFC) c) IC443 is a mixed morphology SNR. Image courtesy of Jonathan Keohane. for the description of each type, see the text.

From this brief description it is clear that a number of different morphological types of SNRs are possible looking at the emission of these object in different wavebands. The original classification is based on optical emission fatures of SN. There are two big classes of SN: Type I and Type II. The first includes object in which there is no H line at the maximum light; in the latter, sources have this features. SN type I have a sub-classification depending on the presence of other emission lines: in type Ib there is the lack of Si II (6150 Å) line and in type Ic the He line is not present. Type II SN has a sub-classification, too. Two of three classes are characterized by features of source lightcurves after maximum light: type IIP has a plateau and type IIL

a linear decline after maximum light. The last type is IIn which presents narrow lines emission features.

This classification reflects the origin of SN. Type Ia is the so called thermonuclear SN: it comes from nuclear burning of the carbon-oxygen white dwarf to iron-peak elements that produce $\sim 10^{51}$ erg. Type Ib, Ic and II all come from explosion of massive stars powered by gravitation (core collapse). In particular, for type Ib cores have eject H envelopes and, for type Ic, both H and He envelopes have been ejected. Type II SN come from stars with mass $\sim 8\ M_{\odot}$ which explode in a red supergigant (type IIP) with the possibility of lower-mass H envelopes (type IIL).

Considering X-ray and radio emission, SNRs can be divided into three categories: *shell type*, *Crab-like* (also known as *plerions* or *filled center*) and *mixed morphology* (also known as *composite*).

In a shell-like SNR the shock wave plows through the space and heat any material along its path producing shells of hot gas. An example of shell like SNR is the Cygnus Loop shown in figure 2.1a.

A Crab-like SNR is a shell-type SNR but has a pulsar in the middle. The pulsar produces a Pulsar wind nebula (PWN) detectable as non thermal X radiation filling the entire shell. The name derives from the Crab nebula (figure 2.1b), the remnant of the supernova explosion of 1054 AD reported in Chinese annuals. The emission appears more similar to a blob than to a shell: this is due to the high energy jets from the central pulsar.

Finally, mixed morphology SNR appears shell like in radio and filled center in X-ray. The X-ray emission is due to the palsma of tehrmal electrons, in contrast to the non-thermal origin of the plerions. Two examples of this type of SNR are IC 443 (shown in figure 2.1c) and HB 21, whose analysis I will develop in chapter 5.

2.2 The evolution of Supernova remnants

The progenitor is important in determining the evolution of the SNR; the main quantities that are relevant are initial density and velocity profile. Most of this section is taken from Reynolds (2008) Now on I will consider spherically symmetric Core Collapse (CC) explosion. Inhomogeneities on small scales should not produce large departures from results assuming spherical symmetry, but major inhomogeneities[1] would not be well described by these results. The roughly spherical shape of most of young SNRs indicates that such departures do not typically dominate the gross evolution. After a first time interval in which the energy of explosion drive the expansion, the object is freely expanding and ejecta density profile can be described by: $\rho \propto r^{-n}$ with $n \sim 10 - 12$. CC progenitor modifies the surroundings with mass loss episodes or, at least, with fast wind during the main-sequence lifetimes and in red supergigant (RSG) with a slower, denser wind. This, in turn, produce circumstellar medium (CSM) density profile $\rho \propto r^{-s}$ with $s = 2$. This behavior is confirmed by X-ray and radio emission observations. CSM and ejecta could be in-homogeneous but, at small scales there are no deviations from spherical symmetry approximation.

If the shock is a discontinuity in flow velocity, which, otherwise, is constant with value u_1 and u_2 in up- and downstream respectively one can write:

$$\frac{u_2}{u_1} \equiv \frac{1}{r_{comp}} = \frac{\gamma - 1}{\gamma + 1} + \frac{2}{\gamma + 1}\frac{1}{\mathcal{M}^2} \tag{2.1}$$

$$\frac{p_2}{p_1} = \frac{2\gamma}{\gamma + 1}\mathcal{M}^2 - \frac{\gamma - 1}{\gamma + 1} \tag{2.2}$$

where $r_{comp} \equiv \rho_2/\rho_1$ is the compression ratio, $\mathcal{M} \equiv v/c$ the Mach number, γ the ratio of specific hits and p the pressure. For the common case $\gamma = 5/3$

[1] such as jet-driven SN or circumstellar medium (CSM) in equatorial disks

and $\mathcal{M}^2 \gg 1$, one can obtain:

$$\begin{aligned} r_{comp} &= \frac{\rho_2}{\rho_1} = \frac{\gamma+1}{\gamma-1} = 4 \\ p_2 &= \frac{2\rho_1 u_1^2}{\gamma+1} = \frac{3}{4}\mu_1 m_p n_1 u_1^2 \\ kT_2 &= \frac{3}{16}\mu_2 m_p u_1^2 \end{aligned}$$

where μ is the mean mass particle and n_1 the upstream particle number density. Note that these relations are valid only if energy loss owing to radiation is negligible. Ejecta with mass M_{ej} with initial velocity $\left(\frac{2E_{SN}}{M_{ej}}\right)^{1/2}$ of the order of $10^3 - 10^4$ km s^{-1} has high Mach number $\mathcal{M} \gtrsim 10^3$, so a blast wave is formed.

Behind the blast wave, ejecta expand almost freely and cool adiabatically; the velocity behaves as an Hubble low: $v \propto r$. Then, SN blast wave encounters modified CSM or undisturbed Interstellar Medium (ISM) and the shock slows down and the interior ejecta decelerates. This ejecta could be then reheated by an inward-facing shock: this phase is known as *ejecta-driven* phase. The reverse shock has a velocity up to ~ 1000 km s^{-1} and it is responsible for X-ray emission from the ejecta. If the reverse shock is spherically symmetric, the contact between the shock-heated ISM or CSM and shock-heated ejecta presents a discontinuity (across which p is constant). These two distinct structures, persist until the mass of the swept up is greater than the mass of the ejecta: in this case, the two structures evolve self-similarly. The behavior during the evolution is well described by the so called *Sedov self-similar* solution for adiabatic point explosion in a uniform medium of negligible pressure. In this case, the radius of the blast-wave is given by $R \propto t^{(n-3)/(n-s)}$ where $n = 10 - 12$ and $s = 2$ in CC case.

The time t_{ch} necessary to move from ejecta-driven to Sedov phase considering M_{ej} mass of the ejects, E the explosion energy and ρ_0 the ambient

density is found to be:

$$t_{ch} = E^{-1/2} M_{ej}^{5/6} \rho_0^{-1/3}. \tag{2.3}$$

Sedov phase ends when the shock is slow enough that the radiative cooling takes place and adiabatic approximation breaks down. Also in this condition, it is possible that some parts of the remnant could cool before the others. Also interior may still remain hot enough to provide pressure (pressure-driven snowplow).

For fully ionized, cosmic-abundance gas, the gas volume cooling function can be approximates as: $\Lambda(T) = 10^{-16} T^{-1}$ erg cm^3 s^{-1}. using that approximation, at the transition to radiative evolution t_{tr}, the radius R_{tr} and the mass of the ejecta M_{tr} are given by:

$$t_{tr} = 2.9 \times 10^4 E_{51}^{4/17} n_0^{-9/17} \text{ yr} \tag{2.4}$$

$$R_{tr} = 19 E_{51}^{5/17} n_0^{-7/17} \text{ pc} \tag{2.5}$$

$$M_{tr} = 10^3 E_{51}^{15/17} n_0^{-4/17} M_\odot. \tag{2.6}$$

Note that, most important phases for particles acceleration are pre-Sedov and transition to the Sedov phase. In the pre-Sedov phase, the maximum energy rises rapidly as the shock velocity remains high and deceleration is small (for details on maximum energy see section 2.3.3). After a transition at a time of order t_{ch} (given in the 2.3), the rate of increase slows.

2.3 Particle acceleration in SNRs

Radio emission features can be explained with the presence of ultra-relativistic ($E \sim 10^4 m_e c^2$) electrons. The radio brightness is too high to arise from compression of intestellar electrons and magnetic field (Reynolds, 2008). The

process that explains the presence of high energy electrons in SNRs is the diffusive shock acceleration and particle scattering across the shock of the remnant.

2.3.1 Diffusive shock acceleration

The description and hysitry of DSA are taken from Baring (1997). Fermi (1949) first postulate that CRs could be produced via collisionless shock acceleration in interstellar clouds. The elegance of Fermi's idea is that, when particles are confined this diffusive process naturally produces power-law CR distribution.

It was realized that shocks in plasma could also provide diffusive acceleration in an efficient manner, tapping the dissipative potential of the flow discontinuity by transferring the shock's kinetic energy to non-thermal populations both upstream and downstream of the shock, at the same time as heating the downstream gas. This last process is the so called diffusive shock acceleration (DSA) or *first-order Fermi* mechanism.

The modern era of shock acceleration theory began with a collection of papers in 1977-78 (Krymskii, 1977; Bell, 1978; Axford et al., 1977; Blandford and Ostriker, 1978).

DSA at SNR blast waves is the favored production mechanism for the production of Galactic cosmic-rays. It can naturally explain the formation of a power-law spectrum by a shock wave.

To have a DSA two components are needed: the shock, which is a velocity jump, and a diffusion center, such as the magnetic field waves.

A shock forms when some material propagates in a medium with speed higher than the reaction speed of the medium itself. The natural travelling speed of a perturbation in a medium depends on its density ρ and pressure

P and it is given by the sound speed:

$$c_s = \sqrt{\frac{\partial P}{\partial \rho}}. \tag{2.7}$$

Using the polytropic equation state

$$P \propto \rho^{\gamma} \tag{2.8}$$

it becomes:

$$c_s = \sqrt{\frac{\gamma P}{\rho}} = \sqrt{\frac{\gamma k_b T}{\bar{m}}} \tag{2.9}$$

where T is the temperature of the medium, $\bar{m}$ the mean atomic mass, and k_B the Boltzmann constant. If something is travelling at a velocity higher than the speed velocity of the medium, sounds waves steepen to form a shock wave that is a discontinuity in the hydrodynamical profile. The shock compress and heats the medium so it can respond to perturbation. The strength of the shock is measured by the ratio between its proper speed and the local speed of sound, and it is called Mach number.

The Fermi mechanism always applied to *collisionless* shock so to all those non-linear preturbancies that have energy and momentum transfer between particles mediated by plasma processes, with Coulomb scattering negligible. To understand this process we have to consider a flow defined by speeds u_1 and u_2 (with $u_2 < u_1$) on the two different sides of the shock as shown in figure 2.2. In the rest frame of the shock, we consider particles speed v_0 initially in the upstream side of the shock. These particles diffuse around via collisions with magnetic turbolence of the plasma until they cross the shock and move downstream. This kind of diffusion tends to isotropize the angular distribution of the particles in the frame in which the upstream plasma is at rest. After a period, in which the particles interact with the upstream medium, now they collide with magnetic turbolence that is associated with

the downstream plasma. If also this plasma tends to isotropize the particles, this populatin sees a plasma moving towards it upon arrival downstream. The velocity of this flow is $\sim |u_1 - u_2|$. The process of quasi-isotropization leads to an increase in average of the particle speed in the rest frame of the shock interface.

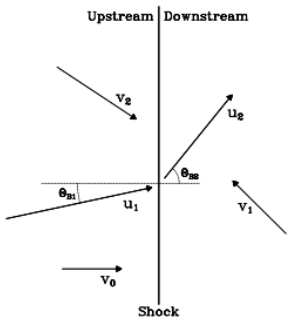

Figure 2.2: A schematic depiction of of a particle motion in a shock. The plasma flow speed are: u_1 in the upstream region, and u_2 in the downstream. it is also shown the mean accelerated particle speed v_i after i shock crossing. Speeds after the shock crossing are ordered as: $v_0 < v_1 < v_2 < ... < v_i$. (from Baring, 1997)

Some of the particles will return to upstream side of the shock, and these will see the upstream plasma moving towards them. Subsequent diffusion back and forth across the shock leads to increase in particle speed, so many shock crossing afford significant acceleration. For non-relativistic particles, the velocity increase is proportional to $\sim |u_1 - u_2|$. This mechanism is known as first-order (or diffusive) shock acceleration.

Second-order Fermi acceleration consists in the same process by random shocks, which results in a velocity increase proportional to $|u_1 - u_2|^2$. in both cases, first and second order, the diffusion yield to a power-law distribution of the particles. The second-order Fermi acceleration is a minor contribution

in dynamics of SNRs. To estimate when this process becomes dominant we can consider the acceleration time to energy E. For a stochastic acceleration and DSA it assume the form (Reynolds, 2008):

$$\begin{aligned} t_{acc}(stoch) &\sim \left(\frac{\lambda_{mfp}}{c}\right)\left(\frac{v_A}{c}\right)^{-2} \\ t_{acc}(DSA) &\sim \left(\frac{\lambda_{mfp}}{c}\right)\left(\frac{u_{sh}}{c}\right)^{-2} \end{aligned} \tag{2.10}$$

where v_A is the Alfven speed, λ_{mfp} the scattering mean free path and $\mathcal{M}_{A2} \equiv u_{sh}/v_A$ is the Alfven Mach number of downstream flow. The ratio of the acceleration rates is:

$$\frac{t_{acc}(DSA)}{t_{acc}(stoch)} \propto \mathcal{M}_{A2}^{-2}.$$

Under normal conditions, DSA is more rapid so we assume that it is the primary mechanism to produce energetic charged particles in SNRs shocks.

Although the power-law index of the accelerated particles is independent of the shock obliquity, the acceleration efficiency is strongly dependent on the angle θ_{B1} that the upstream magnetic field makes with the shock normal (Baring et al., 1993).

To understand the importance of the obliquity in DSA an analysis of particle scattering through the shock front is necessary.

2.3.2 Particle scattering

We consider particle scattering with an energy dependent mean free path λ_{mfp}. Additional condition for this simplify description of the particle scattering, is that the scattering is resonant so we can express λ_{mfp} as a function of the gyroradius (r_g) in the mean magnetic field (Reynolds, 2008): $\lambda_{mfp} = \eta r_g = \eta\left(\frac{E}{eB}\right)$ where the last sentence is valid in ultra-relativistic conditions ($E \gg mc^2$) and η is the gyrofactor.

Resonant scattering from circular polarized magneto-hydrodynamic (MHD) waves (Alfven waves) with frequency equal to the gyrofrequency (Ω_g), will result in diffusion. Given the gyrofrequency of a particle with Lorentz factor γ, $\Omega_g = eB/\gamma mc$, the resonance condition can be written as:

$$\Omega_g = \mathbf{k} \cdot \mathbf{v} \tag{2.11}$$

so more energetic particles need longer λ to scatter. If $\mathbf{k} \perp \mathbf{v}$ no resonance is possible, so to scattering to 90°is not possible, even if it is observed. Probably 90°takes place using other physical processes (Reynolds, 2008).

The scattering results in an effective mean free path depending on gyroradius and in a diffuse coefficient $\kappa(x, E)$ for a particle with energy E. The expression of κ along the direction of the magnetic field is given by:

$$\kappa_{\parallel} = \kappa(x, E) = \frac{1}{3}\lambda_{mfp}c = \frac{1}{3}\eta\frac{Ec}{eB}. \tag{2.12}$$

The diffusion coefficient $\kappa_{\perp}$ arises from the assumption that a particle is displaced one gyroradius perpendicular to field and lies with every parallel scattering. In this condition, $\kappa_{\perp}$ has the form (Reynolds, 2008):

$$\kappa_{\perp} = \frac{\kappa}{1 + (\lambda_{mfp}/r_g)^2} \equiv \frac{\kappa_{\parallel}}{1 + \eta^2}. \tag{2.13}$$

If θ is the angle formed by the diffusion coefficient with the magnetic field B, the coefficient can be decomposed in the two perpendicular directions: $\kappa = \kappa_{\parallel}\cos^2\theta + \kappa_{\perp}\sin^2\theta$. For shock acceleration process, we are interested only in scattering along the shock normal.

A common quantity taken into account is the *obliquity* θ_{Bn} which is defined as the angle between the shock normal and the upstream magnetic field. An interesting case is when $\theta_{Bn} \sim 90°$: in this condition we have a perpendicular shock. The gyromotion bring back and forth particles from the shock even in the absence of scattering. This mechanism is called *shock drift*

acceleration: particles gain energy as result of grad B drift perpendicular to the shock and along induced electric field $\mathbf{E} = -\mathbf{u_1} \times \frac{\mathbf{B}}{c}$ (Reynolds, 2008).

2.3.3 Acceleration rates and maximum energies

The length scale for particle diffusion ahead of the shock can be calculated as κ/u, so the timescale can be written as κ/u^2. More in detail, we can calculate the time to accelerate a particle from momentum p_i to p (Reynolds, 2008):

$$\tau_{acc} = \frac{3}{u_1 - u_2} \int_{p_i}^{p} \left(\frac{\kappa_1}{u_1} + \frac{\kappa_2}{u_2} \right) \frac{dp'}{p'}. \tag{2.14}$$

Using equation 2.13, for a shock with compression ratio r_{comp} and under the additional assumption of $\kappa_1 = \kappa_2$ and $p \gg p_i$ the previous equation becomes (Reynolds, 2008):

$$\tau_{acc}(p)(parallel) = \frac{3\kappa(p)}{u_1^2} \frac{r_{comp}(r_{comp}+1)}{r_{comp}-1}. \tag{2.15}$$

Considering scattering non-isotropic obliquity plays an important role in the estimation of the acceleration time:

$$\tau_{acc}(\theta_{Bn}) = R_J \tau_{acc}(\theta_{Bn} = 0) \tag{2.16}$$

where $R_J < 1$ is given by (Reynolds, 1998):

$$R_J = \frac{\kappa_1(\theta_{Bn,1})/u_1 + \kappa_2(\theta_{Bn,2})/u_2}{\kappa_1(0)/u_1 + \kappa_2(0)/u_2}$$

is independent on E because κs depend all on E.

The estimation of the maximum energy is important for understanding CR origin and the high-energy emission from SNRs. The maximum energy reached is directly connected with the age limitation: there is a finite amount of time in which the SNR can accelerate particles. The three main processes the limit the age are:

1. finite size of the remnant
2. radiative losses
3. increase of the diffusion coefficient, and so the particle can escape upstream.

In any of this case, the particle distribution function results in a power law with exponential cutoff at some energy E_{max}. For each of the different limit on age, we can estimate a different maximum energy (Reynolds, 2008):

$$E_{max}(age) \sim 0.5 u_8^2 t_3 B_{\mu G} (\eta R_J)^{-1} \text{ TeV} \quad (2.17)$$

$$E_{max}(loss) \sim 100 u_8 (\eta R_J B_{\mu G})^{-1/2} \text{ TeV} \quad (2.18)$$

$$E_{max}(escape) \sim 10 B_{\mu G} \lambda_{17} \text{ TeV} \quad (2.19)$$

where $u_8 \equiv u_1/10^8$ cm s^{-1}, $t_3 \equiv t/1000$ yr, $\lambda_{17} \equiv \lambda_{max}/10^{17}$ cm and B the upstream magnetic field. All the discussion above is intended for E_{max} obtained from a gradual drop-off of emission. Synchrotron X-rays emission can be produced at $\nu \gg \nu_{max}(E_{max})$ (Reynolds, 2008).

$E_{max}(age)$ rises rapidly in the pre-Sedov phase. After the transition, at the time t_{ch}, we ca re-write this maximum energy as (Reynolds, 2008):

$$E_{max}(age) = 5 E_{max}(age)(t_{ch}) \left(1 - \frac{t}{t_{ch}}\right)^{-0.2}$$

which is valid only for particles present from the earliest time.

Note that single-particle approach is valid for every shock geometry.

This is considered the main acceleration process in SNRs. But the SN material ejected during the explosion moves with a high velocity. The forward and backward shocks are formed due to ejecta interaction with a circumstellar medium. The circumstellar gas is compressed at the forward shock while while the backward shock propagates into the supernova ejecta.

This phenomenon is not considered in the linear DSA described above but has to be taken into account using nonlinear treatments of DSA. nonlinear DSA (NLDSA) have predicted that at strong shocks a significant fraction of the shock kinetic energy is transferred to CRs. This induces highly nonlinear back-reactions from CRs to the underlying flow, creating a shock precursor (e.g., Amato and Blasi, 2006; Vladimirov et al., 2006; Kang and Jones, 2007) that compresses inflowing plasma upstream of the dissipative subshock. As reported in Kang et al. (2012), the acceleratin in the SNRs shock, considering the NLDSA, was faster at earlier times, when the shock speed is faster.

2.3.4 Injection and magnetic field amplification

The mechanism for which few particles are promoted to the energy of the shock is known as *injection problem*. The shock layer is expected to be few thermal ion gyroradii thick; ions have only few times the mean energy in order to have gyroradii larger than the shock thickness. Particles scatter back and forth the shock and become injected and this process produces thermal leakage.

For electrons gyroradius is always too small to let the particles injected. Another mechanism is responsible to the injection of electrons. This has to depend on remnant parameters such as upstream obliquity or neutral fraction. These parameters have a direct consequence on X-ray TeV emission. A suggested process there is the plasma instabilities but there are still unresolved problems (Reynolds, 2008).

Shocks in SN and SNRs amplify pre-existing magnetic field. This leads to streaming instabilities of upstream CR in parallel shock. Also in this case, there are some unknown features such as: the dependence of shock obliquity, the persistence of oscillation in B as a field with non-zero mean,

the dependence of effect on shock speed or the presence of upstream neutrals (Reynolds, 2008).

Caprioli et al. (2008) found that, starting from an evaluation of magnetic field amplification, the compression ratio can be calculated. This leads to a value of 6-10 for modified DSA, much smaller than that assumed considering standard theory, which predicts a value of 4. This estimation is in agreement with some observations which suggest values between 7 and 10 Völk et al. (see 2005).

2.4 Non-thermal radiation processes in SNRs

Four basic radiative processes are capable of producing emission in SNRs. Three are leptonic: synchrotron radiation (in radio frequencies, described in section 2.4.1), non-thermal bremsstrahlung (section 2.4.3) and Inverse Compton (IC) scattering (section 2.4.2). The most common mechanism in SNRs which involves hadrons is the decay of π^0 mesons produced by scattering of protons with cosmic-ray ions (section 2.4.4). This is the only hadronic mechanism taken into account for the SNRs modeling of the spectrum. Last two leptonic emission mechanisms and the hadronic one produce radiation in γ-rayband. Most of the material used in this chapter is taken from (Longair, 2011), for section2.4.1, (Vietri, 2006), for section 2.4.3, and (Reynolds, 2008) for sections 2.4.2 and 2.4.4.

2.4.1 Synchrotron radiation

Synchrotron radiation is produced by charged particles, usually electrons or positrons with relativistic velocities, that are deflected in a magnetic field B. Higher the speed, lower the wavelength of the radiation emitted that usually

has the peak in the radio frequencies. To derive equations for synchrotron luminosity (i.e. radiated power), first consider the case of a single particle of mass m, energy $E = \gamma mc^2$ and charge e moving with velocity v in a uniform magnetic field B.

The trajectory of this particle makes an angle of α_p (the so-called pitch angle) with the direction of magnetic field. The particle's trajectory descrive an helix or a spiral along the magnetic field along the field line, due to the $\vec{v}\times\vec{B}$ force. The spiral radius of curvature is known and given by $a = \frac{v}{\omega_r \sin\alpha_p}$, where $\omega_r = eB/\gamma m$ is the gyro-frequency.

The total emission can be written in terms of component along the two different polarizations parallel and perpendicular to the magnetic field direction. A detailed derivation of these components is given in Longair (2011); here i will just report the main points. The two emission components can be written as:

$$\frac{dI_\perp(\omega)}{d\Omega} = \frac{e^2\omega^2}{12\pi^3\epsilon_0 c}\left(\frac{a\theta_\gamma^2}{c\gamma^2}\right)^2 K_{2/3}^2(\eta) \tag{2.20}$$

$$\frac{dI_\parallel(\omega)}{d\Omega} = \frac{e^2\omega^2\theta^2}{12\pi^3\epsilon_0 c}\left(\frac{a\theta_\gamma}{c\gamma}\right)^2 K_{1/3}^2(\eta) \tag{2.21}$$

where $K_{1/3}$ and $K_{2/3}$ are the modified Bessel functions of order 1/3 and 2/3, and $\theta_\gamma^2 = 1 + \gamma^2/\theta^2$ and $\eta = \omega a\theta_\gamma^3/3c\gamma^3$ are two additional variables.

the final step is to integrate over $d\omega$. Since most of the radiation is emitted within a very small angle θ with the respect to the pitch angle of the electron, it can be assumed that the $d\Omega = 2\pi\sin\alpha_p d\theta$ because the element of solid angle varies very little over $d\theta$. in addition, since the radiation is concentrated in a small angle about α_p, we can take the integral limits to

$\pm\infty$. Therefore, the integrals can be written as:

$$I_{\perp}(\omega) = \frac{e^2\omega^2 a^2 \sin\alpha_p}{6\pi^2\epsilon_0 c^3\gamma^4}\int_{-\infty}^{+\infty}\theta_\gamma^4 K_{2/3}^2(\eta)d\theta \quad (2.22)$$

$$I_{\parallel}(\omega) = \frac{e^2\omega^2 a^2 \sin\alpha_p}{6\pi^2\epsilon_0 c^3\gamma^2}\int_{-\infty}^{+\infty}\theta_\gamma^2\theta^2 K_{1/3}^2(\eta)d\theta. \quad (2.23)$$

The integrals have been evaluated by Westfold (1959). The equation 2.23 can be written in term of two additional functions:

$$F(z) = x\int_x^{\infty} K_{5/3}(z)dz \quad (2.24)$$

$$G(x) = xK_{2/3}(x) \quad (2.25)$$

with $x = 2\omega a/3c\gamma^3 = 2\eta/\theta_\gamma^3$. Substituting one can find:

$$I_{\perp}(\omega) = \frac{\sqrt{3}e^2\gamma\sin\alpha_p}{8\pi\epsilon_0 c^3}(F(x)+G(x)) \quad (2.26)$$

$$I_{\parallel}(\omega) = \frac{\sqrt{3}e^2\gamma\sin\alpha_p}{8\pi\epsilon_0 c^3}(F(x)-G(x)). \quad (2.27)$$

This integration represent the energy emitted in the two orthogonal polarization during one period of the electron in its orbit in a time $T_r = \nu_r^{-1} = 2\pi\gamma m/eB$. To obtain emissivities $j_{\perp,\parallel}(\omega)$, it is necessary to divide equations 2.27 for T_r. The total emissivity of a single electron is the sum of $j_{\perp}(\omega)$ and $j_{\parallel}(\omega)$:

$$j(\omega) = j_{\perp}(\omega) + j_{\parallel}(\omega) = \frac{\sqrt{3}e^2\gamma\sin\alpha_p}{8\pi\epsilon_0 c^3}F(x). \quad (2.28)$$

In figure 2.3 it is graphically shown the form of the $F(x)$ function.

To evaluate the radiation spectrum for a distribution of electron energies it is necessary to know the shape of this distribution. Using a general form for the distribution of electron energies $N(E)dE$, the energy radiated in the angular frequency range ω to $\omega + d\omega$ can be attributed to electrons with energies in the range $E + dE$ so

$$J(\omega) = \int_0^{\infty} j(\omega)N(E)dE. \quad (2.29)$$

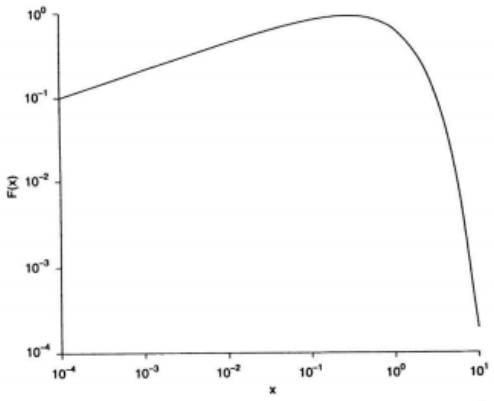

Figure 2.3: The spectrum of synchrotron radiation of a single electron shown with logarithmic axes. The function is plotted in terms of $x = \omega/\omega_c = \nu/\nu_c$ where ω_c is the critical angular frequency $\omega_c = 2\pi\nu_c = (3/2)(c/v)\gamma^2\omega_g \sin\alpha_p$ where α_p is the pitch angle of the electron and ω_g is the gyro-frequency.

2.4.2 Inverse Compton scattering

Inverse Compton (IC) scattering, is the process via which ultra-relativistic electrons scatter low energy photons to high energies so that the photons gain energy at the expense of the kinetic energy of electrons.

An extremely relativistic electron, with Lorentz factor γ encountering a photon with initial energy $E_{\gamma i}$ much less than the electron's rest energy in the electron's rest frame, will up-scatter it in energy by factor of γ^2 and redirect it along the electron's direction of motion, with cross section $\sigma_T \equiv (8\pi r_e^2/3) = 6.65 \times 10^{-25}$ cm^2, where $r_e = 2.82 \times 10^{13}$ cm is the classical electrons radius (Reynolds, 2008).

An isotropic photon field $dn_\gamma(E_{\gamma i})/dV$ photons cm^{-3} erg^{-1} is scattered by a single electron of energy $E = \gamma m_e c^2$ to a spectrum of outgoing photons

given by (Jones, 1968):

$$\begin{aligned}\frac{dn_{\gamma,e}}{dE_\gamma dt} &= \frac{3}{4}\frac{\sigma_T c}{\gamma^2}\frac{m_e c^2}{E_{\gamma i}}\frac{dn_\gamma(E_{\gamma i})}{dV}dE_{\gamma i}\times \\ &\times \left[2q\ln q + (1+2q)(1-q) + \frac{\Gamma_{K-N}^2 q^2(1-q)}{2(1+\Gamma_{K-N}q)}\right]\end{aligned} \tag{2.30}$$

where

$$q \equiv \frac{E_\gamma}{4E_{\gamma i}\gamma(\gamma - E_\gamma/m_e c^2)} \quad \text{and} \quad \Gamma_{K-N} \equiv 4\gamma E_{\gamma i}/m_e c^2.$$

Then the emergent photon spectrum is given integrating equation 2.31 over the electron spectrum, written as $N(\gamma) = N(E)dE/d\gamma = N(E)m_e c^2$, is given by (Reynolds, 2008):

$$\frac{dn_\gamma}{dE_\gamma dt dV} = \int N(\gamma)d\gamma \int \frac{dn_{\gamma,e}}{dE_\gamma dt}. \tag{2.31}$$

When Klein-Nishina effects are negligible, the spectrum has the same shape of the electron spectrum. if the latter has a maximum energy E_{max}, the photon spectrum will have a cutoff at corrisponding frequency $\nu_{max} \sim \gamma^2 <E_{\gamma i}>$, where $<E_{\gamma i}>$ is an average incident photon energy. Below the cutoff, IC has the same slope of the synchrotron spectrum, with index $\alpha = (1+s)/2$ (Reynolds, 2008).

One of the mostly likely source of seed photons for IC scattering is the Cosmic Microwave Background (CMB). Typical value of radiation densities in the vicinity of SNRs are one order of magnitude less (see Gaisser et al., 1998) than the local radiation density. for the CMB radiation, the photon spectrum $dn_\gamma(E_{\gamma i})/dV$ of equation 2.31 is a blackbody at a temperature $T = 2.73$ K.

2.4.3 Bremsstrahlung emission

Bremsstrahlung emission is the radiation of a particle changing its momentum for an interaction, usually with anoter particle of a different species.

In a gas composed by ions and electrons, the main source of bremsstrahlung emission is the interaction between electrons or protons and ions, because ion-ion collisions generates small accelerations due to the high mass involved. Thermal electrons provide the bulk of thermal continuum. Electrons with energies above the shock thermal energies of a few tens of keV at most, will contribute a power-law spectrum with the same phton index Γ as their energy distribution index s. An electron with energy E emits photons up to $\sim E/3$, so the same TeV electrons that contribute keV synchrotron photons, will contribute TeV bremsstrahlung photons. Beginning around 100 MeV, bremsstrahlung photons are emitted by the same electrons that produce radio emission (Reynolds, 2008).

If the electron spectrum is $N_e(E)$ electrons cm^{-3} erg^{-1}, and it encounters protons with density n_H cm^{-3}, Gaisser et al. (1998) estimate that

$$\frac{dn_\gamma}{dE_\gamma dt dV} \sim 7 \times 10^{-16} n_H N_e(E_\gamma) \text{ photons erg}^{-1} \text{ s}^{-1} \text{ cm}^{-3}. \quad (2.32)$$

The full photon spectrum is obtained by integrating the equation 2.32 over the electron distribution.

2.4.4 Nucleon-nucleon interaction

The main radiative mechanism by which energetic hadrons might take themselves evident, is photon emission by the decay of π^0 mesons produced in inelastic scattering of cosmic-ray ions form thermal protons. It is the dominant mechanism and it is the only hadronic process considered in the modeling of SNRs. Above the $\pi-$creation threshold of 1.242 GeV, the cross section for $p + p \rightarrow$anything is just the geometrical cross section of a proton (Reynolds, 2008): $\sigma \sim (10^{-13} \text{ cm})^2 \sim 10^{-26}$ cm^2, little varying with proton energy. Almost all the products are pions and, one third of them are π^0s that decays

into pairs of γ-ray $\pi^0 \rightarrow \gamma + \gamma$ in $\sim 1.78 \cdot 10^{-16}$ s (Longair, 2011). The secondary π^0 spectrum Q_{π^0} (in unit of pions cm^{-3} s^{-1} erg^{-1}) produced by the interaction of an incident flux of energetic protons $\mathcal{F}_p(E)$ with gas with a thermal proton density of n_H cm^{-3} is (Stecker, 1971):

$$Q_{\pi^0}(E_\pi) = 4\pi n_H \int_{E_{min}(p)}^{\inf} dE_p \mathcal{F}_p(E) \frac{d\sigma(E_p, E_\pi)}{dE_\pi}. \tag{2.33}$$

The differential cross section $d\sigma(E_p, E_\pi)/dE_\pi$ involves details of strong-interaction physics. The minimum energy required to produce a pion with energy E_π is given by:

$$E_{min}(p) = m_p c^2 + 2E_\pi + m_\pi c^2 \left(2 + \frac{m_\pi}{2m_p}\right). \tag{2.34}$$

An isotropic distribution of π^0s will decay through $\pi^0 \rightarrow \gamma + \gamma$ to produce photons with a spectrum peaking at energy $m_\pi/2 = 68$ MeV and dropped symmetrically on either side. The higher the energy of the π^0s, the broader the peak. The photon spectrum is given by:

$$\frac{dn_\gamma}{dE_\gamma dt dV} = 2f \int_{E_{min}(\pi)}^{\inf} dE_\pi \frac{Q_{\pi^0}(E_\pi)}{p_\pi} \tag{2.35}$$

where p_π is the pion momentum. To produce a photon of energy E_γ, the minimum pion energy required is $E_{min}(\pi) = E_\gamma + (m_\pi^2 c^4/4E_\gamma)$; the factor f in equation 2.35 is a factor that takes into account the γ-ray produced from He and heavier elements in both projectile and target populations: a good estimation of this factor is $f = 1.45$.

The photon production at a given energy is dominated by protons near the threshold for production of pions, for the steep spectra, so the spectrum from an arbitrary distribution of energetic protons turn on around ~ 70 MeV, and then follows the spectral shape of the proton distribution. If that distribution $N(E_p)$ protons erg^{-1} s^{-1} cm^{-3}changes slowly with energy, one can obtain:

$$\frac{dn_\gamma}{dE_\gamma dt dV} \sim 10^{-16} n_H N(E_\gamma) \text{ photons erg}^{-1} \text{ s}^{-1} \text{ cm}^{-3}. \tag{2.36}$$

2.4.5 Parametric models of the gamma-ray yield from hadronic interactions

In this section I will concentrate on models used to predict the γ-ray yield from hadronic interactions. Most of the section is taken from Dermer et al. (2013) and Kamae et al. (2005). As told in 2.4.4, the threshold for the $\pi-$creation is of 1.242 GeV. There are two class of processes that can produce γ-ray emission: the so called primary and secondary leptonic emission.

Due to the dominant abundance of protons in the CRs, the most important process that contributes to the γ-ray diffuse emission is:

$$\mathrm{p} + \mathrm{p} \rightarrow \gamma + X$$

where X is anything else made from reactions besides γ rays. This is known as primary hadronic emission.

The secondary leptonic emission is produced mainly by the decay of π^0 produced through nuclear collisions. The production of γ rays is mostly mediated by the production and decay of neutral pions. In this case, γ rays are produced through the decay of π^0:

$$\pi^0 \rightarrow 2\gamma.$$

So it is essential to understand the cross section of the processes that produce neutral pions. The main interaction is between protons and hydrogen, the most abundant element in the ISM:

$$\mathrm{p} + \mathrm{H} \rightarrow \pi^0 + \text{anything}.$$

There are also other three minor channels for the production of π^0:

$$\begin{aligned} \mathrm{p} + \mathrm{He} &\rightarrow \pi^0 + \text{anything} \\ \alpha + \mathrm{H} &\rightarrow \pi^0 + \text{anything} \\ \alpha + \mathrm{He} &\rightarrow \pi^0 + \text{anything}. \end{aligned}$$

plus additional minor channels involving nuclei heavier than He that account for an additional 10%. Taking as 1.00 the channel p−H, the rates are: 0.28 for p-He, 0.09 for α−H and 0.02 α−He (Dermer, 1986), so the dominant channel is p−H.

The production of pions near threshold is mostly mediated by resonances like: $\Delta(1232)$, $\Delta(1600)$ and $N(1440)$, all of which decay through a π^0 to make γ-rays. Furthermore, there are baryonic and mesonic decays. In the formes class are Λ and $\bar{\Lambda}$, $\Sigma^0 \rightarrow \Lambda + \gamma$ and Σ^+, with only the Σ^0 in a direct, non-π^0 γ-ray channel. Meson-decay channels are K^+, K^-, K_L and $K_S^0 \rightarrow 2\gamma$.

The goal is to calculate the cross section of these processes to reconstruct the observed γ-ray spectrum. Cross section are tuned with values taken from accelerators, i.e. from the CDF collaboration at Fermilab.

Dealing with quite complex processes, there are two approaches: the analytic (such as Dermer, 1986) and the numeric (i.e. Kamae et al., 2005, 2006) one. Starting from measurements and similar model, in the analytic approach one calculates analytically the γ-ray yield through some approximations, while in the numeric approach one simulates the interactions and, in such a way, calculate the final γ-ray yield.

For the modeling in chapter 6, we use the Kamae et al. model, developed with the numerical approach.

2.5 SNRs as source of galactic cosmic rays

In this chapter I will discuss the SNR paradigm stressing the strengths and the limitations of this assumption and explaining also the connections with observations.

CR spectrum is $\propto E^{-(s+\delta)}$ where s is the source spectral index (~ 2) and

δ is the diffusion coefficient which depends on particle rigidity (Blasi, 2011).

In addition to that, in a magnetic field B expressed in Gauss, an electron of energy E radiates with a power frequency peak of $\nu = 1.82 \cdot 10^{18}\ E^2\ B$ Hz corresponding to an energy of $E_\gamma = 14.7 \left(\frac{\nu_{\mathrm{GeV}}}{B_{\mu\mathrm{G}}}\right)^{1/2}$ GeV. This kind of high energetic charged particles were already known as cosmic rays.

2.5.1 Propagation of Galactic CRs in the Galaxy

Here I will give an overview on how CRs propagates in the Galaxy. For this discussion I will follow (Blasi, 2011). For a complete overview and modelisation of the propagating processes of energetic particles in tenuous plasma, see (Drury, 1983).

The sources in this model are all located in an infinitely thin disk with radius R_d and the diffusion coefficient is constant within a halo of size H. The CRs density is given by:

$$n_{CR}(E) \approx \frac{N(E)\mathcal{R}_{SN}}{2\pi R_d^2}\frac{H}{D(E)}$$

where $\mathcal{R}_{SN}$ is the rate of supernova explosion, $N(E) \propto E^{-\gamma}$ spectrum of CRs produced by an individual SNR, and $D(E)$ the diffusion coefficient. The diffusion coefficient can be expressed as

$$D(E) = 10^{28} \left(\frac{\rho}{3\ \mathrm{GV}}\right)^{\delta}\ \mathrm{cm}^2\ \mathrm{s}^{-1}$$

where $\rho = E/Z$ is the particle rigidity.

If the particles considered are ultra-relativistic protons, their velocity is c, $Z = 1$ and the flux observed at the Earth is:

$$\phi(E) = c\frac{n_{CR}(E)}{4\pi}. \tag{2.37}$$

To fit both B/c ratio and anti-proton data, the approximation $D_{28}/H_{\rm kpc} \sim 1$ is needed. Under this assumption equation 2.37 becomes:

$$\phi_{CR}(E) \approx 2.4 E_{51} \xi_{CR} R_{d,15}^{-2} \mathcal{R}_{SN,30} (\gamma - 2) 3^{\delta} E_{\rm TeV}^{-2.73} \ {\rm TeV}^{-1} \ {\rm m}^{-2} \ {\rm s}^{-1} \ {\rm sr}^{-1}$$

where $E_{51} = E_{SN}/10^{51}$ erg, ξ_{CR} is the CR acceleration efficiency, $R_{d,15} = R_d/15$ kpc and $\mathcal{R}_{SN,30}$ the rate of supernova explosion in unit of 30 per year.

A flux of $8.7 \cdot 10^{-2}$ TeV^{-1} m^{-2} s^{-1} sr^{-1} can be observed at the Earth for a number of combination of ξ and δ. Reference values of these two parameters are: $\xi \sim 7\%$ for $\delta = 1/3$, $\xi \sim 11\%$ for $\delta = 0.54$ and $\xi \sim 58\%$ for $\delta = 0.7$. These are lower limits to the required efficiencies. From these values it is clear that it is necessary to include also dynamical reaction of accelerated particle in the theory of particle acceleration. In addition also streaming instabilities induced by the accelerated particle has to be included because they lead to a magnetic field amplification upstream the shock.

If resonant streaming instability is excited and in absence of damping, the variation of magnetic field from the initial value B_0 can be estimates as:

$$\delta B \sim B_0 \sqrt{2 \mathcal{M}_A \xi_{CR}}$$

where $\mathcal{M}_A \gg 1$ is the Alfvenic Mach number.

The two processes described above are the most important effects in CRs propagation in the Galaxy.

The flux and energy spectrum of CRs are object of an intense study since their discovery in 1912 by Victor Hess. The energy spectrum of CRs extends to energies of about $\sim 10^{20}$ eV and even beyond as shown in Figure 4.2. The CR spectrum has two distinct features showed in Figure 4.2:

- a break at 2.3×10^{11} GeV (as suggested by Adriani et al., 2009, but not confirmed by recent observations with AMS)

- the so-called knee at $\sim 10^{15}$ eV

- a second knee at $\sim 10^{17}$ eV

- an ankle at $\sim 10^{19}$ eV.

. It is believed that all particles below the knee are of galactic origin for energetic reason as discussed in section 2.5.2: the expected energies reached inside the Galaxy extends at least to the knee. Furthermore, the ultra high energy cosmic rays (UHECRs) above the ankle are produced and accelerated outside of the Galactic Disk such as AGN, Gamma-ray Bursts (GRBs), young pulsars, Radiogalaxies and Clusters of galaxies (Aharonian, 2004). Beyond the ankle, powerful accelerators are needed which are supposed to be located outside the Galaxy.

2.5.2 The SNR paradigm

In this section I will try to explain strengths and limitations of the SNR paradigm. For further details, see Blasi (2011) from which I extract this overview.

The spectrum of CR extends over 13 order of magnitude as shown in figure 2.5. The spectrum is measures up to $\sim 10^{11}$ TeV by the Auger experiment. The CR spectrum has two distinct features: the so called *knee* and *ankle* around 10^{15} eV and 10^{19} eV respectively. The particles below the knee are of galactic origin because the Galactic magnetic field confined them. This hypothesis is also supported by the γ-ray observations of the local group of Galaxies. The UHECRs above the ankle are produced and accelerated outside the Galactic Disk, in the Halo of our Galaxy, or in powerful extragalactic objects such as AGN, Radiogalaxies and Cluster of Galaxies.

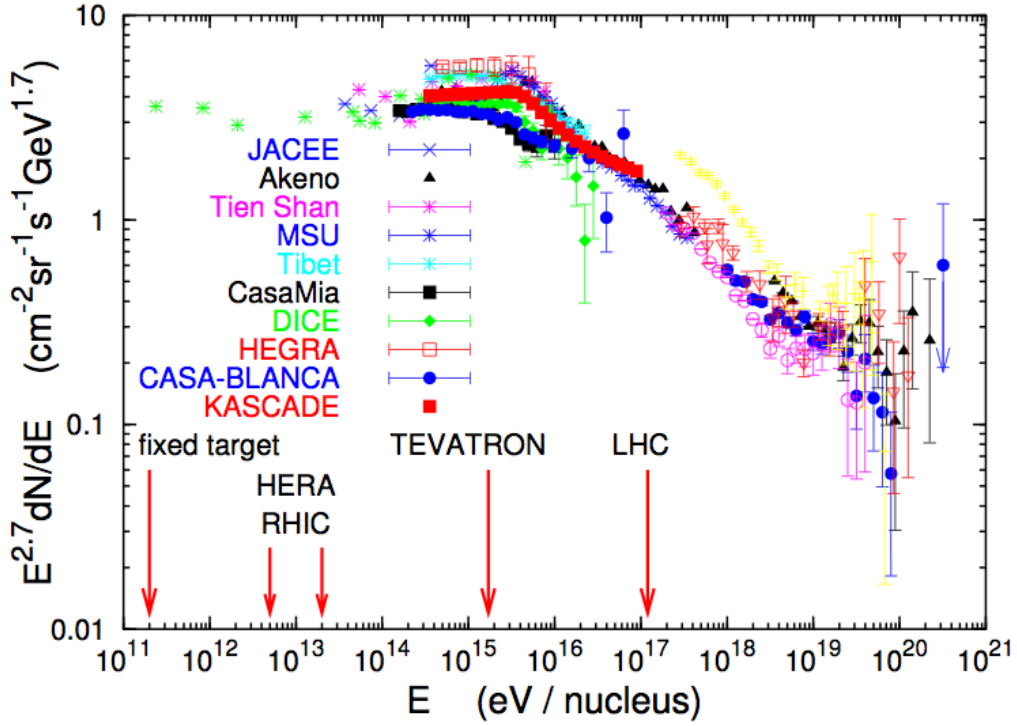

Figure 2.4: Summary of measurements of the all-energy spectrum of CRs. Taken from Aharonian (2004).

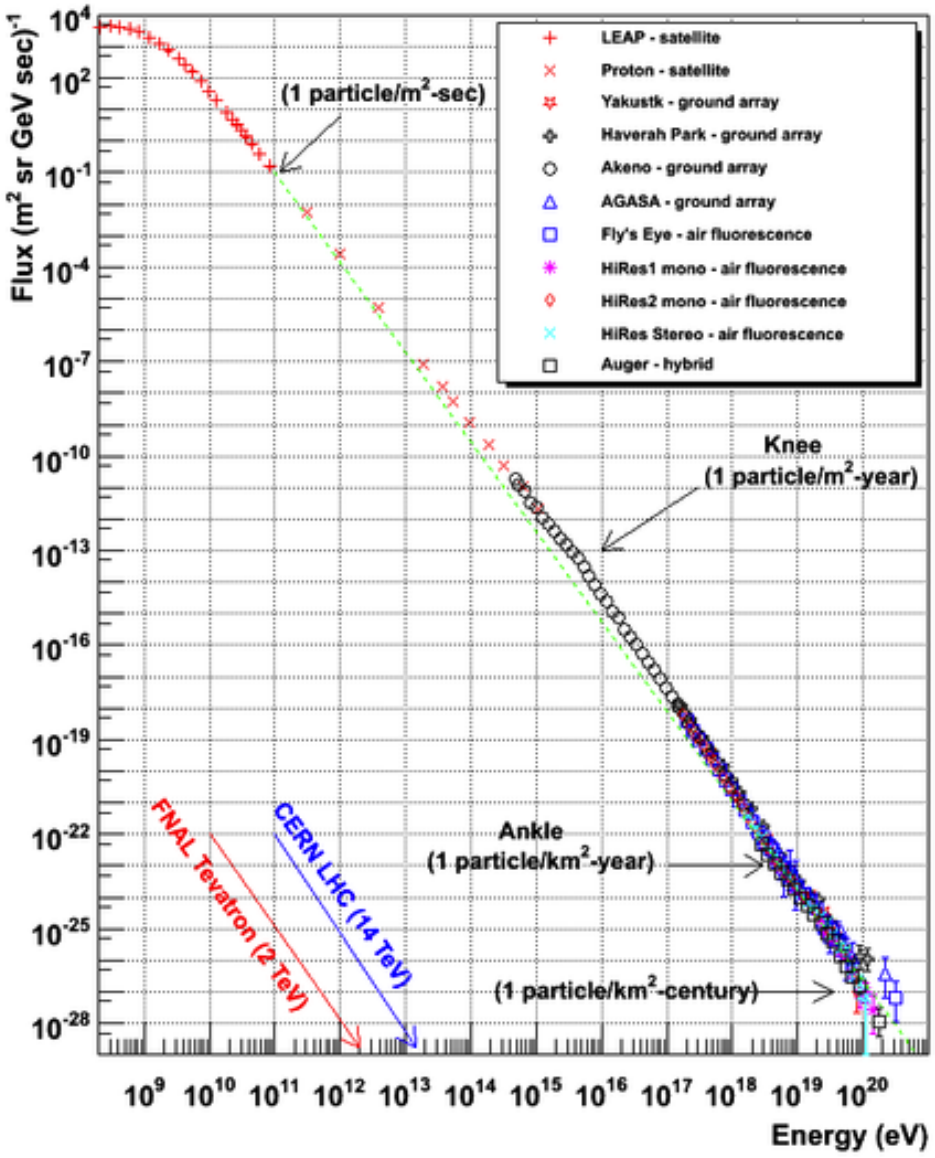

Figure 2.5: The overall differential energy spectra of CRs from various experiment. Prominent features in the spectrum are indicated: the *knee* at 10^{15} eV and the *ankle* at 10^{19} eV. The frequencies of the arrival energies are indicated, as well as the energies attainable in various accelerator experiments (from Longair, 2011)

The extragalactic origin is a good candidate for the highest energy CRs because the large scales permit acceleration to energies beyond the capabilities of galactic environment and particles of these energy are not confined in the Galaxy.

For energetic reasons, SNRs, together with superbubbles, are considered sources of Galactic CRs because they can provide the energy required to explain the CR flux observed at the Earth.

Superbubbles are regions excavated in the ISM by repeated SN explosions, rather than in isolated SNRs. These regions are very active in that several SNRs occur in a relatively short period of time (a few tens million years), and conditions might be better suited for particle acceleration to higher energies (Blasi, 2013). The explosion take place in a metal rich environment, so it can explain some anomalies in the chemical composition of CRs. Particle acceleration may be taking place due to several different processes, from shock acceleration in the winds, to shock acceleration at shocks formed during supernova explosions, to second order acceleration in the turbulent magnetic field deriving from merging winds and SN ejecta. It has also been proposed that the maximum energy that can be achieved is higher than in isolated SNR, although these estimates are somewhat based on simple arguments that may fail to properly represent reality. But all are just hypothesis not well supported by observations.

The SNR paradigm is the assumption that identifies SNRs as sources of of Galactic CRs.

The three main requirements of this paradigm are:

1. SNRs may accelerate with typical efficiency of $\sim 10 - 20\%$;

2. chemical abundance of the nuclei is well described;

3. multyfrequency spectra of individual remnants are well modeled;

The acceleration mechanism that takes places in SNRs is the DSA (described in 2.3.1) even if the energetic requirement stress the fact that the standard test-particle approximation does not represent correctly the CR accelerating process. In particular the reaction of accelerated particles onto the accelerator cannot be neglected and it is responsible of spectral features such as spectral concavity. The reaction of accelerated particles has to be included in DSA also because the standard diffusion coefficient typical of ISM only leads to maximum energies of CRs in range of $\sim$ GeV rather than the observed $\sim 10^6$ GeV. The only way to accommodate this discrepancy is to argue that the accelerated particles generate the magnetic field structure on which they may scatter.

Note that particle acceleration process is strongly dependent upon the environment in which the supernova goes off.

Evidences of efficient CR acceleration

There are three main smoking gun to confirm the SNR paradigm. First of all the *observation of X-ray emission form rims.* Non-thermal X-ray emission is produced by synchrotron emission of high energy electrons in magnetic field. Emission is dominated by the region downstream the shock where the magnetic field is stronger and has a cutoff at a frequency which is independent to the magnetic field and given by: $\nu_{max} \approx 0.2 u_8^2$ keV where $u_8 = u_{sh}/(10^8 \text{ cm s}^{-1})$ is the shock velocity in units of 1000 km s^{-1}. This leads to a maximum energy of $E_{max} \approx 10 B_{100}^{-1/2} u_8$ TeV where $B_{100} = B/100$ µG is the magnetic field in units of 100 µG. The extension of the emitting region at $\nu \sim \nu_{max}$ is given by: $\Delta x \approx \sqrt{D(E_{max})\tau_{obs}(E_{max})} \approx 0.04 B_{100}^{-3/2}$ pc. Typically $\Delta x \sim 10^{-2}$ pc which gives a magnetic field in the downstream region of

$100 - 300$ µG or, in the upstream region, of $20 - 80$ µG. For example in SNR SN 1006, narrow rims ($\sim 10 - 20$ pc) downstream can only be reproduced for efficient particle acceleration scenario.

The second "smoking gun" is given by *collision-less shocks in partially ionized plasma*. Blast waves give rise to collision-less shocks. These shocks are due to plasma processes that affect the ionized component of the plasma. Neutral component is affected by the presence of the shock and particle acceleration only if it exchanges an electron with a ion. This happens only if they are moving at different speed, so in three cases: 1) the temperatures of ion and the neutral are different, 2) the temperatures are the same but the two atoms lie in a different point of the thermal velocity distribution, or 3) the bulk velocities of the two components are different. The signature of this process is the appearance of Balmer lines, that can be both narrow or broad. The narrow lines are due to the neutrals that keep the same temperature that they have upstream and did not suffer the charge exchange; the broad lines are produced by neutrals produced through charge exchange (hot ions before the process). Looking at these two lines, one can estimate the temperature of the two components. The signature, in γ-ray band, of SNRs as sources of galactic CRs, is the pion decay bump (Ackermann et al., 2013).

The last evidence of the SNR paradigm is the *maximum energy and the knee*. From spectrum of individual elements in CRs, one can see that the spectrum decline at $\sim few\ 10^6$ GeV for protons and even before for heavier nuclei. To produce the CR spectrum is necessary to introduce the amplification of magnetic field by ~ 100, using Bohm diffusion. The amplification value is similar to that extrapolated from X-ray observations. For energies above $\sim few\ 10^6$ GeV chemical composition must become heavier and, then, the spectrum of the Galactic CR ends at energy of $\sim 10^8$ GeV and a transi-

tion from Galactic to extragalactic origin happens.

In addition, together with radio data, γ-ray data help to constrain the processes involved in the acceleration of particles in SNRs. Radio data are used to parametrize the particle population which emits via synchrotron radiation. The particles, accelerated via leptonic and hadronic processes described in section 2.3, and emits in the γ-ray waveband. From this analysis, values of the magnetic field and maximum energy reached by the particles can be obtained. Typical values confirms the hypothesis that SNRs are the main sites for the acceleration of Galactic CRs.

Problems of the SNR paradigm

The issues concerning the SNR paradigm are two: the γ-ray observations and the X-ray lines. In this waveband the association between the detected flux to a π^0 decay is problematic because the emission can be associated also with IC scattering of accelerated electrons. In addition most of *Fermi* SNRs has a steep γ-ray spectrum (index $\sim 2.4 - 3$) unlike the flat or concave spectra predicted by the model. Note that steep spectra are observed in old SNRs with nearby molecular clouds that can be a target for inelastic CR collisions.

The are cases in which X-ray lines are not detected, for example in SNR RX J1713-3946. These non-observation is problematic for a scenario in which the detected γ-rays are of hadronic origin.

Chapter 3

The *Fermi* Large Area Telescope

The LAT is the main instrument on board the *Fermi* γ-ray space telescope[1]. The satellite was launched on June 11, 2008 from the Kennedy Space Center (Florida, USA). The LAT is a pair conversion telescope detecting photons from $\sim$ 20 MeV to $>$ 300 GeV and scanning the whole sky every $\sim$ 3 h. The other instrument on board *Fermi* is the Gamma-ray Burst Monitor (GBM), a detector designed to detect the transient phenomena from 8 keV to 40 MeV.

In this chapter, I will give an overview on the detector, its performance and the techniques for high level data analysis. In section 3.1, I will describe all the components of the *Fermi* LAT detector; in section 3.3, the event reconstruction and classification are presented; in section 3.4, I will explain the Instrument Response functions (IRFs).

3.1 The Large Area Telescope

The LAT is a pair conversion telescope detecting photons from $\sim$ 20 MeV to $>$ 300 GeV.

[1] http://fermi.gsfc.nasa.gov

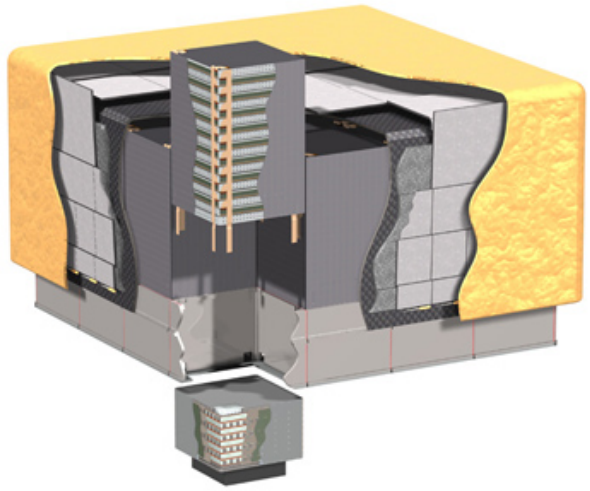

Figure 3.1: Schematic view of the *Fermi* LAT (Atwood et al., 2009). A tower (tracker and calorimeter) is shown for explanation. Details of all the components are available in the text. The telescope's dimensions are 1.8 m $\times$ 1.8 m $\times$ 0.72 m for a total mass of 2789 kg.

Figure 3.1 shows its structure; the detector is an array of 4×4 towers each composed by:

1. a tracker (for details see § 3.1.1)

2. a calorimeter (see §3.1.2)

An anti-coincidence detector completely covers the array of towers and provides a first discrimination between events due to the background (charged particles) and γ-rays (see §3.1.3).

Being a space experiment, the quantity of data that can be downloaded to the ground has to be limited to $\sim$ 1 Mbps. To achieve this goal, most of events triggered by CR have to be rejected in a first on-board analysis, described in section 3.2.

Another requirement for the detector, is that almost all the pair-conversion events started in the tracker have to pass in the calorimeter for energy measurements. This is obtained with an accurate design of the tracker and calorimeter part, that I will describe in next sections.

The discussions about detector building and performance are taken from Atwood et al. (2009).

3.1.1 The tracker

Each tracker module has 18(x, y) tracking planes, consisting of two layers (x and y) of single-sided Silicon Strip Detectors (SSD). The converter-tracker (TKR) (see figure 3.2) is made of 16 planes of high-Z material (Tungsten, placed immediately above each x-y plane) in which the γ-rays can be converted in a e^+e^- pair. These planes are interleaved with detectors to measure the point of passage of charged particles, hence to track their trajectories

and derive the direction of the impinging gamma ray primary. Strips' planes are arranged into an hodoscopic configuration.

The tracker is designed to satisfy two different and opposite requirements: good efficiency in converting γ-rays into pairs, and a good spatial resolution. The first is obtained increasing the thickness of the W converting foils in order to have the maximum number of radiation length. The latter goal is reached using thin converter in order to avoid multiple scattering. To balance the need of thin converters (for a good Point Spread Function (PSF) at low energies) and the need of converting materials (necessary for the effective area at high energies), the tracker was divided into two parts named "front" and "back". The front region has 12(x, y) tracking planes with thin converters foils, each 0.03 radiation lengths to optimize the PSF at lower energies. The back converters (4(x, y) planes after the front-section) are ~ 6 times thicker to maximize the effective area at higher energies[2]

The support structure is a stack of 19 composite panels (trays) supported by a carbon-composite sidewalls that are useful also for the heat conduction to the base of the tracker. The structure is a low-mass, carbon-composite chosen for its long radiation length which prevent γ-rays conversion far from the SSD.

3.1.2 The calorimeter

The main purposes of the Calorimeter (CAL) is to measure the energy deposition due to the electromagnetic shower from the incident γ-ray and image the shower development profile. This last capability is also important to provide a good discrimination method between the shower produced by the

[2]The discussion of the LAT performances, the PSF and the effective area, is postponed to section 3.4.

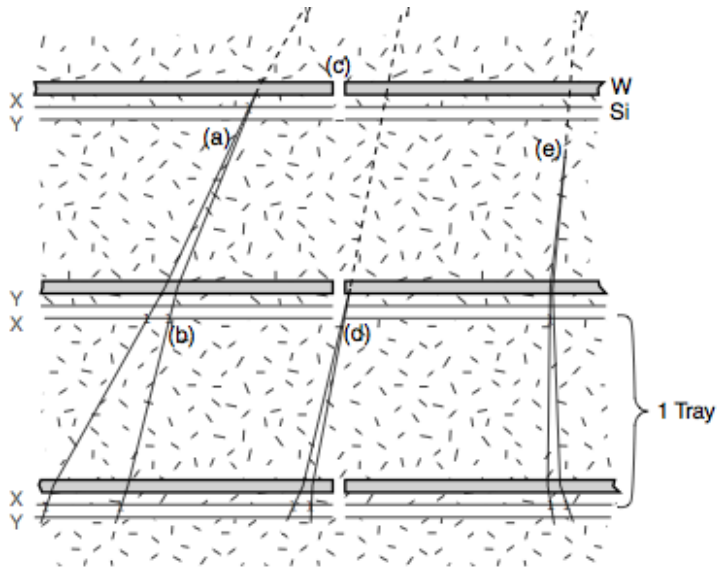

Figure 3.2: Illustration of the design of LAT tracker. This picture shows the conversion of the γ-rays which, ideally, take place as close as possible to the W foils. (Atwood et al., 2009)

γ-ray and the hadronic events.

The calorimeter is composed by 96 CsI(Tl) crystals; each CAL module size is 2.7 cm $\times$ 2.0 cm $\times$ 32.6 cm and it is located below a TKR tower. In each tower the crystals are optically isolated from each other and arranged in 8 layers. The total vertical depth of the calorimeter is 8.6 radiation lengths. Each module is rotated 90° with respect to the crystal in the previous layer, to obtain an hodoscopic array. The segmentation along two coordinates allows to reconstruct the longitudinal coordinate of the passing ionizing particle. Along the crystal, the difference in light yield at the two extremes allows the reconstruction of the third coordinate. From the longitudinal shower profile, an unbiased estimation of the initial shower energy is derived by fitting the measurements to an analytic description of the energy-dependent mean longitudinal profile. To allow the energy reconstruction of events up to $\sim$ 300 GeV, the calorimeter needs to be heavy $\sim$ 1800 kg. On the other hand, this may cause problems with the signal veto, as described in the next section.

3.1.3 The anti-coincidence detector

The main handle to reject charged particles is provided by the Anti-Coincidence Detector (ACD). For this reason, the main requirement is to have a high efficiency in detecting the charged particles (at least 0.9997 for detection of a single charged particles entering the Field of View (FoV) of the LAT).

Another effect that has to be avoided using the ACD is the so called back-splash effect. This effect is due to the isotropically distributed secondary particles (mostly $100 - 1000$ keV photons) from the electromagnetic shower created by the incident γ-ray. In the ACD, the shower can Compton scatter and produce a false veto signal. This effect is the so-called back-splash and it

is caused by the heavy-mass calorimeter. To suppress the back-splash effect, the ACD is segmented and the veto is given only by tiles near the incident incoming particle: such a restriction reduces significantly the area of ACD contributing to the back-splash effect.

The ACD is made of plastic scintillators tiles chosen for their efficiency,their well understood behavior and inexpensive technology. Scintillation light from each tile is collected by wavelength shifting fibers (WLS) coupled with two photomultiplier Tubes (PMTs) for redundancy.

3.2 Trigger and on-board filtering

In this section, I will give a brief overview on the trigger and the on-board filtering of the LAT. For a more detailed description, see Ackermann et al. (2012a).

Each sub-system provides a trigger primitive: a combination of them starts the LAT data taking. The first trigger primitive is generated by the tracker, which is issued when 3 x-y consecutive planes have a signal above threshold. This signals a potential track in a tower. This request is very efficient because often a particle hits more than a track and/or cross more than 3 layers in a same tower.

Another trigger primitive is given by the calorimeter: there is a trigger whenever a crystal ends in the calorimeter is higher than a defined value. There are two types of thresholds: the low-energy ($E > 100$ MeV) and the high-energy ($E > 1$ GeV) threshold.

There is also a veto for the charged particles and it is given by ACD. The trigger system has a programmable list of ACD tiles associated with each TKR tower. If ACD shadowing is enabled an additional trigger is given

when a triggered TKR signal in a tower happens in coincidence with a veto signal in the ACD tiles associated to the same tower.

Finally, there is also a veto for heavily-ionized particles: this signal is used for calibration purpose on the CAL.

There is also an additional trigger primitive, used for diagnostic and calibration purposes: the `PERIODIC` trigger. It runs at a nominal frequency of 2 Hz during all science data taking.

The trigger provided by the TKR and the CAL are tower based. Trigger primitives are collected by the Central Trigger Unit. All the possible combinations of the triggers are mapped into so-called trigger engines: some trigger requests are allowed to open a trigger window of fixed duration (700 ns) and the set of primitives collected in this time interval is compared to a table of allowed trigger conditions (see Ackermann et al. (2012a)). In case a trigger condition is satisfied, a global trigger (or trigger accept) is issued and event acquisition commences. The ACD veto is used to reject background events and the primary source of trigger is the TKR primitive signal.

The on-board filter consists of a few event selection algorithms running in parallel, each independently able to accept a given event for inclusion in the data stream to be downlinked. Every event are filtered in three different ways (Ackermann et al., 2012a):

1. by the `GAMMA` filter which is design to accept γ rays
2. by the `HIP` filter which select heavy ions events for CAL calibration
3. by the `DIAGNOSTIC` filter which enriches the downlinked data with information about sensor performance and selection biases.

The `GAMMA` filter consists of a hierarchical sequence of veto tests: if an event fails a test, does not reach the next step and it is marked for rejec-

tion. This filter has the goal of rejecting events from background or not well reconstructed and its main steps are (Ackermann et al., 2012a):

- reject events with a pattern of ACD tiles that are consistent with CRs and do not have a CAL signal, making them unlikely that the ACD hits were from a backsplash

- accept all events with a total energy deposed in the CAL greater than a programmable threshold (20 GeV)

- reject events that have a TKR trigger associated with an ACD tile pattern

- reject events for which a significant energy deposition in the CAL ($>$ 100 MeV) is present but the pattern of hits in the TKR is unlikely to produce any track

- reject events for which the tracks match with individual ACD tiles and provided the energy in the CAL is less than a threshold currently set at 5 GeV

- reject events that do not have at least one track on-board reconstructed

The on-board filter software is highly optimized for speed, and terminates processing of each event as soon as it is possible to reach a decision (Ackermann et al., 2012a).

3.3 Event reconstruction and classification

In this section, I will describe the process that leads to the reconstruction of a γ-ray from the signatures present in the detector. I will discuss only

`pass7` event reconstruction and performance presently used for released data, including those used for my analysis in chapter 5. A new event reconstruction, entirely based on on-flight data, `pass8`, will be soon released, but I will not discuss it in this thesis. As i will not discuss the upgrade of `pass7` reconstruction, the `pass7rep`. First step to reconstruct events is the track reconstruction, described in §3.3.1: the found tracks are guides for what is expected in the calorimeter and also for the ACD event types. Then I will describe the energy reconstruction done using the CAL data (§3.3.2). Finally, in §3.3.3, the event classification is shown: this last step is useful to classify events to discriminate between photons coming from the background and those associated to a γ-ray source.

3.3.1 Track reconstruction

Spatially adjacent strips are grouped together to form clusters and the coordinates of these clusters are used to reconstruct the track of the incoming particles. Each cluster has a precise z location identified by the silicon hit by the photon. The x and y location is reconstructed using the centroid of the activated strips.

The core of the tracking system is the algorithm that generates tracks hypothesis. A track hypothesis is a trajectory that can be rejected or accepted based on its consistency with the sensors readouts. The generation of algorithms is combinatoric with constraints to the number of trial trajectories considered because of the limited computing power. Two main algorithms are used for events reconstruction: the Calorimeter-Seeded Pettern Recognition (CSPR) and the Blind Search Pattern Recognition (BSPR). The first one uses information from the calorimeter: for most of the LAT science analysis, some energy deposition in the calorimeter is required. When present,

the centroid and the shower axis in the calorimeter can be computed using moments analysis (for details see Atwood et al. (2009)). This algorithm assume that the energy centroid lies close to the trajectory. The first hit in the tracker is chosen as the furthest layer from the calorimeter: also in this case a (x,y) coordinate is given. Now these two points are connected with a straight line: if a subsequent hit is found to be close to this line, a track hypothesis is generated and so on for all the layers. The covariance matrix is also propagated and provides an estimation of the goodness of the track reconstructed. The propagation of covariance matrix includes the material crossed so it provides an estimation of the errors due to the scattering. The quality of the reconstructed track is derived from the values of χ^2, number of hits, number of gaps, etc. Note that, for energies higher than 1 GeV the research of subsequent hits is limited to a cone around the direction provided by the calorimeter moments analysis to limit the back-splash effect.

Instead, the BSRP algorithm does not use information from the calorimeter: the second hit is randomly chosen from the next closest layer to the calorimeter. Then the trajectory is projected to the next layer and if an hit is sufficiently close to the projection, a trial track is generated.

The final stage consists in combining the track into vertices. First the best track is recognized. From this track, the algorithm loops on all reconstructed track and calculates the distances from the best track. Then, if the distance is less than 6 mm, a vertex solution is generated by covariantly combining the parameters of the two tracks. Looking at the first hit, the z-axis location can be located in the center of the tungsten foil, in the silicon detector or within the core material of the tracker tray, above the first hit. Also in this case a quality parameter is calculated from the χ^2 of the combined tracks, the distance of closest approach, etc.

3.3.2 Energy reconstruction

For each calorimeter crystal, the signal from two ends are combined to provide the total energy in the crystal and the position where the energy is deposited. The centroid of the energy deposition is calculated through principal moment analysis. The shower direction is given by the eigenvector with the smallest eigenvalue. The trajectory of the best tracks from the tracker is used also to estimate the energy correction necessary to take into account the leakage out of the calorimeter and the gaps between the crystals. To do this, two algorithms are applied for each event: a Parametric Correction (PC) based on barycenter of the shower, and a fit to the Shower Profile (SP) for the longitudinal and transverse development of the shower. Note that the SP method starts to work with energies higher than 1 GeV so the only algorithm that covers the entire energy range is the PC method.

3.3.3 Event classification

To classify the events according to their quality and their probability to be produced by a gamma ray, some quantities have to be extracted (Ackermann et al., 2012a).

The reconstructed quantities are difficult to analyze, so they have to be transformed in figures of merit (FoMs), that are more convenient to handle. Among all reconstructed energies and directions, one of them has to be extracted to perform the analysis. In addition also "secondary" FoMs are generated to have other physical parameters such as the distance between the ACD and the TKR trace, or an estimation of the confidence of the energy associated with the event analyzed. The performance of the FoMs is well studied and described with Monte Carlo (MC) simulations.

The first step to tag an event as probable charged-particle background is the ACD analysis. The cases for which an event is classified as "background" are two: a significant energy deposition in the ACD and a hit *directed* to less sensitive areas of ACD. Note that also the cases in which the best reconstructed track does not represent a γ ray event is taken into account: this is the so called Charged Particles in the Field-of-View (CPF) analysis. Once the ACD analysis has sealed the detector to the best of our capabilities, the analysis proceeds with a TKR analysis. Events from the CR background, are all those that saturate the energy deposition in the TKR planes and have high energy deposition in the first hit layer. Those events are flagged to remove them from high purity data.

The analysis for background discrimination is based on identifying the topology of γ events. This is performed studying the signatures of events in dedicated MC simulations (for details see §3.3.6 Ackermann et al. 2012a). From this procedure the probability that an event comes from a γ-ray interaction is derived. The next step involves CAL information: general cuts for events coming from the bottom and the sides of the LAT are applied. As for TKR, events are divided into five branches and the probability that an event is a γ ray is derived.

Looking at the probability that an event is gamma-like or background-like, it is possible to classify all events. All data are divided into four categories according to their purity and probability of contamination from background: `TRANSIENT`, `SOURCE`, `CLEAN` and `ULTRACLEAN`. The `TRANSIENT` class is used for the analysis of transient source. A high purity in data is not required therefore the constraints in this class are weak: minimal cuts on quality estimators P_E and P_{core}, lower limit on event energy of 100 MeV, event energy after all corrections must not be higher than 5 times the energy

deposited in the CAL and from CPF analysis the event must not be flagged as charged particle.

The `SOURCE` class is applied to perform the analysis of point sources. It is obtained starting from the `TRANSIENT` class with some additional requirements such as: the event must not be flagged as background based on topological analysis of the TKR and CAL reconstruction and there is an energy dependent cut on the direction reconstruction quality. The required background contamination is ~ 1 Hz in the LAT FoV. This class has most of the photons clustered near the position of the point sources and the background events can be modeled as a isotropic background (Ackermann et al., 2012a).

The `CLEAN` class is constructed starting from the `SOURCE` class and it is useful to study diffuse γ-ray emission and any analysis that need low background contamination (~ 0.1 Hz in LAT FoV). The selection includes: the rejection of an event if it passes through the holes of ACD, the acceptance of the events if it passes the cuts of the ACD designed to remove hadronic CRs.

Finally the `ULTRACLEAN` class is optimized for the study of extragalactic diffuse γ-ray emission. The requirement for the background level is $\sim 40\%$ lower than the `CLEAN` class. This selection is done imposing a constraint in the value of the total probability of having a γ-ray event P_{all} (Ackermann et al., 2012a). Note that all events classes discussed above are nested and for each step, the contamination in the data set decreases, as the detection efficiency.

3.4 The instrument response functions

The Instrument Response functions (IRFs) take into account the effects of the detector. They provide a description of the instrument in terms of transformation probability from the true physical value to the reconstructed quantities. The IRFs not only depend on the instrument itself but also on the reconstruction algorithms and on the background rejection. The IRFs can be expressed as:

$$R(E, \Omega | E', \Omega'; t)$$

where E' and Ω' are the reconstructed photon energy and direction and E and Ω are the true values. The differential count rate is given by the convolution of the source flux per unit of area at the detector with the IRFs:

$$\frac{dN}{dtdEd\Omega}(E, \Omega, t) = \int dE' d\Omega' R(E, \Omega | E', \Omega'; t) \frac{dN}{dtdE'd\Omega' dS}(E', \Omega', t).$$

For the LAT, the IRFs are usually factorized in three different components:

1. the *effective area* $A_{eff}(E', \Omega', s)$ is the product of γ-ray conversion probability and the efficiency for a given event selection (s) for a photon of reconstructed energy E' and incidence angle Ω';

2. the *Point Spread Function* $P(\Omega' | E, \Omega, s)$ is the probability density to reconstruct the direction Ω' for a γ-ray with true energy E and direction Ω in the event selection s;

3. the *energy dispersion* $D(E | E', \Omega, s)$ is the probability density of measuring the energy E' for a γ-ray photon (E,Ω) in the event selection s.

So the instrument response factor can be re-written as

$$R(E|\Omega, |E', \Omega'; t) = T(t) A_{eff}(E', \Omega', s) P(\Omega' | E, \Omega, s) D(E | E', \Omega, s)$$

where the term $T(t)$ accounts for temporal variations, e.g. off time.

In next sections I will briefly describe the LAT performance, as captured by the IRFs parametrization, for the IRFs for the `SOURCE` selection class, so now on the dependence on s will be ignored. The performance plots are taken from Ackermann et al. (2012a).

3.4.1 The effective area

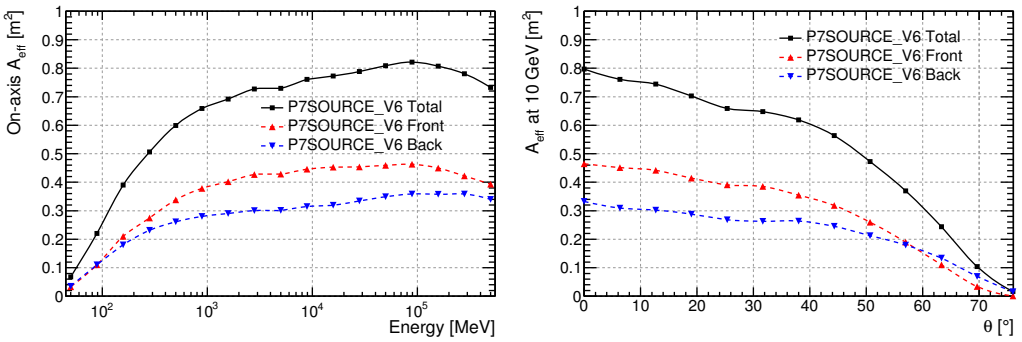

Figure 3.3: *Left panel*: on–axis effective area as a function of energy. *Right panel*: effective area at 10 GeV as a function of incidence angle. Both graphs take into account events from `P7SOURCE_V6` class.

The effective area can be parametrized as:

$$A_{eff}(E,\Omega) = A_{geo}(E,\Omega)P_{conv}(E,\Omega)\varepsilon_{det}(E,\Omega)\varepsilon_{rec}(E,\Omega)$$

where A_{geo} and P_{conv} are the total geometric area and the conversion probability as a function of energy and incident direction; ε_{det} and ε_{rec} represent the instrument detection efficiency and the efficiency of the reconstruction algorithms and the cuts for the background rejection, respectively. Knowing the effective area, it is also possible to determine the rate at which the

instrument will detect a signal:

$$\frac{dN_s}{dt} = \int_E \int_\Omega A_{eff}(E,\Omega) F(E,\Omega) dE d\Omega$$

where $F(E,\Omega)$ is the source flux.

In Figure 3.3, the plots of effective area for `SOURCE` class are shown. As already told in §3.1.1, the tacker is divided in two parts: the first part, made of 12 layers of 3% radiation length tungsten converter, called *Front* and a second part, made of 4 layers of 18% radiation length tungsten converter, called *Back*. These sections have different PSF due to multiple scattering and for each of these case the plot is presented. Figure 3.3 shows the effective area for the total tracker considering both front and back part.

3.4.2 Systematic errors on the effective area

The overall estimate on the uncertainty on effective area (A_{eff}) is shown in figure 3.4.

This estimation takes into account only the largest deviation observed, which is defined as the mismatch between the front-converting and the back-converting events (Ackermann et al., 2012a). To calculate errors, three consistency check are made (Ackermann et al., 2012a):

1. comparing the events from the front and from the back of the detector
2. comparing events from the sides or corners
3. comparing on-axis and off-axis events.

In addition to that, fluxes measured with different event classes are compared. By doing so, the accuracy of the measured efficiency loss are estimated for each of the selection cuts to go from one event class to the next. This analysis

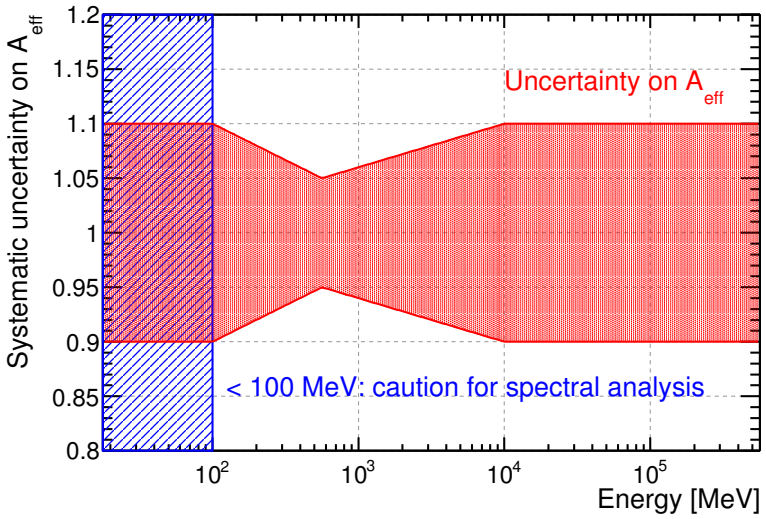

Figure 3.4: Systematic uncertainty band on A_{eff} as a function of energy. From Ackermann et al. (2012a).

is performed using data from the Vela pulsar, a sample of AGN and from the Earth limb.

As shown in figure 3.4, uncertainties can be quoted as: 10% at 100 MeV, then there is a decrease to 5% at 560 MeV, and a new increase at 10% to 10 GeV and above. Note that, under 100 MeV, systematic errors on A_{eff} are very uncertain, so analysis below this energy are not recommended. It is important to note that these errors are expectations about the overall uncertainty of A_{eff} at various energies, and do not include any expectations about what types of deviations we might expect within the stated uncertainty bands, nor about the point-to-point correlations in any systematic biases of A_{eff} (Ackermann et al., 2012a).

To calculate systematic errors, we adopt the method of the *bracketing IRFs*. The idea to do this analysis is modify the IRFs to simulate the worst case scenarios and repeat the analysis extracting the quantities of interest. This process can be applied for the systematic error calculation of fluxes or

spectral parameters. The modified A_{eff} can be written as:

$$A'_{eff}(E,\theta) = A_{eff}(E,\theta) \cdot (1 + \epsilon(E)B(E))$$

where $\epsilon(E) = \frac{\delta A_{eff}(E)}{A_{eff}(E)}$ and $B(E)$ is an arbitrary bracketing function that take values in the $[-1, 1]$ range. The simplest bracketing function is $B(E) = \pm 1$ that minimize and maximize A_{eff}.

To maximize the effect on the spectral index in a power-law fit, we choose a functional form that changes sign at the pivot energy E_0 (Ackermann et al., 2012a):

$$B(E) = \pm \tanh\left(\frac{1}{k}\log(E/E_0)\right)$$

where the parameter k controls the slope of the transition near E_0.

As Ackermann et al. (2012a) stress, the systematic error estimates resulting from this technique represent conservative estimates within the instrumental uncertainties, rather than random variations.

3.4.3 Energy dispersion

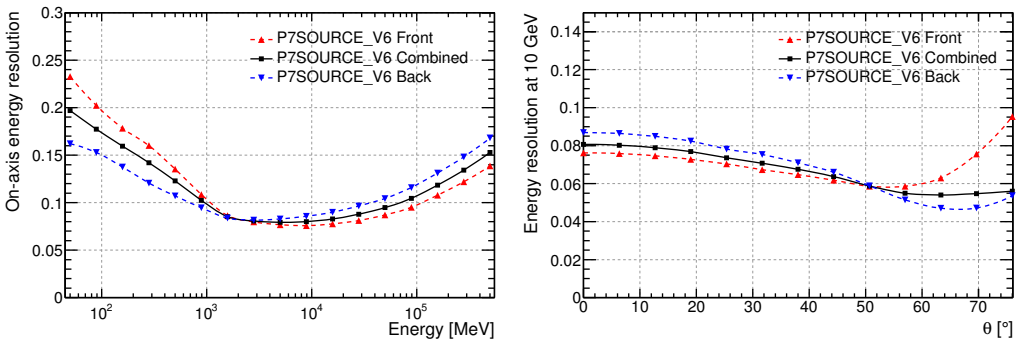

Figure 3.5: *Left panel*: on–axis energy resolution as a function of energy. *Right panel*: energy resolution at 10 GeV as a function of incidence angle. Both graphs take into account events from `P7SOURCE_V6` class.

The energy dispersion is a measure the energy dispersion around the true value and it is shown in figure 3.5. The probability density is generally asymmetric and it is a known characteristic of thin electromagnetic calorimeter, such as the LAT CAL. This feature makes the energy redistribution difficult to parametrize. For the low energy tails, there are not big problems because most of the sources analyzed are steeply falling with energy. For the high-energy part, overestimating the event energy can lead to overestimate the hardness of the source spectrum. To avoid this effect, the event selection is carefully tuned to suppress the high-energy tail, rejecting events for which the energy correction might be overcompensated.

In-flight validation of the energy response function is not obvious because there are not astrophysical sources that provides a spectral line at a well defined energy to calibrate the instrument (e.g. Ackermann et al., 2012b).

3.4.4 The point spread function

At low energies the PSF is mainly determined by multiple scattering. If we consider this as the only consideration on the PSF, this has to become narrower as E^{-1}. But, as reported in Ackermann et al. (2012a), the PSF value decrease as $\sim E^{-0.78}$ at low energies as shown in Figure 3.6. This effect can be explained with the missed hits in the tracker and hard scattering process. All these effects are predicted in MC simulations.

Above few GeV the narrowing of PSF is limited by the limited hit resolution of SSDs. At a normal incidence, this effect can be quantified in $\sim 0.1°$. The transition to this precision dominated regime is calculated via MC simulation and it is expected to occur between $\sim$ 3 GeV and $\sim$ 20 GeVas can be observed in Figure 3.6.

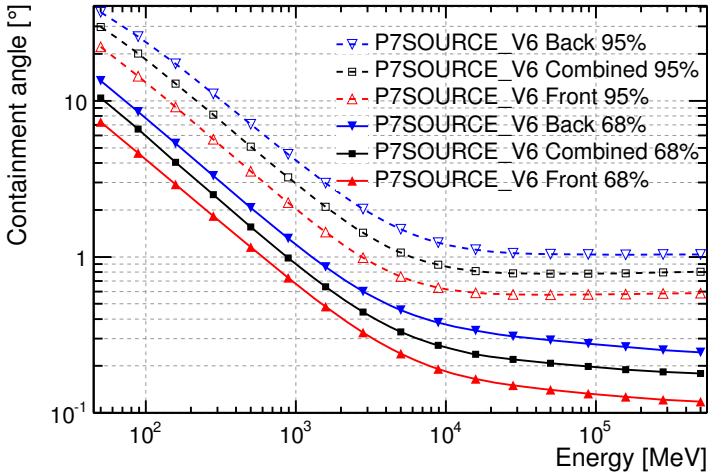

Figure 3.6: 69% (solid lines) and 95% (dashed lines) containment angles in function of energy for the `P7SOURCE_V6` event class.

3.5 *Fermi* LAT data analysis

The aim of this section is to provide an explanation to the *Fermi* LAT analysis. The LAT collaboration developed high-level analysis tools, called Science Tools (ST), to study the LAT data. These tools are publicly available through the FSSC[3]. The ST include tools for studying the temporal behavior of the pulsar, rapid simulation of LAT observation, data reduction and likelihood analysis. In this section, I will concentrate only on the last two aspects, which are relevant for the analysis I made in chapter 5.

The *Fermi* LAT collaboration developed two type of analysis: the `UNBINNED` and the `BINNED` analysis. `UNBINNED` treats each single event separately, `BINNED` allows to reduce memory and CPU usage by binning in direction and energy.

[3] `http://fermi.gsfc.nasa.gov/ssc/data/analysis/documentation/Cicerone`

3.5.1 Data selection and analysis

The first step of the high-level analysis is the *event selection*. We perform the cut based on the energy, Region of Interest (RoI) and energy event class. Usually, the energy selection is from 100 MeV to 300 GeV even if the LAT could reconstruct photons with energies down to 20 MeV. For this last energy range (from 20 MeV to 100 MeV), huge systematic errors due to effective area calculation and interstellar emission model are introduced. Usually, the RoI is a circle centered at the source position and with a radius of $\sim 15^{\circ}$. Smaller RoI could be used to avoid contamination from high emitting regions not completely modeled by background model (e.g. Galactic Plane, Cygnus region, etc.). To take into account the effect on γ-ray emission from Earth's atmosphere (its contribution is significant for zenith angles $> 103^{\circ}$), we perform a cut on the zenith angle. With this cut, we select only events for which the reconstructed direction is less than 100°from the local zenith. The exposure is normalized excluding all the time intervals for which the zenith angle is $> 100^{\circ}$. This is a strategy developed for point source study. It is also possible to select smaller time intervals to plot curves of the source flux along the time.

For the temporal cut, we take into account all the time intervals in which the LAT is in calibration mode or in non-standard data-taking configuration. We also exclude time intervals whee the LAT boresight is rocked with respect to the local zenith by more than 52°mostly for pointing purpose. These steps of analysis are common for both `UNBINNED` and `BINNED` analysis. Now on I will describe only `BINNED` analysis because this is the technique I will use for analysis in chapter 5.

After all these preliminary cuts, we calculate the *cubic counts map*: we divide all the energy range into slices and, for each energy slide a squared

count map is computed. This map, with the livetime cube, the exposure map and the source map, are the basic input for the minimization of the Likelihood (explain in section 3.5.2). The second map needed for the likelihood calculation is the *livetime cube*: this is a 3D map covering the full sky of the integrated livetime as a function of inclination with respect to the LAT z-axis. The map reports, for each point in the sky, the integrated livetime in function of the incidence angle. This along with the A_{eff}, is needed to calculate the exposure which is the constant of proportionality between measured counts and flux of the source. This step is necessary to speed up the exposure computation. Then the *exposure map* is computed: it covers the same region of the sky as the counts maps and has separate planes for different energies spanning the energy range of the counts maps. Note that the exposure needs to be recalculated if the RoI, zenith angle, time, event class, or energy selections applied to the data are changed. For the binned analysis, this also includes the spatial and energy binning of the 3D counts map. The last step, before the likelihood maximization, is the computation of the *source map*: to do this map a `XML` model is needed. This model contains all the sources contributing to the RoI emission and two background model, one taking into account the extragalactic isotropic emission and the other miming the galactic interstellar emission (for further details on background model see §4). The *source map* is a 3D counts map with all the contribution from the sources present in the `XML` model multiplied by exposure and convolved with the effective PSF.

Then the maximum likelihood analysis can be performed. In next session I will describe all the details for this kind of analysis.

3.5.2 The maximum likelihood analysis

The main problems in fitting the *Fermi* LAT data is the limit statistic and the presence of high background level. In addition, also the angular resolution is a problem for fitting the *Fermi* LAT data for two reasons. First the angular resolution is rapidly varying with energy. Secondly, it is not possible to associate uniquely a photon to a source, specially for sources very close each other or in background dominated areas (e.g. Galactic plane) To solve these features, the statistical approach adopted is the Likelihood analysis based on Poisson statistics. The γ-ray data analysis is based on Mattox et al. (1996), which perform an analytic study for the likelihood of the EGRET data.

The likelihood value quantify the relative extend to which the data support a statistical hypothesis. The estimate is the value of the parameters that maximize the likelihood value.

The likelihood ratio is the value of the likelihood of the null hypothesis for the data divided by the likelihood of the alternative hypothesis for the same data. Wilks (1938) states that the -2 times natural logarithm of the likelihood ratio behave as the χ^2 with n degrees of freedom, where n is the difference of degrees of freedom in the null hypothesis model and the degrees of freedom of the alternative model.

The likelihood is the probability of the observed data for a specific model of high-energy γ-ray emission. It is the product of the probability for each pixel (Mattox et al., 1996):

$$L = \prod_{ij} p_{ij}$$

where

$$p_{ij} = \frac{\theta_{ij}^{m_{ij}} e^{-\theta_{ij}}}{n_{ij}!}$$

is the Poisson probability of observing n_{ij} counts on pixel ij with the number

of counts predicted by the model θ_{ij}. To easily manipulate this value, the natural logarithm of this quantity is calculated:

$$\ln L = \sum_{ij} n_{ij} \ln(\theta_{ij}) - \sum_{ij} \theta_{ij} - \sum_{ij} \ln(n_{ij}!).$$

Because the last term is model independent, it is not useful for the calculation of the likelihood ratio test so it is possible to neglect it, so the previous formula becomes:

$$\ln L = \sum_{ij} n_{ij} \ln(\theta_{ij}) - \sum \theta_{ij}. \tag{3.1}$$

The first term causes $\ln L$ to increase as the model predicts counts in pixels where they actually occur. The second term demands that model counts be parsimoniously allocated.

To estimate the significance of a source, the likelihood ratio test is used. We assume as null hypothesis that no point source exists at the position under consideration, the alternative hypothesis being of course that the point source does exist. The quantities extracted from the fit of the two models are: the value of $\ln L_0$ from the first fit, and the value of $\ln L_1$ from the second one. The logarithm of the likelihood ratio is $\ln L_0 - \ln L_1$. The point-source Test Statistics (TS) is defined as:

$$TS \equiv -2(\ln L_0 - \ln L_1) \tag{3.2}$$

and it is expected to behave as the χ^2 with n degrees of freedom, where n is the difference of degrees of freedom in the null hypothesis model and the degrees of freedom of the alternative model (Wilks, 1938).

Chapter 4

The diffuse gamma-ray Sky

The majority of Supernova Remnants are located in the Galactic plane, a region where the dominant backgrounds for γ-raystudy for sources are the γ-ray emission from interstellar gas due to cosmic-ray interactions and IC from interaction with Interstellar radiation field (ISRF). In this chapter, I will briefly illustrate the physical processes producing interstellar emission (§4.1 and 4.2), and how this emission is modeled for the analysis of LAT sources (§4.4.2 and 4.4.1). Then I will describe how the *Fermi*LAT collaboration developed models to estimate the systematic uncertainties of the diffuse interstellar emission model (see section 4.5).

4.1 The tracers of the interstellar medium

The understanding of the nature and the physical properties of ISM is of crucial importance in astrophysics. For an accurate study of sources located in the Galactic plane, a good and detailed knowledge of the diffuse interstellar emission is necessary. Stars do not sit in vacuum, but they stay in a rich intestellar environment populated by gas, CRs and electromagnetic field. The

diffuse γ-ray sky is the result of the interaction of CRs with ISM. To map it in details, we have to know the distribution of CRs in the ISM (see chapter 2), the composition of intergalactic gas and interstellar magnetic field which give information on the synchrotron emission. In this section, I will give a brief overview on the tracers of ISM and the techniques we can adopt to estimate interstellar magnetic field.

The mass of the interstellar gas is $\sim 10\%$ of the visible mass of the Galaxy. In the Galactic plane, close to the Sun, the overall gas density can be as high as $\sim 10^6$ particles cm^{-3} (Longair, 2011) but the variations from place to place are huge.

To understand the composition of the interstellar medium, we combine several multi-wavelength tracers, details about which are given in this section.

4.1.1 Neutral interstellar gas

There are five main bandwidths in which investigate the presence of neutral interstellar gas: the $21-$cm line of neutral hydrogen, sub-mm for molecular lines such as the CO, optical, ultraviolet and X-ray. In this section I will describe the emission mechanisms that proivde us with tracers of the neutral ISM.

H I 21-cm line The emission of this particular transition is at 1420 MHz that corresponds to $\lambda_0 = 21$ cm. The radiation comes from the transition between the two levels of the hydrogen 1s ground state, slightly splitted by the interaction between the electron spin and the nuclear spin with transition from $S = 1$ electron spin to $S = 0$. Because of the quantum properties of radiation, hydrogen in its lower state will absorb 1420 MHz and the observation of 1420 MHz in emission implies a prior excitation to the upper state.

This is an almost totally forbidden hyperfine transition: the spin of electron and proton from parallel became anti-parallel. The transition rate is:

$$A_{21} = 2.85 \cdot 10^{-15}\ \mathrm{s}^{-1}$$

where A_{21} is the Einstein's coefficient and represents the transition probability per unit of time between the upper energy level 2 and the lower energy level 1. This value means that this transition happens once every 10^7 yr for each atom. In spite of the low emission probability, the large amounts of interstellar hydrogen makes the line clearly detectable. Because of their small transition probability, collisions and other processes have enough time to reach the dynamical equilibrium between hydrogen atoms in the lower and upper states. The ratio between the number of atom in the excited and the number in ground state is given by the Boltzmann equation:

$$\frac{N_2}{N_1} = \frac{g_1}{g_2} \exp\left(-\frac{h\nu_0}{kT}\right)$$

where T is the excitation temperature and g_n is the statistical weight of the state ($g_2/g_1 = 3$).

The two easier cases for studying the interstellar medium are: the optically thin and the optically thick regime.

In the first case, if the emitting region is optically thin, only spontaneous emission takes place and the emissivity κ_{12} is given by:

$$\begin{aligned} \kappa_{12} &= \frac{g_2}{g_1 + g_2} n_H A_{21} h\nu_0 \\ &= \frac{3}{4} n_H A_{21} h\nu_0 \end{aligned}$$

where n_H is the number density of atomic hydrogen atoms and A_{21} is the Einstein's coefficient defined above. If the hydrogen is distributed along the line of sight of the observer, the flux S received is given by:

$$S = \int \frac{\kappa_{21}(r)}{4\pi r^2} \Omega r^2 dr$$

where Ω is the solid angle subtended by the beam and r the distance along the line of sight. From this relation one can calculate the intensity received

$$I = \frac{S}{\Omega} = \frac{3}{16\pi} A_{21} h\nu_0 \int N_H dr.$$

The integral is also known as *total column density*, so the value of the intensity is also a measure of the total column density. Due to the small probability transition the 21-cm line is very narrow. If the neutral hydrogen is in motion, the Doppler effect is clearly visible and detectable in the Galaxy even if also turbolent motion inside gas clouds can affect the measurements. This effect can be used to separate different clouds along the lines of sight.

The other simple case is the optically thick regime. If there are high emitting radio sources and there are H clouds along the line of sight, we have an absorbed spectrum. If $h\nu \ll kT$, the spectrum is that of a black-body[1]:

$$\chi_\nu I_\nu = \chi_\nu \frac{2kT}{\lambda^2} = \frac{\kappa_{21}}{4\pi}.$$

If $\Delta\nu$ is the line width, the emissivity per unit of frequency interval is $\kappa_{21} = \frac{3}{4} N_H A_{21} h \frac{\nu_0}{\Delta\nu}$ and the absorbing coefficient

$$\chi_\nu = \frac{3}{32\pi} \frac{A_{21} h c^2}{\nu_0^2 k T_S} \frac{\nu}{\Delta\nu} N_H$$

where T_S is the so-called spin temperature defined as the excitation temperature of the hyperfine levels defined by the Boltzmann equation. If the brightness temperature T_b is much greater than the spin temperature ($T_b \gg T_S$) the intensity I_ν becomes

$$I_\nu = I_0(\nu) e^{-\chi_\nu l}$$

where l is the path length through the cloud. Note that, to calculate this quantity, the knowledge of T_S is needed.

[1] intensity given by: $I_\nu = \frac{2kT}{\lambda^2}$

The determination of $N(H)\ I$ requires to know for each position (i.e. each velocity v) the spin temperature and the optical depth τ:

$$N(H\ I) \equiv C \int T_S \tau(v) dv \tag{4.1}$$

with $C = 1.823 \times 10^{18}$ atoms cm^{-2} (K km s^{-1})$^{-1}$.

The measurements of neutral hydrogen are interesting because we get some information from absorption and emitting spectrum. From the absorption measurement, we investigate small scale structures and on velocity dispersion along the line of sight on the scale of the angular size of the background sources. From the emitted spectrum we can calculate the large scale distribution of neutral gas.

Molecular radio lines The importance of observing molecules in the radio band is that there is no extinction due to interstellar dust as it happens in the optical waveband. The physical processes that leads to emission are associated with transitions between electronic, vibrational and rotational levels. Each of those corresponds to a characteristic energy range. The highest energies are reached by electronic transitions, and the peak is in the optical waveband; the vibrational transition are associated with molecular binding between atoms of molecules and the spectral region in which they emit is the infrared ($h\nu \sim 0.2$ eV); finally, the rotational level transitions derive from quantization of angular momentum and produce emission in the sub-mm domain.

Molecular lines provide information about denser region of interstellar gas than the 21-cm line emission because the molecules can be dissociated by ultraviolet and optical photons. Typically, this phenomenon happens for clouds with densities of $n_H \sim 10^{9-10}$ m^{-3}.

The most abundant molecule in the universe is H_2 but it has no electric

dipole moment so there are no rotational transitions. The presence of molecular gas is assured by observations in UV: molecular hydrogen was detected in absorption in the UV region of the spectrum through its electronic transitions. These observations confirmed that H_2 is present in large quantities in in the interstellar gas.

The next most abundant molecule is CO. It is often assumed that the CO line intensities trace the column densities of molecular hydrogen. A probable explanation of the usage of CO as a tracer of H_2 is, if CO exist, H_2 must also exist because the excitation is due to collisions with molecular hydrogen molecules. We can use CO instead of H_2 because, in the conditions in which C and O form CO molecules, also hydrogen atoms can produce H_2 molecules. The proportionality between CO luminosity and H_2 is assured by viral masses, infrared (IR) and γ-ray emission.

Optical and Ultraviolet absorption lines To emit in the optical waveband atoms must have excited states at energies larger than 4 eV from the ground state so only few species emit. The species observed in stellar spectra are: Na I, Ca II, Ca I, K I, Ti II and Fe I. For higher energy transitions, we must look at the ultraviolet region (100-300 nm). In this band there is a wider range of interstellar atoms and molecules to be studied. For interpreting the absorption lines, one must know the absorption cross section $\sigma(\nu)$ which can be analytically calculated for simpler cases or derived from laboratory experiments. The cross section depends on the frequency, ν. The frequency dependence of the absorption cross-section depends upon the mechanism of the line broadening. This feature could have two explanations. The first is Doppler effect: the absorbing atoms are moving or the bulk motion within the clouds, producing the broadening of the absorption line. The second ex-

planation is the so called "natural broadening": atoms remain a finite time Δt in excited state. In this case the broadening can be estimated from the Heisenberg's uncertainty principle

$$\Delta E \simeq \frac{h}{\Delta t} \Longrightarrow \Delta\nu \simeq h\Delta t^{-1}.$$

If the medium is optically thin, the optical depth $\tau_\nu = \int \sigma_i N_i dl$ measures the total column density of the i atomic species.

X-ray absorption In the X-ray band, the photoelectric absorption is the process responsible of the emission in this waveband. An approximation of the absorption curve is (Longair, 2011)

$$\tau_X = 2 \cdot 10^{-26} \left(\frac{h\nu}{1 \text{ keV}}\right)^{-8/3} \int N_H dl$$

where the integral is the column depth of atomic hydrogen. The photoelectric absorption takes place within the source itself or in the intergalactic medium, for example in our Galaxy.

Interstellar dust An important part of the ISM is dust, which is responsible of patchy obscuration observed in optical images of the Galaxy. It contains a large fraction of the heavy elements present in the interstellar medium. Dust is also present in most environments in the Universe, unless it is heated to temperatures above material's sublimation temperature, which is about 10^3 K. Emission due to dust is observed in shells of dying stars and supernova when the temperature falls below 10^3 K. In optical and infrared the effect due to the presence of dust is described with an extinction law $S \propto e^{-\tau}$ where τ is the optical depth depending on wavelength as $\tau \propto \lambda^{-x}$ ($x \approx 1$ in optical and $1.6 \lesssim x \lesssim 1.8$ in infrared). Studies in optical, infrared and ultraviolet wavebands show that interstellar dust must be composed of a

number of different components. Interstellar dust causes two major observable phenomena:

1. absorption of ultaviolet and optical radiation

2. re-radiation of the radiation absorbed in IR.

From accurate study of interstellar dust, we can understand its composition. Using both HI , Lyman α and H_2 Lyman-Werner bands in the UV band it is possible to derive the hydrogen column density in the diffuse ISM (Bohlin et al., 1978). In addition, in interstellar dust are also present small aromatic molecules known as polycyclic aromatic hydrocarbons, or PAHs. the molecules typycally consist of $\sim$ 50 carbon atomsin the form of planes of exagonal benzene rings.

4.1.2 Ionized interstellar gas

The four main processes I will describe in this section to detect ionized interstellar gas are: free-free emission, permitted (and forbidden) transitions in gaseous nebulae, dispersion measurement of pulsar, and Faraday rotation of linearly polarized radio signals.

Free-free emission Free-free emission, also known as thermal Bremsstrahlung emission, is produced by thermal electrons scattering off ions without being captured: the electrons are free before the interaction and remain free afterwards.

It produces a flat spectrum up to $h\nu \approx kT$ (with T the plasma temperature) beyond which there is an exponential cutoff. The Bremsstrahlung intensity along the line of sight can be evaluated as $I_\nu \propto \int n_E^2 T^{-1/2} dr$.

From this relation we can conclude that, for radio spectra of compact region of ionized hydrogen, $I_\nu \propto \nu^2$ (Longair, 2011). For very low frequencies ($\nu \leq 10$ MHz) absorption by the diffuse ionized interstellar gas becomes important and the Galactic plane can be observed in absorption against the background of Galactic non-thermal radio emission. The X-ray band, thermal Bremsstrahlung is due to intergalactic gas and in the shell of SNRs.

The soft X-ray emission from the plane of the Galaxy is interpreted as the diffuse thermal bremsstrahlung of the hot component of the interstellar gas which is also responsible for the ultraviolet O VI absorption lines (Longair, 2011). This hot gaseous component is responsible of ultraviolet O VI absorption line at a temperature $T_{gas} \sim (1-3) \cdot 10^6$ K.

All these components give a global image of the variety of species present in the ISM.

Permitted and forbidden transitions Strong emission lines are observed from high-density regions of interstellar gas and are generated by the emission from atoms excited by ultraviolet emission of hot stars; the environment in which this emission takes place are in the vicinity of new forming stars or near stars dying. Heating and ionization of gas are driven by radiation emitted from stars. These processes take place only if $h\nu \geq 13.6$ eV $= E_i$ which is the ionization potential of hydrogen. Hydrogen recombination lines are the strongest observed and responsible of cooling. They are observed from diffuse warm component of interstellar gas so they can be of difficult interpretation due to absorption from the environment. The emission from Hα lines is present in the entire sky and i Galactic regions with $|b| > 10^\circ$ and can be roughly approximated by a $cosec|b|$ relation which indicates emission from a thin disk. Further information on temperature and density can be

obtained from forbidden lines of [N II], [S II] and [O III]. For example in optical bandwidth, the forbidden levels are populated by collisions with energy within few eV from the ground state. For C, N, O, Ne, S the accessible levels are metastable (with excitation energy of $\lesssim$ 5 eV. The only way to return to the ground state is through a transition violating the rules of electric dipole. Using these lines, one can determine densities and temperature of the emitting line regions. We can distinguish two cases:

- low density region: there is the emission of a photon and the intensity line is proportional to the rate of collisional excitation

- high density region: the phenomenon it takes place is de-excitation by electron collision, so there is a suppression of emission line.

So, calculating the ratio between different forbidden lines from the same region, the electron density can be obtained. The medium considered is ionized but globally neutral so, the number of electrons and protons are the same as it is the same the density of electrons and that of the hydrogen.

Dispersion measure of pulsars An estimate of the column density of free electrons in the Galaxy ($\int n_e dl$) can be obtained by measuring the time delay of arrival times of radio pulses as a function of frequency. In the radio waveband ($\nu \approx 10^2 - 10^3$ MHz), the ratio between the plasma frequency[2] ($\nu_p = \sqrt{\frac{e^2 n_e}{4\pi^2 \epsilon_0 m_e}} = 8.98 n_e^{1/2}$ Hz) and the frequencies considered is smaller than one ($\nu_p \ll \nu$) so the velocity of the wave-packet (v_{gr}) can be expressed as:
$v_{gr} = c\left[1 - \frac{1}{2}\left(\frac{\nu_p}{\nu}\right)^2\right]$. If the pulse is emitted at $t = 0$, the arrival time of the

[2]the plasma frequency is defined as the natural collective oscillation frequency of a charge species in a plasma, in the absence of a magnetic field.

signal is

$$T_a = \int_0^l \frac{dl}{v_{gr}} = \int_0^l \frac{dl}{c}\left[1 + \frac{1}{2}\left(\frac{\nu_p}{\nu}\right)^2\right] = \frac{l}{c} + \frac{e^2}{8\pi^2\epsilon_0 m_e c}\frac{1}{\nu^2}\int_0^l n_e dl$$

so a measure of T_a is also an estimation of the electron density. pulsars of known distance are used to build maps of ionized gas in the Galaxy. These models are then used to calculate distances of other pulsars (i.e. Taylor and Cordes, 1993; Cordes and Lazio, 2002).

Faraday rotation of linearly polarized radio signals Ionized interstellar gas is permeated by magnetic fields and constitutes a magnetized plasma or magnetoactive medium. The Faraday rotation is the effect for which the position angle of the electric vector of linearly polarized emission is rotated while propagating along the magnetic field direction. A linearly polarized wave can be decomposed on the two eigenstates of circular polarization. If $\nu_g/\nu \ll 1$ (where $\nu_g = 2.8 \cdot 10^1 0$ B Hz is the gyrofrequency with B expressed in Tesla [T]), the reflective index of the two modes are: $n^2 = 1 - \frac{(\nu_p/\nu)^2}{1 \pm (\nu_g/\nu) cos\theta}$ where ν_p is the plasma frequency and θ is the angle between the magnetic field and the direction of the incident wave. When two elliptically polarized components are added together at depth l through the region, if $\frac{\nu_p}{\nu} \ll 1$ and $\frac{\nu_g}{\nu} \ll 1$

$$\Delta n = \frac{\nu_p^2 \nu_g}{\nu^3} cos\theta \Longrightarrow \Delta\phi = \frac{2\pi\nu\Delta n}{c} dl$$

where $\Delta\phi$ is the phase difference. The electric vector is rotated of $\Delta\theta = \frac{\Delta\phi}{2} = \frac{\pi\nu_p^2\nu_g}{c\nu^2} cos\theta dl$ and, resolving for θ

$$\theta = \frac{\pi}{c\nu^2}\int_0^l \nu_p^2 \nu_g cos\theta dl = 8.12 \cdot 10^3 \lambda^2 \int_0^l n_e B_\parallel dl$$

where l is measured in pc and $B_\parallel$ is the magnetic field parallel to the line of sight expressed in T. θ/λ^2 is the rotation measure: the sign of this quantity gives information about the weighted mean direction of magnetic field

along the line of sight. Observing the sources (that emit linearly polarized radiation) we can have information on $n_e B_{\parallel}$ along the line of sight.

4.2 Galactic diffuse emission

Galactic diffuse emission dominates other components of the γ-ray sky in the GeV domain and has a wide distribution with most emission coming from the Galactic plane. It is a superposition of γ-rays produced in the interstellar medium by interactions between CRs nuclei and gas, electron Bremsstrahlung due to gas nuclei, IC scattering of soft photons by CR electrons, and an isotropic component supposedly of extragalactic origin. Galactic diffuse emission encodes the distribution of CRs and ISM throughout the Milky Way (e.g. Abdo et al., 2009b). Modeling such component is crucial for extracting a residual isotropic emission and affects how the extragalactic background is derived. In addition, the diffuse γ-ray emission is a natural background for many signals such as point sources or annihilating Dark Matter (DM). The ratio between hadronic component of the Galactic γ-ray diffuse emission and IC or Bremsstrahlung mechanism above a few hundred MeV and below $\sim$ 10 GeV is highly dependent on the sky region observed. An example is shown in figure 4.1 for $0^\circ \leq l \leq 360^\circ$ and $10^\circ \leq b \leq 20^\circ$ where the hadronic component dominates IC and Bremsstrahlung emission.

The diffuse γ-ray emission gives information on the origin and propagation of CR which are made of *primary* protons, nuclei and electrons. All these particles are accelerated to relativistic energies by powerful objects like SNRs (§2). At the same time, a major fraction of species in CRs have a *secondary* origin. These particles are nuclei of the (Li, Be, B) group, anti-particles produced by the interaction of primary CRs with ambient interstellar gas and

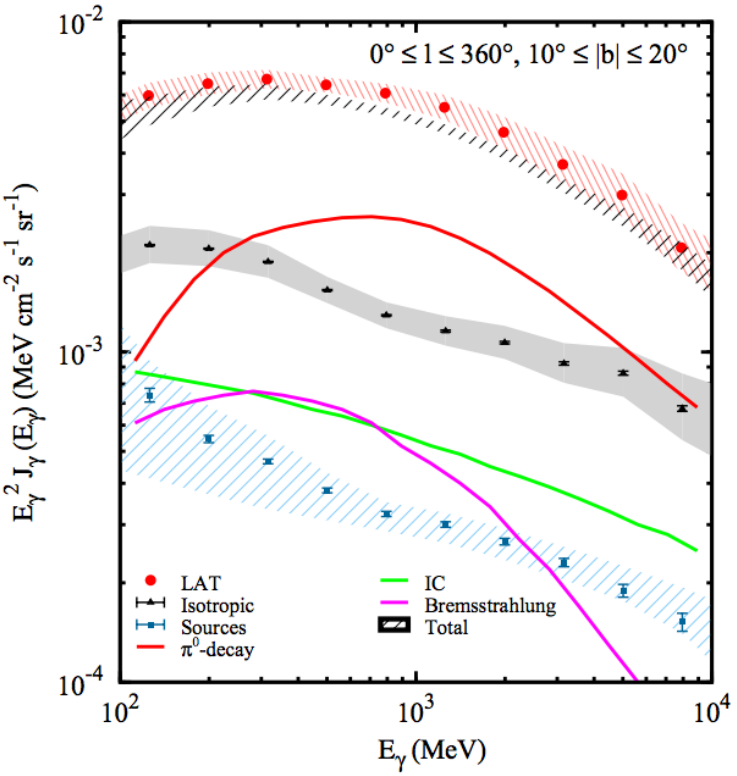

Figure 4.1: Fermi LAT data with an *a priori* model based on local cosmic-ray data and does not use γ-ray data, source, and unidentified background (UIB) components for sky region reported in the figure ($0° \leq l \leq 360°$, $10° \leq |b| \leq 20°$). The UIB component was determined by fitting the data and sources over all Galactic longitudes for the high-latitude region $|b| \geq 30°$ for the full LAT energy range. The modeled components are displayed with lines: π^0-decay (red), Bremsstrahlung (magenta), and IC (green). The areas represent: UIB (gray and solid area), source (blue and hatched area), and total made of UIB, source and model (black and hatched area). Fermi LAT data are red dots with red/hatched area as statistical error. Taken from Abdo et al. (2009a).

with thermal plasma inside accelerators.

The flux and energy spectrum of CRs are object of an intense study since their discovery in 1912 by Victor Hess. The energy spectrum of CRs extends to energies of about $\sim 10^{20}$ eV and even beyond as shown in Figure 4.2. The CR spectrum has two distinct features showed in Figure 4.2:

- a break at 2.3×10^{11} GeV (as suggested by Adriani et al., 2009, but not confirmed by recent observations with AMS)
- the so-called knee at $\sim 10^{15}$ eV
- a second knee at $\sim 10^{17}$ eV
- an ankle at $\sim 10^{19}$ eV.

. It is believed that all particles below the knee are of galactic origin for energetic reason as discussed in section 2.5.2: the expected energies reached inside the Galaxy extends at least to the knee. Furthermore, the UHECRs above the ankle are produced and accelerated outside of the Galactic Disk such as AGN, GRBs, young pulsars, Radiogalaxies and Clusters of galaxies (Aharonian, 2004). Beyond the ankle, powerful accelerators are needed which are supposed to be located outside the Galaxy.

The diffuse galactic γ-ray emission is the radiation components produced in interactions of electronic and nucleonic components of CRs with the interstellar gas and photon fields. The study of this component provides information about the density and energy spectra of CRs also in external galaxies. At the present state of art there are still unknown features on CRs (see section 2.5) mainly because it is not obvious that the locally observed CRs can be taken as representatives of the whole galactic population of relativistic particles. Furthermore, the identification and separation of the truly diffuse

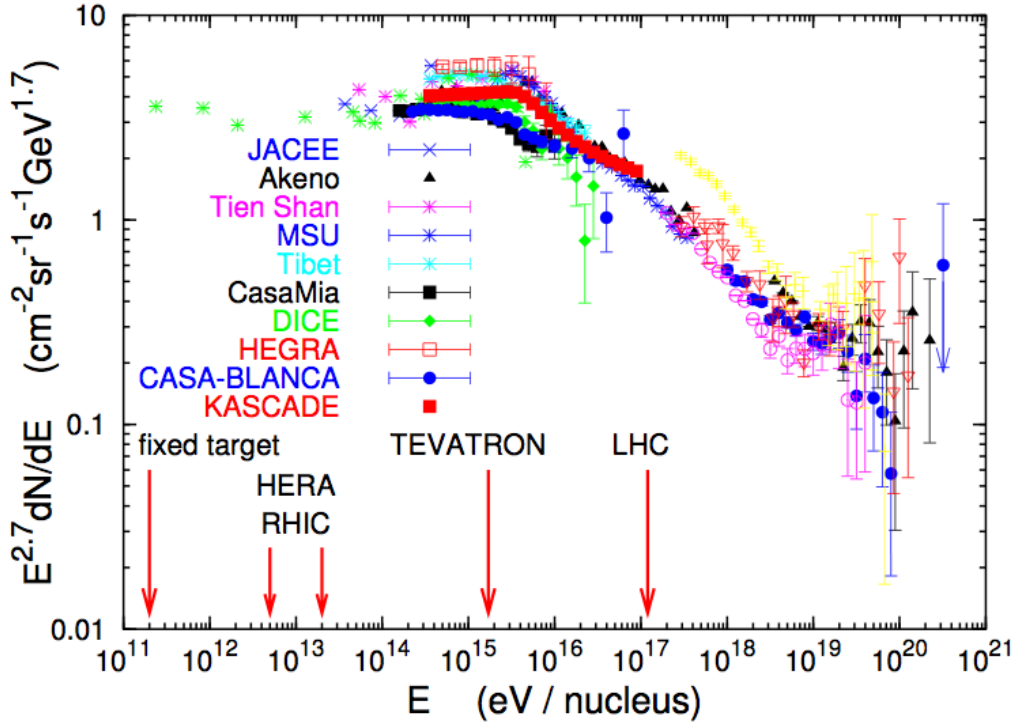

Figure 4.2: Summary of measurements of the all-energy spectrum of CRs. Taken from Aharonian (2004).

γ-ray emission is not an easy task because of a non-negligible contamination of weak unresolved discrete sources (e.g. Aharonian, 2004).

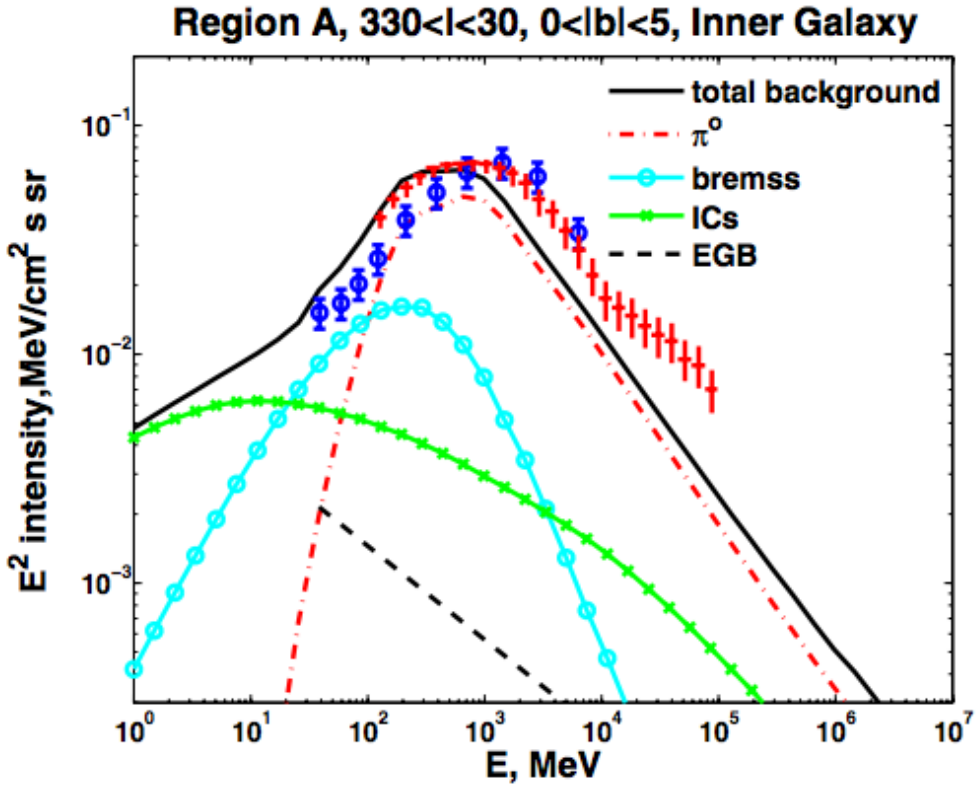

Figure 4.3: Spectra of diffuse γ-rays predicted by the propagation model for different sky regions. Blue dots are EGRET data, while red crosses are *Fermi*LAT data. Figure taken from Zhang et al. (2010)

The CR propagation equation for a particular particle species can be written as (e.g. Strong et al., 2007, and references therein):

$$\begin{aligned}\frac{\partial\psi(\vec{r},p,t)}{\partial t} &= q(\vec{r},p,t) + \vec{\nabla}\cdot(D_{xx}\vec{\nabla}\psi - \vec{\mathrm{V}}\psi) + \frac{\partial}{\partial p}p^2 D_{pp}\frac{\partial}{\partial p}\frac{1}{p^2}\psi \\ &- \frac{\partial}{\partial p}\left[\dot{p}\psi - \frac{p}{3}(\vec{\nabla}\cdot\vec{\mathrm{V}})\psi\right] - \frac{1}{\tau_f}\psi - \frac{1}{\tau_r}\psi \end{aligned} \quad (4.2)$$

where $\psi(\vec{r},p,t)$ is the CR density per unit of total particle momentum p at position $\vec{r}$, $\psi(p)dp = 4\pi p^2 f(\vec{p})dp$ in terms of phase-space density $f(\vec{p})$, $q(\vec{r},p)$

is the source term including primary, spallation and decay contributions, D_{xx} is the spatial diffusion coefficient, $\vec{V}$ the convection velocity, diffusive reacceleration is described as diffusion in moentum space and is deterined by the coefficient D_{pp}, $\dot{p} \equiv dp/dt$ is the momentum gain or loss rate, τ_f is the time scale for loss by fragmentation, and τ_r the time scale for radioactive decay.

4.3 The GALPROP code

To create model of propagation of CRs in the Galaxy some propagation codes or semi-analitical models can be used. A number of codes are developed to solve numerically the diffuse equation of CRs in Galactic environment. Among other, let us cite: DRAGON[3], USINE[4] or GALPROP. The *Fermi*LAT collaboration adopted the GALPROP code. GALPROP[5] is a code created to (Strong et al., 2007):

1. make simultaneous predictions of all relevant observation of CR nuclei, electrons and positrons, γ-rays and synchrotron radiation

2. prevent the limitations of analytic and semi-analytic methods and take advantage of the improvement in computing power as CR, γ-ray and other data become more accurate

3. include the current knowledge of the structure of the Galaxy and the source distribution.

[3] http://dragon.hepforge.org/DRAGON

[4] http://lpsc.in2p3.fr/index.php/fr/activites-scientifiques/ams-cream/codes/usine

[5] http://galprop.stanford.edu

I will give a brief overview of the GALPROP code taken from Strong et al. (2007) because is the code used within the *Fermi*LAT collaboration. Detailed information about this package are available in Strong and Moskalenko (1998) paper. The propagation equation 4.2 is solved numerically on a spatial grid, either in 2D with cylindrical symmetry in the Galaxy or in full 3D. The boundaries of the model in radius height, and the grid spacing are customizable. The distribution of CR sources can be freely chosen to represent SNR, being the mechanism to accelerate CR particles as described in chapter 2. Interstellar gas distribution are based on current H I, CO surveys and dust measurements, and the interstellar radiation field is based on a detailed calculation (Porter et al., 2008). The numerical solution proceeds in time until steady-state is reached.

First, the propagation equation is solved for heaviest nuclei (e.g. ^{64}Ni), then the solution is used to compute the source term for its spallation products. The solution is propagated in turn down to protons, secondary electrons and positron, and anti-protons.

Primary electrons are treated separately. Normalization of protons, helium and electrons to experimental data is provided. γ-rays and synchrotron are computed using interstellar gas data, for pion-decay and Bremsstrahlung, and the ISRF model for IC. Spectra of all the species are an output of the computation.

GALPROP goal is to be realistic. It includes crude approximations but it resorts the reality. This code does not calculate trajectories and does not consider presence of structures in the background, such as superbubbles. For these cases other techniques may be more appropriate, and they provide a future goal for further developments of GALPROP.

4.4 Modeling the background gamma-ray emission for the *Fermi* LAT high level analysis.

4.4.1 Interstellar diffuse emission

About 99% of the mass of the interstellar medium is gas and $\sim 90\%$ of this gas is made of atomic (H I) or molecular hydrogen (H_2). H I is traced by its $21-$cm line radiation, as described in section 4.1.1, H_2 has no dipole so cannot be directly observed in its cold phase, which is the dominant state in which we can find this gas. These lines are used to derive maps of the atomic hydrogen column density $N(H\ I)$, derived from the 21-cm line temperature under the assumption of a uniform spin temperature, and the molecular hydrogen column density $N(H_2)$, assumed to be proportional to the CO line intensities $W(CO)$.

For the *Fermi*LAT high level analysis I performed in chapter 5, the background model provided by the collaboration is based on two years of data taking. The model used to fit the γ-ray data is composed of linear combination of:

- atomic hydrogen from the all-sky Leiden-Argentina-Bonn (LAB) (Kalberla et al., 2005) composite survey. The column densities are derived assuming a constant spin temperature of 200 K
- velocity integrated CO intensities $W(CO)$ obtained from the Center for Astrophysics compilation (Dame et al., 2001)
- templates for IC emission obtained with the `GALPROP` code (see §4.3)
- dust optical depth maps used to account for gas not traced by the lines

- dedicated spatial templates for large-scale regions of excess emission such as: Loop I (including north spur region), Galactic lobes, galactic plane excess, earth limb events.

This can be done because energetic CRs uniformly penetrate all gas phases in the ISM. This interstellar emission model (IEM), along with sources of 2FGL catalog (Nolan et al., 2012), an isotropic intensity to take into account the extragalactic background and instrumental background, is fitted to the data. The templates are divided into six galactocentric rings (described in table **??**) to allow for Galactocentric gradient of cosmic-ray.

rings	r_{min} [kpc]	r_{max} [kpc]
1	0.0	4.0
2	4.0	5.5
3	5.5	7.0
4	7.0	10.0
5	10.0	16.5
6	16.5	50.0

Table 4.1: Galactocentric rings radius in kpc.

Fitting these models to γ-ray data, the differential emissivity or normalization for each template is derived. Summing the components, the Galactic

diffuse emission differential intensity in photons $\mathrm{sr}^{-1}\mathrm{s}^{-1}\mathrm{cm}^{-2}\mathrm{MeV}^{-1}$ [6]:

$$\begin{aligned}\frac{dI}{dE}(l,b) &= \sum_{i=rings} \frac{dq_{H\ I,i}}{dE} N_{H\ I}(r_i,l,b) + \sum_{i=rings} \frac{dq_{CO,i}}{dE} W_{CO}(r_i,l,b) \\ &+ \frac{dq_{EBV}}{dE} E(B-V)_{res}(l,b) + \frac{dq_{IC}}{dE} I_{IC}(l,b)\end{aligned}$$

where q is the emissivity of a particular component and E(B-V) the residual map,tracing the total dust column density, obtained after subtracting the part correlated to $N(H\ I)$ and $W(CO)$. The patches mentioned above are regions of spatially uniform intensity whose shapes reproduce the shape of the excesses in the γ-ray data. The intensity of the emission associated with each patch is fitted for each energy band together with the other templates.

For energies above 20 MeV the model has been extrapolated to fit the LAT data so the final model cube is made of 30 energy bins planes from 50 MeV to 600 GeV. The model provided by the collaboration gives the Galactic differential intensity in photons $\mathrm{sr}^{-1}\mathrm{s}^{-1}\mathrm{cm}^{-2}\mathrm{MeV}^{-1}$.

The standard IEM is distributed as a cube summed over the components which predicts the intensities of Galactic interstellar γ-ray emission in a grid of directions and energies with its accompanying isotropic model described in the next section.

4.4.2 Isotropic gamma-ray emission

An additional diffuse component with almost isotropic distribution in the sky is observed and known as the isotropic γ-ray background. Due to its uniformity over the sky, it is thought to be of extragalactic origin and referred to also as extragalactic γ-ray background (EGB). Most of it is attributed

[6] from *Description and Caveats for the LAT Team Model of Diffuse Gamma-Ray Emission* available at `http://fermi.gsfc.nasa.gov/ssc/data/access/lat/BackgroundModels.html`

to unresolved discrete sources. The most recent determination of the EGB spectrum based on LAT is reported in Dermer (2007). The dominant source classes that may explain the origin of EGB: blazars and radio/γgalaxies, interaction of CRs in star-forming galaxies, nonthermal radiation from clusters of galaxies and GRB not detected by the instrument. There may also be a truly diffuse component, not due to discrete sources due to cascades initiated by photo-pion or photo-pair production of ultra-energetic CRs interacting with photon of the extragalactic background light or cosmological DM.

From the above description of the extragalactic background it is clear that, for the *Fermi* LAT high-level analysis, also a template of the isotropic background is necessary. The model has to reproduce all the extragalactic γ-ray emission and also the CRs residual background: the residual intensity is obtained after fitting the diffuse Galactic γ-ray emission model components and the point sources.

The isotropic model is build fitting separately only the high latitude emission ($|b| > 30°$), to minimize the effects of the Galactic ridge that can be significant above 10°from the plane. This contamination is particularly severe at low energies because of the long tails of PSF.

An extrapolation of the data obtained, permits to continue the spectrum at energies grater than 100 GeV.

4.4.3 Models limitations

Several errors can affect the models used for the high-level analysis, specially the Galactic diffuse emission. The major limitations are:

- at low latitudes residuals obtained subtracting the model from the LAT data are non-negligible and clumpy

- the Galactic model does not include populations of unresolved Galactic point sources but they can be absorbed by some templates

- the diffuse model, for energies below 120 MeV was not fitted to the LAT data and it is less reliable

The CR residual background is handle as sources as γ-ray and the photon IRF are used. But the acceptance for residual charged-particle background is not the same as for gamma rays: the distribution of arrival directions in the instrument coordinates is not the same as for gamma rays and the assumption of being isotropic is only an approximation.

4.5 Systematic errors due to diffuse interstellar emission

To calculate uncertainties due to diffuse Galactic γ-ray emission (DGE) (described in sections 4.2 and 4.4.1), a grid of models is created. The idea of this grid was already used by Ackermann et al. (2012d) to compare the background maps obtained during the first 21 months of the *Fermi* mission with the diffuse background simulated using `GALPROP`.

The *Fermi*LAT collaboration developed eight alternative IEM to give an estimation of the systematic errors (de Palma et al., 2013). The model are build adopting a different model building strategy from the standard IEM, resulting in a different gas emissivities, or CO-to-H_2 and dust-to-ratios. Models are created using `GALPROP` code, described in section 4.3. To build these models a few parameters on the propagation model (`GALPROP`) are varied: the source distribution (Case and Bhattacharya, 1998 and Lorimer et al., 2006), the CR propagation halo heights ($z_h = 4$, 10 kpc) and atomic hydrogen spin

temperature (150 K and 10^4 K for optically thin hypothesis). It also allows more freedom in the fit by separately scaling the IC emission and H I and CO in 4 Galactocentric rings (for the definition of the rings see figure 4.4)

SNRs are believed to be the primary sources of Galactic CRs (see §2.5). However, their Galactic distribution is not well determined (Ackermann et al., 2012d). To account for this uncertainty, two different distributions of the SNRs are considered: the Case and Bhattacharya (1998)[7] and the Lorimer et al. (2006). The first is a measured SNR distribution, while the latter is the distribution of the pulsar. The distribution of the pulsar can be used because pulsars are an SN explosion end state.

The main uncertainty deriving the column densities is the spin temperature T_S used to correct the opacity of the 21 cm line. The T_S value used in the standard model for *Fermi* LAT analysis is 200 K. H I exists in a mixture of phases in the range between 40 K and a few thousand kelvin. Since the goal is to evaluate systematic uncertainties concerning the ISM model, two values for the T_S are chosen: 150 K and the optically thin assumption ($T_S \gg 150$ K). The choice of $T_S = 150$ K is motivated by the fact that the maximum observed brightness in the LAB survey is around 150 K and T_S must be greater than the observed brightness temperature (Ackermann et al., 2012d).

Since the X_{CO} factor may change with the Galactocentric radius, the spatial distribution is not well known, so we allow to vary in this analysis. To do that the template is divided into 4 Galactocentric annuli with boundaries: 0 kpc, 4 kpc, 8 kpc, 10 kpc and 30 kpc as shown in figure 4.4.

As reported by de Palma et al. (2013), this strategy for estimating sys-

[7]The validity of Case and Bhattacharya (1998) σ-D relation has been criticized but it is used as an alternative to probe the effect of changing the CR distribution.

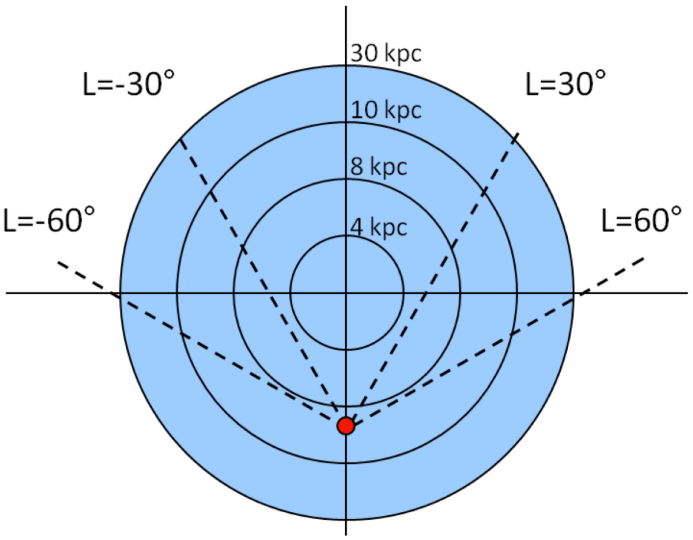

Figure 4.4: Schematic representation of the H I and CO rings used for split alternative IEMs crossed by line of sight at various Galactic longitudes. The dot marks the sun position at 8.5 kpc. The figure is not in scale. Picture taken from de Palma et al. (2013).

tematic uncertainty from interstellar emission modeling does not represent of systematics involved but this approach is able to obtain an indication about some important systematic effects. As stressed in Ackermann et al. (2012d), the study is limited due to the large number of DGE model parameters. Only diffusive-reaccelaration models are considered for CR propagation. In addition a smooth distribution of CR sources with homogeneous injection spectra is assumed (Ackermann et al., 2012d).

We perform the analysis already done with the standard background and we look at variations. In this way we are able to estimate the contribution to the systematic errors due to DGE.

Part II

Analysis and results

Chapter 5

Gamma-ray analysis

SNRs interacting with molecular cloud (MC) are of particular interest for the particle acceleration study. This because these kind of objects are the most likely candidates to accelerate Galactic CRs. Furthermore, high-energy γ-ray emission can pinpoint the presence of energetic leptons or ions and help to constraint the acceleration efficiency and maximum energy of accelerated particles. In particular I will present the analysis of HB 21 which present significant emission in γ-ray band and extended emission in both γ-ray and radio waveband. After an introduction in which I display the general information about HB 21 (section 5.1), I will describe the method used for morphological (§5.2.2) and spectral analysis (§5.2.5). In section 5.2.6, I will describe how we look for spectral variations across the remnant.

Most of the content of this chapter and of the next one have been published as Pivato et al. (2013).

5.1 General information about HB 21

HB 21 is a mixed morphology (MM) SNR, so it presents an inner part emitting in X-ray band and an outer shell emitting radio waves as shown in figure 5.1.

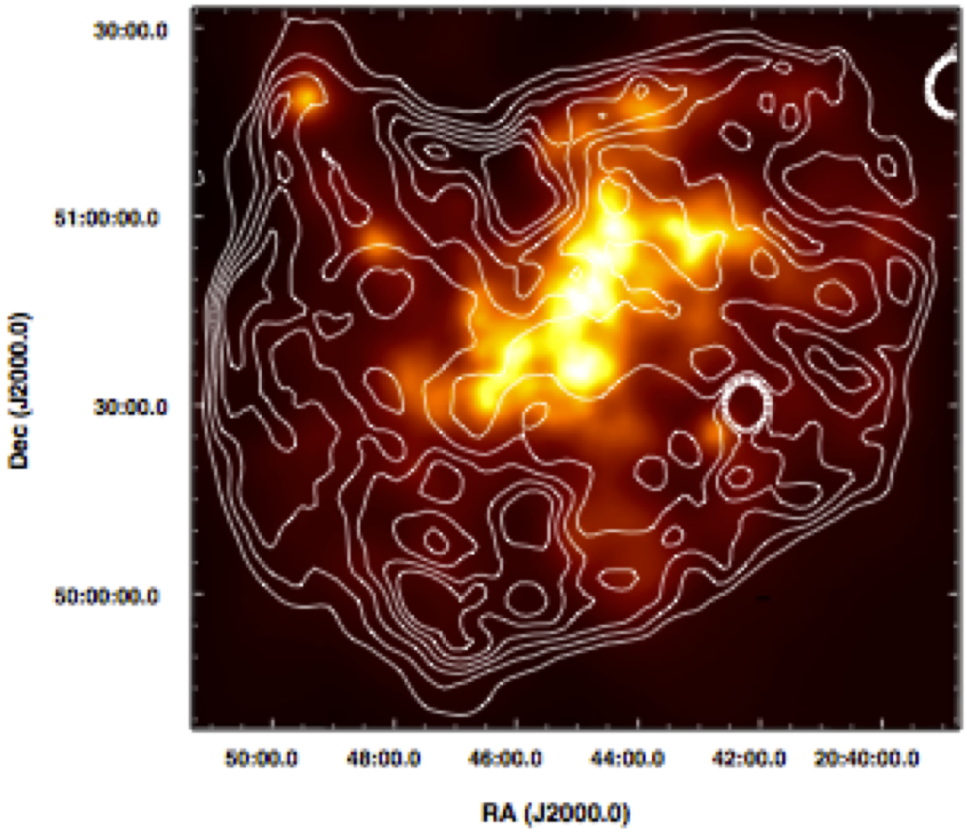

Figure 5.1: ROSAT X-rays image of HB 21. Superimposed there is the radio contours from emission at 408 MHz with the Canadian Galactic Plane Survey: they range from 0.455 Jy to 0.890 Jy. The intensity range of this image is $10^{-4} - 2.1 \times 10^{-2}$ counts s^{-1} $arcmin^{-2}$. From Pannuti et al. (2010).

In this section, I will give all the general information on HB 21 in order to better understand the behavior of the source and its spectrum. The interesting features are: the estimation of the distance (§5.1.1), of the age

(§5.1.2) and the evidences of interaction of the remnant with molecular clouds (§5.1.3).

5.1.1 Distance estimation

Estimating the distance of HB 21 is a non trivial problem to be solved and it is crucial to modeling its spectrum. HB 21 is located close to the line of sight of the MCs associated with the Cyg OB7 complex. Huang and Thaddeus (1986) and Dame and Thaddeus (1985) suggested that there is interaction between Cyg OB7 complex and HB 21 based upon its morphological appearance: the Cyg OB7 seems to surround the eastern and southern part of the SNR. They adopted the Cyg OB7 complex distance (0.8 kpc) as the distance of HB 21, but there are no direct evidences of the interaction between these two structures, so HB 21 distance appear to be only based on morphological appearance. In addition to that, there is a poor morphological correlation between CO and radio brightness as shown in Koo et al. (2001). For these reasons the estimation of the distance to HB 21 is still uncertain.

Byun et al. (2006) gives an estimation of the distance based on X-rays properties, pre-shock velocities, X-ray-absorbing column density and radio surface brightness.

Looking at X-rays properties of HB 21, Byun et al. (2006) propose a bigger distance of > 1.6 kpc. If the 0.8 kpc estimation is assumed, the X-ray surface brightness is too faint. In addition, the SN explosion energy derived considering this distance using X-ray data, is an order of magnitude lower than the canonical value of 10^{51} erg for SN explosions (Byun et al., 2006). To reproduce this value a greater distance of 1.7 ± 0.5 kpc is needed.

The pre-shock velocities of the shocked clouds can be used as distance indicators. Byun et al. (2006) estimate the pre-shock velocities for clouds

NW and S of -12 and -7 km s^{-1} respectively. Considering the Galactic rotation curve with a constant rotation velocity of 220 km s^{-1}, the kinematic distances of these two clouds are 3.0 and 2.3 kpc respectively.

Another method to estimate the distance is to use the X-ray-absorbing column density. The estimated velocity v_X or distance d_X is the velocity (or distance) where the actual accumulated column density becomes equal to the X-ray-absorbing column density. This value is derived from H I and CO observations. The HI column density is given by (Byun et al., 2006)

$$N(H\ I) = 1.82 \times 10^{18} T_S \int_{+50}^{r} \ln \left[1 - \frac{T_b(v)}{T_S} \right] dv \text{ cm}^{-2} \qquad (5.1)$$

where T_S is the spin temperature in K and v is in km s^{-1}. For the value of T_S, considering that HB 21 is located toward the Galactic are, Byun et al. (2006) choose 135 K. The accumulated column density is equal to the X-ray-absorbing column density at $v = -5.7^{+1.5}_{-1.8}$ km s^{-1}. In this estimation is not included the contribution of ionized hydrogen: to include it, the foreground column density of ionized hydrogen has to be calculated. Considering the electron number density of $n_e \approx 0.0019$ cm^{-3}, the foreground column density is $\sim 0.6(d/1 \text{ kpc})10^{20}$ cm^{-2}. With this correction the velocity becomes (Byun et al., 2006): $v_X = -4.9$ km s^{-1}. Again, applying a Galactic rotation curve and the galactocentric distance of the Sun (8.5 kpc), the corresponding distance is 2.0 ± 0.3 kpc.

Looking at radio emission, a closer distance is preferred. Considering the radio brightness of HB 21 and applying the Σ-D relation of Case and Bhattacharya (1998), Byun et al. (2006) obtain a diameter of 41 pc, and a distance of 1.3 kpc, even if it is known that Σ-D relation has an uncertainty of a factor 2 in both directions.

Considering all the available distances with their uncertainties, Byun et al. (2006) conclude that the distance of 1.7 ± 0.5 kpc is appropriate.

5.1.2 Age estimation

The estimation of the age is directly related to the distance of HB 21.

The model considered for MM SNRs invokes evaporation of clouds that are left relatively intact after the passage of the shock. In such case, the X-ray-emitting gas is due to dense embedded molecular material that evaporates in the SNR interior due to standard thermal conduction of the hot gas (Lazendic and Slane, 2006). The remnant is considered still in an adiabatic phase and the post-shock temperature is related to the observed temperature in X-ray gas in the Sedov phase, scaled with a factor A (Lazendic and Slane, 2006):

$$T_s = AT_{\mathrm{Sedov}} = 0.78kT_X A \tag{5.2}$$

where T_s refers to the case in which electron-ion equilibrium is assumed. The relation for the temperature of shocked gas with adiabatic index $\gamma = 5/3$ is used to derive the velocity of the blast wave (Lazendic and Slane, 2006):

$$v_s = \left(\frac{16kT_s}{3\mu m_H}\right)^{1/2} \tag{5.3}$$

where $\mu = 0.604$ is the mean atomic weight, and the age of the remnant is

$$t = \frac{2r_s}{5v_s} \tag{5.4}$$

where r_s is the radius of the blast wave.

Using this method, which is highly dependent on the SNR model applied, Lazendic and Slane (2006) obtain $v_s = 670 \pm 33$ km s^{-1} and HB 21 age is $5000 - 6000$ yr.

If the angular size of the radio shell is used, the age is ~ 7000 yr (Lazendic and Slane, 2006).

The estimation of Lazendic and Slane (2006) is done assuming a distance of 0.8 kpc. As told in the previous section, we adopt a distance of 1.7 kpc so

the age has to be corrected considering this distance. The age of HB 21 is obtained scaling the $\sim$ 7000 yr at 0.8 kpc to the value at 1.7 kpc using the relation (Byun et al., 2006):

$$t_{SNR} \sim 1.5 \times 10^4 d_{1.7} \text{ yr} \tag{5.5}$$

which gives an age of $\sim 1.5 \times 10^4$ yr.

5.1.3 Interaction with molecular clouds

Koo et al. (2001) report the presence of shocked molecular clouds in the SNR HB 21. The evidences ranges from a morphological evidence to the detection of broad and/or shock excited emission lines from the various molecules. This last feature is of crucial importance to understand the physical and chemical processes associated with the molecular shock.

In figure 5.2 it is shown a map of the CO emission overlaid with the radio emission of the remnant. The broad lines (showed in figures 5.3b and 5.3c) are presumably emitted from the shocked gas which is located in warm dense clumps with significant column densities so that the 2-1 lines are optically thick (Koo et al., 2001).

There is no evidence for interaction of the SNR with molecular clouds along the eastern boundary.

This can be one hint to search spectral variations across the remnant also in γ-rays as done in section 5.2.6 As told before, HB 21 is a MM SNR. There is a strong association between MM SNRs and evidence for interactions between shock fronts and dense clouds revealed by OH masers (Yusef-Zadeh et al., 2003). Therefore, MM SNRs are good candidates to be bright γ-ray sources.

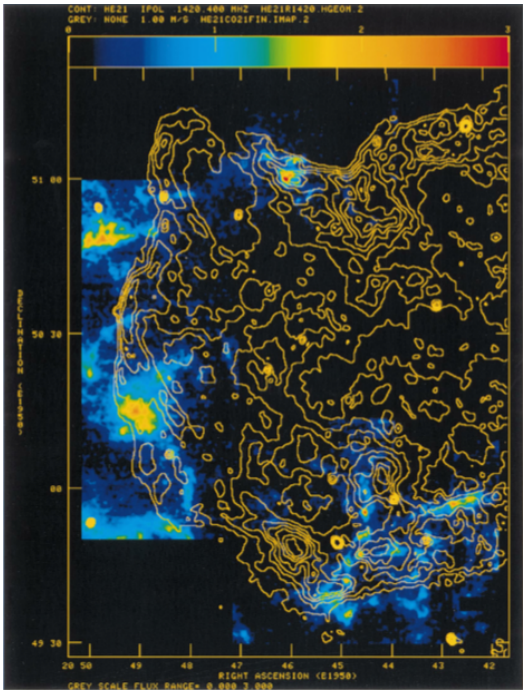

Figure 5.2: ^{12}CO integrated intensity map of HB 21. The velocity ranges from $v = +3.9$ to -17.5 km s^{-1}, and the integrated intensity varies from 0 to 64 K km s^{-1}. Overlaid there is the 1420 MHz brightness map obtained with the TRAO synthesis telescope. Figure from Koo and Heiles (1991).

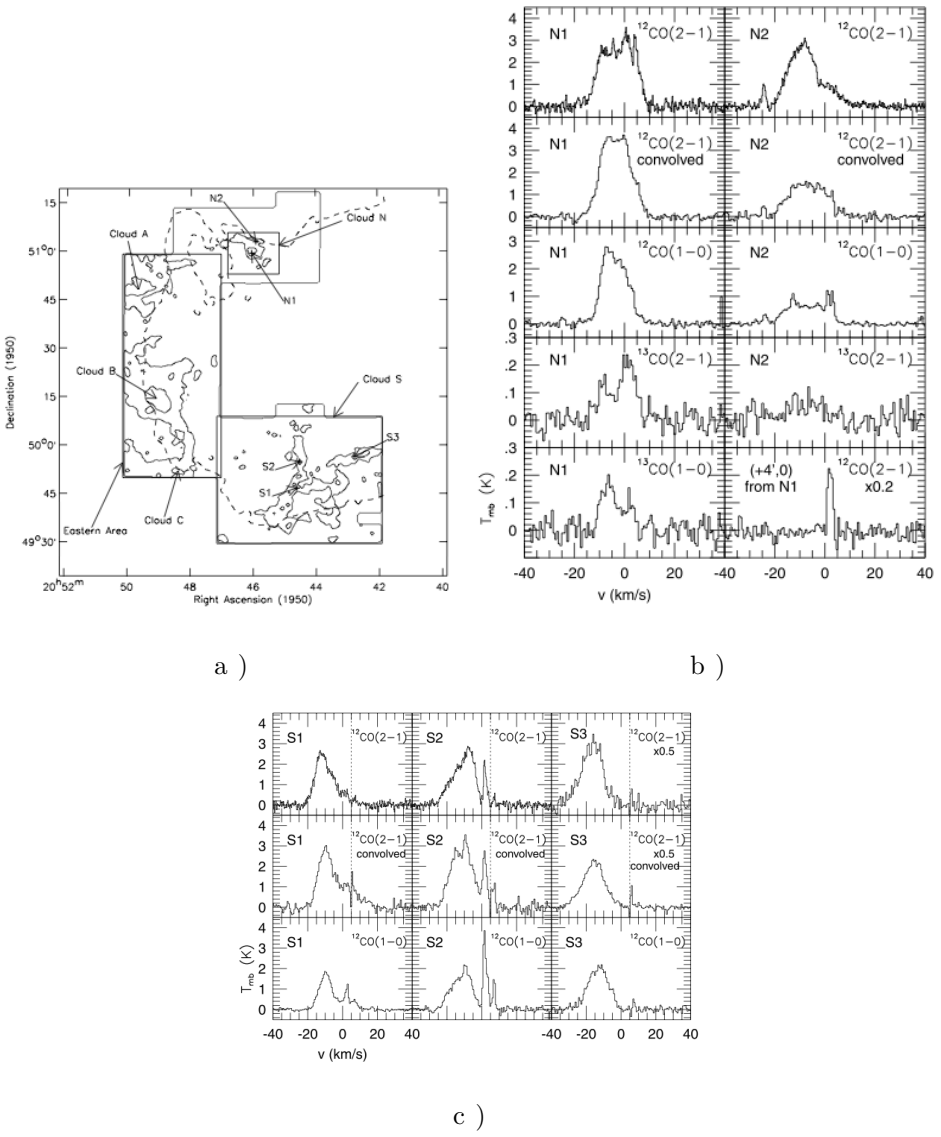

Figure 5.3: Maps of the position of the CO peaks and their spectra. a) Chart of the position of the CO peaks. b) CO spectra of the northern peak position N1 and N2. c) CO spectra for the southern peaks S1, S2 and S3. From Koo and Heiles (1991).

5.2 *Fermi* LAT analysis

In this section I will describe the *Fermi* LAT analysis performed for this source. In particular, after describing the data set used (§5.2.1), I will describe morphological and spectral analysis (sections 5.2.2, 5.2.6 and 5.2.5).

5.2.1 *Fermi* data set and background

Data for this analysis are accumulated from the beginning of scientific operations on 2008 August 4 to 2012 June 14, selecting the low-background `P7SOURCE` event class. The data analysis is performed using the LAT Science Tools package (v9r27p1), available from the Fermi Science Support Center[1]. For the morphological characterization we use only events with energy > 1 GeV to profit from the narrower PSF in order to separate the γ-ray emission associated with HB 21 from neighboring sources and interstellar emission. We then use events down to 100 MeV to determine the spectral energy distribution of the remnant. Below this energy the PSF becomes much broader than the SNR and the uncertainties related to the instrument response are larger. In both the morphological and spectral characterization we consider photons with measured energies up to 300 GeV, but only find a significant detection of the source up to energies of several 100 GeV due to the limited number of events at high energies. I perform the analysis in a 10×10 RoI centered at the radio position of HB 21 ($l = 89.^{\circ}0$, $b = +4.^{\circ}7$). The RoI approximately corresponds to the 68% event containment region for the `P7SOURCE` events at 100 MeV and exceeds the 95% event containment region for energies $\gtrsim 700$ MeV (see figure 3.6). I adopt this narrower than usual RoI in order to limit at the lowest energies the large uncertainties due

[1] `http://fermi.gsfc.nasa.gov/ssc`

to the modeling of the bright interstellar emission from the nearby Cygnus region (Ackermann et al., 2011, 2012c). I also exclude a few time intervals when the LAT boresight was rocked with respect to the local zenith by more than 52°(mostly for calibration purposes or to point at specific sources) and events with a reconstructed angle with respect to the local zenith $> 100°$ in order to limit the contribution from the Earths atmospheric γ-ray emission. To take into account the latter selection criterion in the calculation of the exposure, I exclude time intervals when any part of the RoI was observed at zenith angles $> 100°$.

The background is composed of diffuse emission and individual nearby γ-ray sources. Diffuse emission is taken into account using the standard models provided by the *Fermi* LAT collaboration[2] for the `P7SOURCE` selection (see Nolan et al., 2012). They include a model that accounts for the Galactic interstellar emission from CR interactions with interstellar gas and low-energy radiation fields, and an isotropic background spectrum that accounts for diffuse γ-ray emission of extragalactic origin and residual background events due to charged particle interactions in the LAT misclassified as γ-rays (for details see chapter 4). I leave the normalization of the Galactic interstellar model as a free parameter, yet fix the isotropic background spectrum because it is difficult to separate it from the other components in such a small RoI and it is more reliably determined over larger regions of the sky.

I include in the background model all the point sources present in the 2FGL catalog (Nolan et al., 2012) with distances less than 15° from the RoI center and which are not associated with the SNR. I will discuss in section 5.2.2 the case of the source 2FGL J2051.8+5054, which is located at the edge of the SNR. The spectral models used for background sources are those

[2] `http://fermi.gsfc.nasa.gov/ssc/data/access/lat/BackgroundModels.html`

reported in the 2FGL catalog. Fluxes and spectral indices are left as free parameters in the fit if the source is within the RoI. Otherwise they are fixed to the catalog values.

The background model and the various models for HB 21 are fitted to the LAT data using a binned maximum-likelihood method based on Poisson statistics (e.g. Mattox et al., 1996), as implemented in the *gtlike* tool (see section 3.5). For this purpose data were binned on an angular grid with $0^{\circ}.1$ spacing, and different binning in energy as detailed below. The analysis uses the post-launch IRF `P7SOURCE_V6` (Ackermann et al., 2012a).

5.2.2 Morphological analysis

As a first step to perform an accurate analysis with the *Fermi* LAT data is the morphological analysis. We notice that in the 2FGL catalog, there are 3 sources associated to HB 21 and an additional source (2FGL J2051.8+5054) is located at the edge of the γ-ray emission. The aim of this analysis is double: on one hand I want to understand if the γ-ray emission is likely due to a single extended source or from different point sources, and on the other hand, I want to understand which is the best fit template for the future γ-ray analysis.

In figure 5.4a I show a count map of the RoI for energies > 1 GeV, to visually illustrate the morphology of the γ-ray emission in the region. Figure 5.4b shows the model I adopt to take into account the background and figure 5.4c is what remains from the difference between the two previous maps: in this way we can isolate the emission from the source we want to analyze.

The first model I consider is the one composed of only point sources; the three point sources associated at HB 21 in the 2FGL catalog are: 2FGL J2043.3+5105, 2FGL J2041.5+5003 and 2FGL J2046.0+4954. In addition to the point-

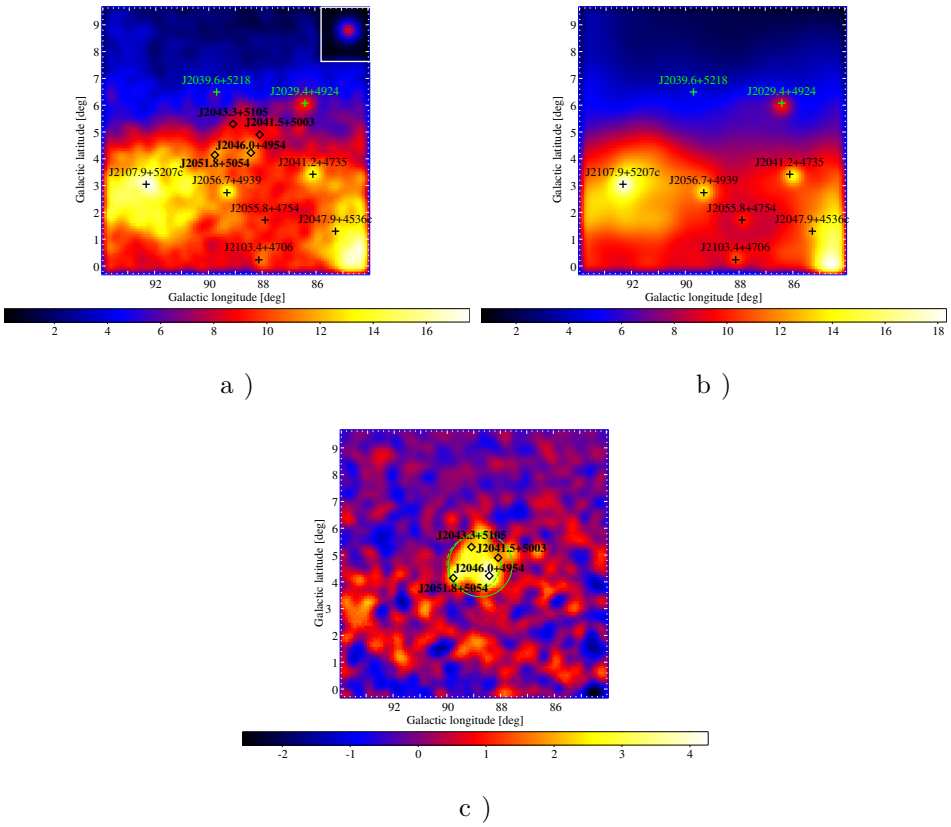

Figure 5.4: a) LAT counts map at energies $>$ 1 GeV with color scale in counts/pixel. We overlaid the positions of 2FGL sources (crosses for background sources and bold diamonds for the three sources associated with the remnant and 2FGL J2051.8+5054). The inset in the top right corner shows the effective PSF over the energy range considered for a power-law spectral distribution with index 3.1. b) Background model map (calculated using the best-fit parameters from the case where HB 21 was modeled as a disk). c) Remaining emission associated with HB 21; overlaid are the positions of the four point sources above, the best-fit disk (solid line) and the radio disk (dashed line). The pixel size is 0.°1 and all maps are smoothed for display with a Gaussian kernel of σ=0.°4.

sources-only model, I consider three different spatial template: the disk, the radio emitting region (figure 5.8a) and the X-ray emitting region (figure 5.8b). For each model we evaluate the test statistic

$$\mathrm{TS} = 2(\ln \mathcal{L}_1 - \ln \mathcal{L}_0) \tag{5.6}$$

where $\mathcal{L}_1$ is the maximum-likelihood value for the model including the remnant and $\mathcal{L}_0$ is the maximum-likelihood value for the model not including it (null hypothesis). If the null hypothesis is verified (no γ-ray emission associated to HB 21), TS is expected to be distributed as a χ^2 with a number of degrees of freedom given by the additional number of free parameters in the model including the source, with the caveats discussed in Protassov et al. (2002). For a detailed description of the maximum likelihood analysis, see section 3.5.2.

To investigate if the additional source is part of the emission of the remnant or is a source itself I perform the maximum likelihood fit including in the model also the 2FGL J2051.8+5054 for each spatial template.

The results obtained are reported in table 5.1. If I compare the TS with the model in which HB 21 is modeled by the point sources in the 2FGL Catalog (Table 5.1) I find that the extended source provides a higher likelihood for a lower number of free parameters in the fit. Therefore, I conclude that the hypothesis of extended emission is preferred over four individual point sources. All the spatial templates are fitted with a power-law spectrum.

I determine the position and extension of the γ-ray emission associated with HB 21 from γ-ray data only using the *pointlike* tool, which is optimized and widely validated against Monte Carlo simulations for this purpose (Lande et al., 2012).

I model the source as a disk with a power-law spectrum and I determine the position of its center (l, b) and radius r, along with flux and spectral index

Table 5.1: Test statistic (TS) and degrees of freedom (d.o.f.) for the different spatial models for the γ-ray emission associated to HB 21 considered in 5.2.2.

sources	TS	d.o.f.
Null hypothesis	0	0
4 point sources	256	10
disk	302	5
disk + 2FGL J2051.8+5054	316	7
X-ray image	212	2
X-ray image+ 2FGL J2051.8+5054	234	4
radio image	298	2
radio image + 2FGL J2051.8+5054	312	4

from LAT data, using an energy binning of 8 bins per decade. I considered both the cases where 2FGL J2051.8+5054 is included as a separate point source in the model or removed.

The TS for the case including separately 2FGL J2051.8+5054 in the model is larger by 14 than the case with the disk only (Table 5.1). The significance of the separate source hypothesis is below the threshold usually required to claim a detection for LAT sources (TS$>$ 25). Deeper observations are needed to determine if 2FGL J2051.8+5054 can be distinguished as a source independent from the remnant. In the rest of the analysis, we do not consider 2FGL J2051.8+5054 as a separate source and, therefore, we remove it from the model.

I note that the results concerning the morphology of HB 21 are robust regardless of whether 2FGL J2051.8+5054 is included as a separate source in the model or not.

Using the best fit disk, the significance of the detection of HB 21 is $\sim 29\sigma$.

I also check parameters for disk plus additional source hypothesis and single disk. In the first case I obtain $l = 88.^{\circ}62 \pm 0.^{\circ}05$, $b = 4.^{\circ}79 \pm 0.^{\circ}06$, and $r = 1.^{\circ}14 \pm 0.^{\circ}07$. In the second I have $l = 88.^{\circ}75 \pm 0.^{\circ}04$, $b = 4.^{\circ}65 \pm 0.^{\circ}06$, $r = 1.^{\circ}19 \pm 0.^{\circ}06$. Errors reflect statistical uncertainties only.

In Figure 5.4b I show the background model map obtained from the fit with the disk, and in Figure 5.4c the background-subtracted count map where the emission associated to HB 21 is visible.

For both radio and X-ray templates I compare the cases when 2FGL J2051.8+5054 is included in the fit as a background source or not.

From the results reported in table 5.1 I confirm that the morphology of the remnant in γ-ray significantly differs, as expected, from the emission in X-rays. Both the radio template and the γ-ray disk provide a good fit to the data, though the first has less degrees of freedom, as shown in table 5.1. Since the two models are not nested it is not possible to conclude which is the best one.

I also check if the source size changes with energy. I do that separately fitting a disk to the LAT data from 1 to 3 GeV and from 3 to 10 GeV. I obtain $r = 1.^{\circ}19 \pm 0.^{\circ}09$ in the lower-energy range and $r = 1.^{\circ}24 \pm 0.^{\circ}09$ in the higher-energy range. No significant change in size with energy is detected.

Given that the disk model provides the largest TS of all single source models, and is derived from the γ-ray data, I use this model to compute the spectrum of the remnant.

For the best fit γ-ray disk I also computed the systematic errors as described in sections 3.4.2 and 4.5. I just consider errors due to interstellar emission model, because IRFs variations does not affect the determination of the disk characteristics but they just give a variation on the flux calculated

from the data.

When the alternative interstellar emission models are used, the γ-ray disk is systematically shifted toward the north-west part with respect to the radio shell (with shifts in longitude between $0.^{\circ}19$ and $0.^{\circ}24$, and in latitude between $0.^{\circ}06$ and $0.^{\circ}09$), and the disk radius is systematically smaller by $0.^{\circ}18 - 0.^{\circ}24$ as summarized in figures 5.5 and 5.6. The significance of the detection of HB 21 does not change sizably.

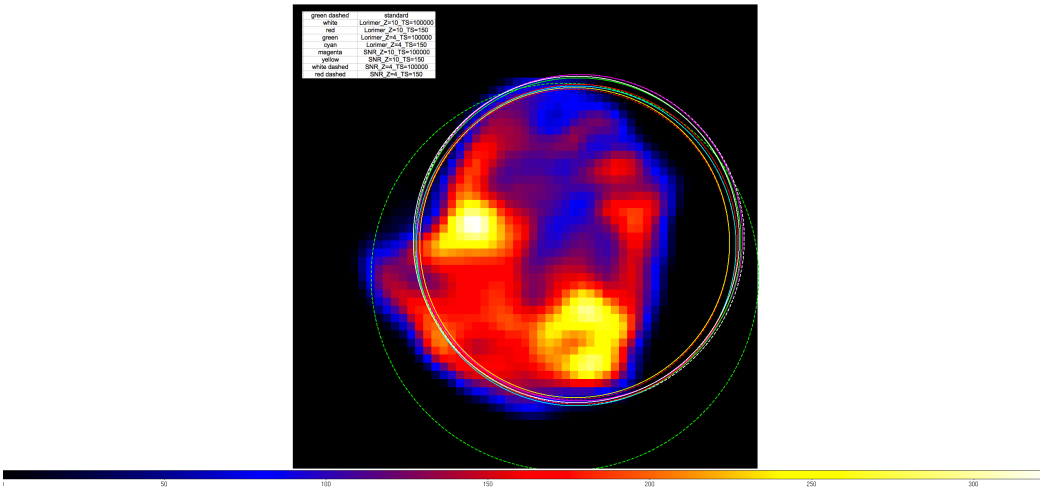

Figure 5.5: Disk obtained fitting the model with the alternative background emission. The alternative disks are compared with the radio emission at 6-cm.

This effect is mainly due to the different approaches used to deal with the dark gas, neutral interstellar gas which is not well traced by the linear combination of column densities inferred from the 21-cm H I line and the 2.6-mm CO line, but which is traced by correlated residuals in dust emission/absorption and interstellar γ-ray emission (Grenier et al., 2005). Dust residuals are used as a dark-gas template fitted to the γ-ray data in the standard interstellar model, whereas they are used to correct the H I column

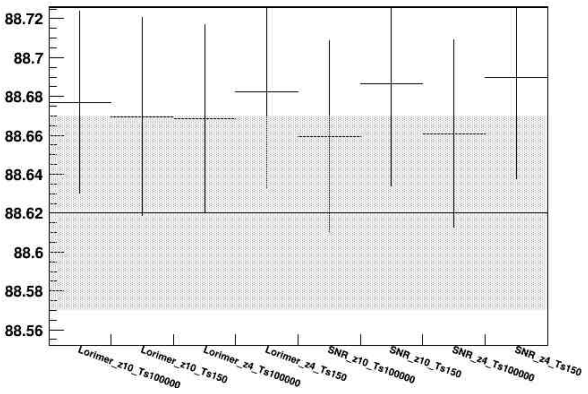

a) L parameter in degrees

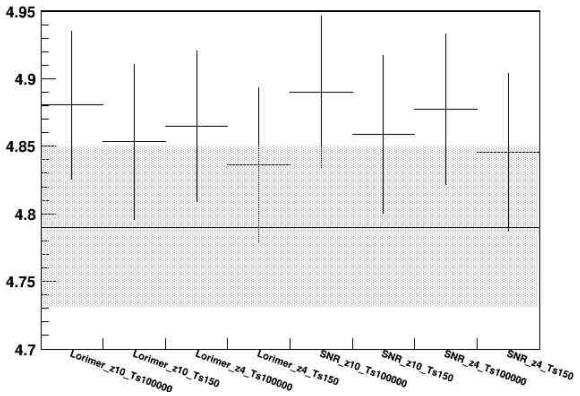

b) B parameter in degrees

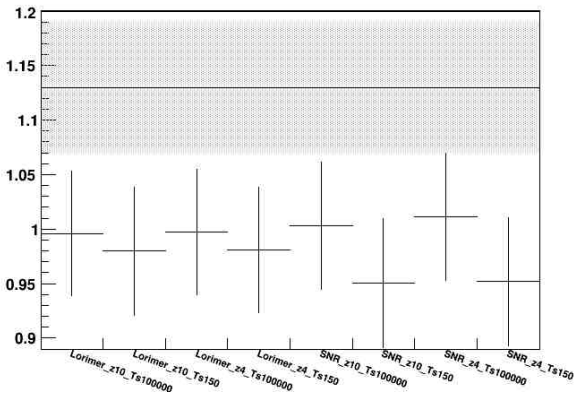

c) radius of the disk in degrees

Figure 5.6: Values of the coordinates and radius of the disk, changing the diffuse intestellar model. The errors reported are statistical only. The straight line is the value obtained with the standard background.

densities in the alternative models assuming a dust-to-gas ratio independent from γ-ray observations. This excess in the alternative models respect to the standard background is clearly visible in figure 5.7. This leads to different estimates of the gas column densities, therefore to different structures in the interstellar emission models. Additionally, the standard model accounts for enhanced interstellar emission toward the nearby Cygnus X complex (see Ackermann et al., 2011, 2012c), whereas the alternative models do not. These differences are found to have a significant impact on the determination of the SNR morphology.

I note that for all the alternative models the disk extends beyond the rim of the remnant in coincidence with the western molecular cloud, but leave the faint south-east edge of the radio shell off as shown in figure 5.5.

5.2.3 Comparison with other wavelengths

As told before, HB 21 is a MM SNR interacting with molecular clouds.

In figure 5.8 I compare the γ-ray emission associated with HB 21 to emission from the remnant at other wavelengths. Figure 5.8a compares the γ-ray image with radio emission at 6-cm tracing non-thermal electrons.

Figure 5.8b compares the γ-ray morphology with X-ray emission from the thermal plasma filling the center of the remnant, measured by ROSAT (Voges et al., 1999). The ROSAT image was cleaned using the standard background maps[3].

Finally figure 5.8c compares the γ-ray emitting region with the distribution of molecular material. Molecular column densities in the Local-Arm region are traced by the CO line intensities at $2.6-$ mm (Dame et al., 2001; Dame and Thaddeus, 2011) integrated over velocities with respect to the lo-

[3]Available from `http://www.xray.mpe.mpg.de/cgi-bin/rosat/rosat-survey`

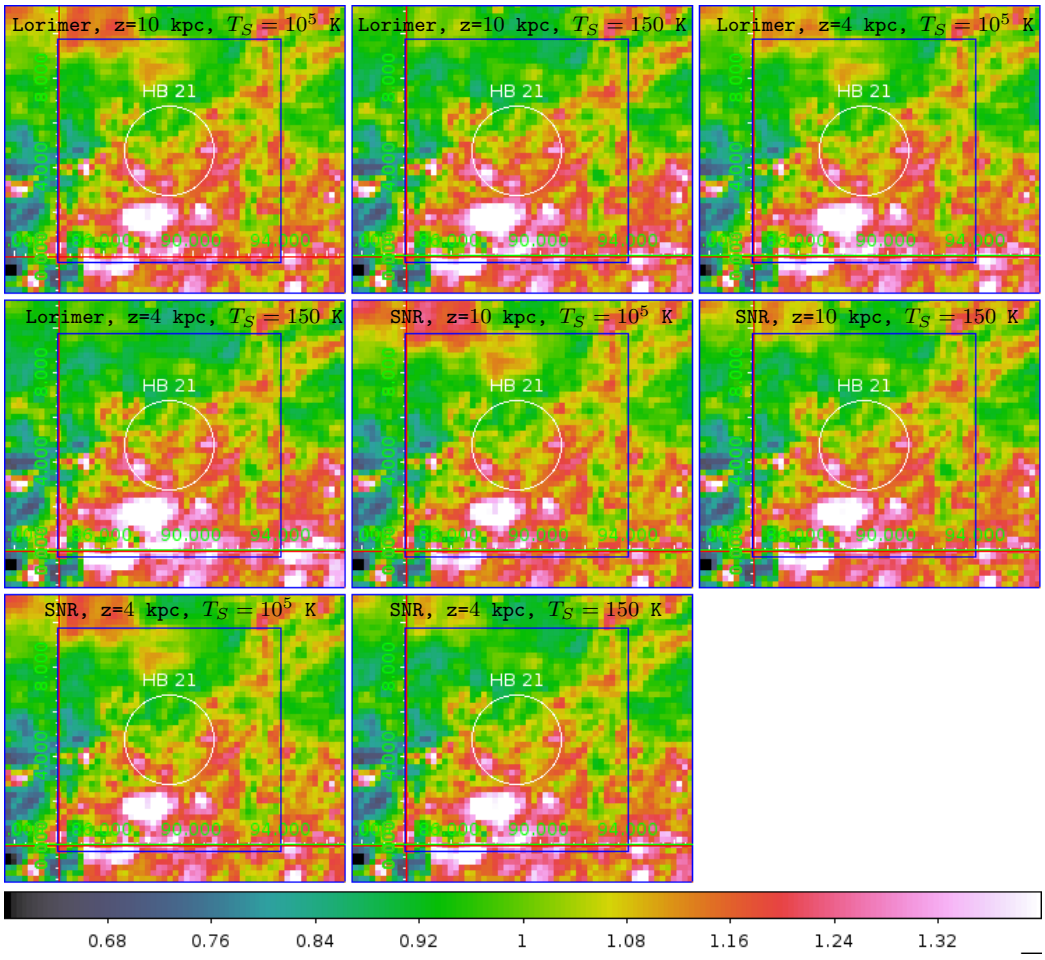

Figure 5.7: Ratio of the alternative background emission, respect to the standard intestellar diffuse model at 1 GeV. The circle is 2° around HB 21, and the box is a 10° × 10° RoI.

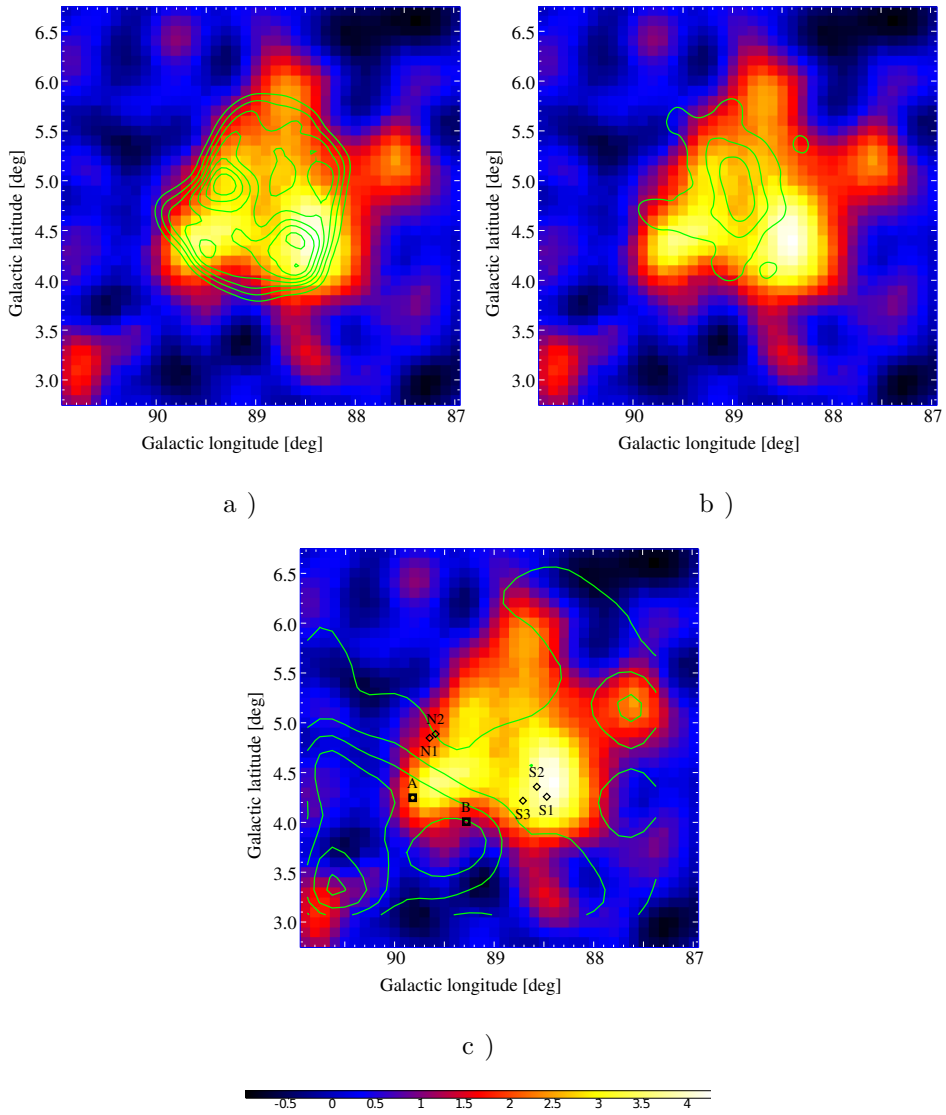

Figure 5.8: Emission associated with HB 21 overlaid with contours from emission at other wavelengths (see text for details): a) Radio emission intensity at $6-$ cm with a beam size of $0.^{\circ}16$, smoothed with a Gaussian kernel with σ=$0.^{\circ}2$. The seven contour levels are linearly spaced from 0 to 2.0 Jy beam^{-1}. b) Background-subtracted X-ray emission (ROSAT) smoothed with a Gaussian kernel of $\sigma = 0.^{\circ}25$. The three contour levels are linearly spaced from 0.36×10^{-3} to 2.13×10^{-3} counts s^{-1} arcmin^{-2}. c) Intensities of the 2.6-mm CO line in the Local-Arm region. The six contour levels are linearly spaced from 1.5 K km s^{-1} to 28 K km s^{-1}. We also show the positions of the shocked CO clumps (diamonds) and clouds A and B (squares) given in Koo and Heiles (1991).

cal standard of rest within ± 20 km s^{-1}. I also show the positions of shocked CO clumps and of two large CO clouds distributed along the boundary of the radio shell (Koo and Heiles, 1991).

The γ-ray emission associated with HB 21 is broader than the central region filled by thermal X-ray emitting plasma. It compares well with the radio shell, but appears to extend beyond the radio shell in regions where molecular clouds are present. The brightest γ-ray regions coincide with the Southern shocked CO clumps identified by Koo and Heiles (1991). This correlation with CO suggests that at least part of the γ-ray emission from HB 21 may be produced by accelerated particles colliding with dense interstellar matter.

5.2.4 PSR J2047+5029

As most of the SNRs, also HB 21 presents a neutron star in its shell. We note that the radio pulsar PSR J2047+5029 is $0.^{\circ}5$ away from the remnants radio center (Janssen et al., 2009). While pulsars represent the largest Galactic γ-ray source class, this particular pulsar likely contributes no detectable flux to the RoI. I test this hypothesis adding a point source (in coincidence of the radio pulsar) in the model and fitting it. The spectrum shape used is a power-law with exponential cutoff. Looking at the TS value I obtain < 1 so the source does not have a significant emission in γ-ray.

To strength this assumption we also look at the pulsar characteristics obtained form the radio data. The spindown power is $\dot{E} \sim 2 \times 10^{33}$ erg s^{-1}, lower than that of any known γ-ray pulsar, and three times lower than for any young, radio-loud γ-ray pulsar (Abdo et al., 2013). That is, the pulsar is probably below the deathline expected from the outer magnetospheric emission models that best describe the LAT pulsars (Wang and Hirotani, 2011). Furthermore, the pulsar's dispersion measure indicates a distance

$D = 4.4$ kpc. The ratio $\sqrt{\dot{E}}/D^2 = 2.3 \times 10^{15}$ erg$^{1/2}$ kpc^2 (a proxy of the expected γ-ray luminosity) is five times lower than for any known γ-ray pulsar (see fig. 15 in Abdo et al., 2013). We also check the two-year LAT catalog, but it shows no point source at the pulsar position Nolan et al. (2012), nor does the 4-year catalog currently in preparation.

Nevertheless, we searched PSR J2047+5029 for γ-ray pulsations. It is not part of *Fermi*'s pulsar timing campaign (Smith et al., 2008), so we obtained a timing solution based on Westerbork Synthesis Radio Telescope (SRT) and Jodrell Bank radio data taken concurrently with the *Fermi* data[4]. The ephemeris will be presented in future work (Janssen et al. 2013). We used it to phase-fold the LAT data, over a grid of minimum energy cuts (100 MeV to 1000 MeV, in 50 MeV steps) and maximum radius cuts (from 0.°4 to 2°from the pulsar position, in 0.°1 steps). For pulsars with unknown γ-ray spectral shapes and unknown pulse profile shapes, such grids amount to a search for the maximum pulsar signal-to-background noise ratio. At each grid location, we calculated the H-test, which never exceeded 3σ statistical significance (see section 5 in Abdo et al., 2013). The pulsars energy flux above 100 MeV is therefore lower than for any known γ-ray pulsar, that is, below 2×10^{12} erg cm^2 s^{-1}.

We conclude that the pulsar can be neglected when characterizing γ-ray emission from HB 21.

5.2.5 Spectral analysis

I want to understand which is the best spectral shape to fit the LAT data.

The spectral energy distribution (SED) of HB 21 is determined over the full energy range between 100 MeV and 300 GeV and using 35 logarithmic

[4]Janssen, and Stappers private communication

energy bins for the likelihood analysis. The γ-ray emission is modeled with the best-fit disk as described in section 5.2.2.

To do that I compare the hypothesis of a power law

$$\frac{dN}{dE} = N_0 \left(\frac{E}{100 \text{ MeV}} \right)^{-\Gamma} \tag{5.7}$$

with three different curved spectral models, in order to quantify the deviation from the former spectrum, calculating the TS value for each case.

The three functional forms considered are:

1. log-parabola

$$\frac{dN}{dE} = N_0 \left(\frac{E}{1000 \text{ MeV}} \right)^{-(\alpha+\beta \ln(E/1000 \text{ MeV}))} \tag{5.8}$$

2. smooth broken power law

$$\frac{dN}{dE} = N_0 \left(\frac{E}{100 \text{ MeV}} \right)^{-\Gamma_1} \left(1 + \left(\frac{E}{E_b} \right)^{(\Gamma_2-\Gamma_1)/0.2} \right)^{-0.2} \tag{5.9}$$

   with Γ_1 and Γ_2 being the spectral indices below and above the break energy E_b, respectively

3. power law with exponential cutoff

$$\frac{dN}{dE} = N_0 \left(\frac{E}{200 \text{ MeV}} \right)^{-\Gamma} \exp\left(-\frac{E}{E_c} \right) \tag{5.10}$$

   where E_c is the energy cutoff.

I computed the TS for each alternative model compared to the power-law hypothesis with the curved hypothesis. In table 5.2 we report the values obtained.

All the curved models have a higher TS than the power law distribution. For the following discussion I adopt the log-parabola because it yields the

Table 5.2: TS and additional d.o.f. for the different functions used to model the SED of HB 21. For each model we report the values of the best-fit parameters.

spectrum shape	ΔTS	additional d.o.f.	fit parameters
power law	0	0	$\Gamma = 2.33 \pm 0.03$
log-parabola	92	1	$\alpha = 2.54 \pm 0.05$
			$\beta = 0.39 \pm 0.04$
smooth broken power law	41	2	$\Gamma_1 = 1.67 \pm 0.02$
			$\Gamma_2 = 3.54 \pm 0.05$
			$E_b = 789 \pm 65$ MeV
power law with exponential cutoff	82	1	$\Gamma = 1.42 \pm 0.03$
			$E_c = 958 \pm 41$ MeV

largest improvement with respect to the simple power-law, with a $\Delta TS = 92$, corresponding to an improvement at a $\sim 9\sigma$ significance level in the energy range from 100 MeV to 300 GeV. The total γ-ray energy flux from HB 21 results to be $9.4 \pm 0.8(\text{stat}) \pm 1.6(\text{syst}) \times 10^{11}$ erg cm^2 s^{-1} and the photon flux $1.48 \pm 0.2(\text{stat}) \pm 0.4(\text{syst}) \times 10^7$ ph cm^2 s^{-1}. The systematic errors shown in this section are calculated perfoming the analysis with the alternative models and extracting the root mean square of the variations with respect to the values from the standard model. For completeness, I report the systematic errors due to interstellar emission model on all the fit parameter of HB 21: the results are shown in figure 5.9.

As shown in the figure 5.9a, Γ_1 index is systematically lower in the alternative models fit even if they are compatible within the statistical errors. Also Γ_2 index is systematically smaller fitting with the alternative models as shown in figure 5.9b. For what concern the fluxes, they are all compatible within the erros with the value obtained fitting with the standard IEM (see figure 5.9c). These values are due to the different background considered: variations in components of diffuse emission, produce variations in the indeces of spectrum.

I also computed the SED in a model independent way. I split the energy range between 100 MeV and 60 GeV into 12 logarithmically spaced bins. The model used is the same as the all energy range fit, but, for the source I use a power law spectral model, instead of the curved spectrum and I let free only the fluxes. Other spectral parameters are fixed to the 2FGL values for background sources and to a power-law index of 2 for HB 21 (the results are insensitive to this particular choice). When TS for an individual bin is < 9, I calculate an upper limit at the 95% confidence level determined through the likelihood profile method.

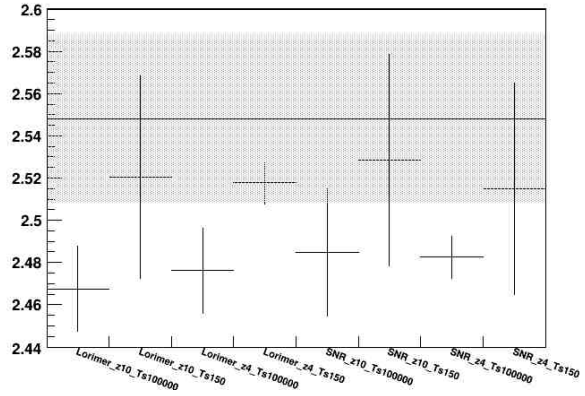

a) Γ_1 index

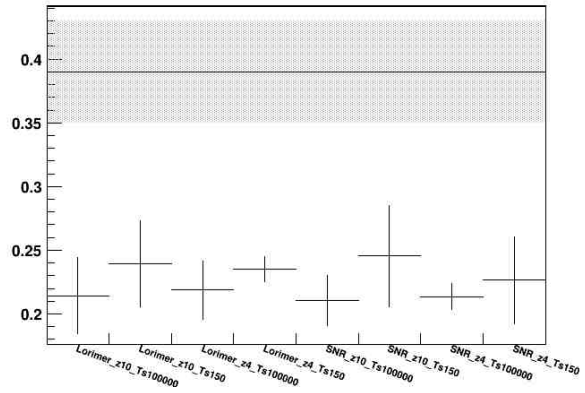

b) Γ_2 index

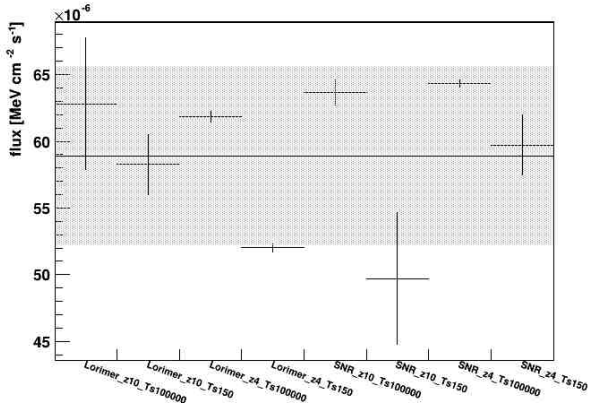

c) flux

Figure 5.9: Values of the fit parameters, changing the diffuse intestellar model. The errors reported are statistical only. The straight line is the value obtained with the standard background.

I show the resulting SED in figure 5.10 with also systematic errors indicated. Systematic errors due to interstellar emission model are then summed in quadrature with the error due to the LAT effective area uncertainties for display. The SED points are reported in table 5.3. The contributions due to the modeling of interstellar emission and the LAT effective area are presented separately. In the energy range considered, the systematic errors are driven by the interstellar emission model. This independent way to compute the SED confirm that the spectrum is curved as showed in the global fit.

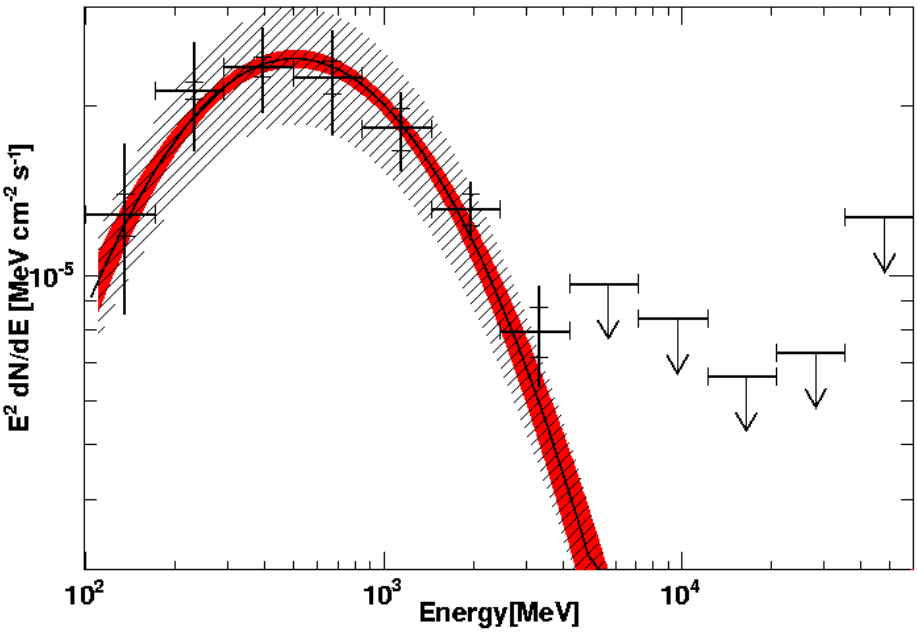

Figure 5.10: Spectral energy distribution of HB 21. The line shows the best-fit log-parabola model, the light-red filled area shows the statistical error band and the dashed gray area shows the systematic uncertainties. The bar markers correspond to statistical errors only, while lines show the larger systematic errors. 95% confidence-level upper limits are given for energy bins where the TS of the source is < 9.

Bin-per-bin fit pinpoint the presence of a cutoff or a break in the γ-ray dat: as will be discussed in section 6.4, this is a common feature in middle age or old SNRs.

Table 5.3: SED of γ-ray emission from HB 21. For each SED point we report the systematic uncertainties separately for those related to IEM and LAT EA, as well as the overall uncertainty obtained by summing them in quadrature.

Energy bin center [MeV]	E^2dN/dE [eV cm^{-2} s^{-1}]	statistical [eV cm^{-2} s^{-1}]	IEM [eV cm^{-2} s^{-1}]	EA [eV cm^{-2} s^{-1}]	Total syst. [eV cm^{-2} s^{-1}]
135	12.8	$\pm$1.1	$\pm$4.1	$\pm$1.2	$\pm$4.3
230	21.3	$\pm$0.8	$\pm$4.3	$\pm$1.8	$\pm$4.7
393	23.5	$\pm$0.9	$\pm$3.8	$\pm$1.6	$\pm$4.1
670	22.5	$\pm$1.5	$\pm$4.6	$\pm$1.1	$\pm$4.8
1143	18.3	$\pm$1.5	$\pm$2.7	$\pm$0.9	$\pm$2.9
1959	13.1	$\pm$0.9	$\pm$1.4	$\pm$0.7	$\pm$1.6
3326	7.9	$\pm$0.8	$\pm$1.5	$\pm$ 0.5	$\pm$1.6

5.2.6 Search for spectral variations across the remnant

HB 21 is known to interact with molecular clouds (§5.1.3) so the interaction between particles accelerated by the SNR shock and the environment can pinpoint the presence of CRs. A sign of this interaction in γ-rays could be the variations of the emission spectrum across the emitting region. HB 21 is a good candidate to perform this analysis because it is spatially resolved by the *Fermi* LAT.

To further investigate this hypothesis, I repeat the spectral analysis, as described in section 5.2.5 but splitting the best fit γ-ray disk into two or three parts. The decision on how to split is taken looking at the overlays of figure 5.8 and considering CO clouds as a preferred targets for CRs escaping form the SNR. In 2012, Reichardt et al. claim a $\sim 2\sigma$ spectral variation across the remnant: they fuond this value splitting the disk emitting region into three parts. Even though such splitting forms slices too small to be well resoled by the LAT, I check also this hypothesis to confirm or reject their results. The splittings are showed in figure 5.11 and are:

1. radio-emitting area (modeled with a uniform disk centered at $l = 89.^{\circ}0$ $b = +4.^{\circ}7$ with radius 1°) and the remainder of the best-fit disk (figure 5.11a);

2. southern shocked-CO region (modeled as a uniform disk centered at $l = 88.^{\circ}38$ $b = 4.^{\circ}50$ and radius $0.^{\circ}35$) and the remainder of the best-fit disk (figure 5.11b);

3. disk split into two halves to separate the southern shocked CO area from the rest (figure 5.11d);

4. finally, I test the division proposed by Reichardt et al. (2012) splitting the uniform disk into three subregions covering 120° each (figure 5.11e).

First I perform the analysis from 1 GeV to taking advantage of the better PSF of the LAT (see figure 3.6). For this first analysis I uses a power-law model: looking at figure 5.10, I notice that, above 1 GeV, the spectrum can be approximated with a power law function. The results are reported in table 5.4 where I also reported the values of the indexes for each region for completeness.

Table 5.4: Likelihood values and spectral indices for the models described in §5.2.6, splitting the single bestfit disk in different subregions. For each case we report the number of d.o.f. and the spectral indices. Analysis performed above 1 GeV.

model considered	ΔTS	Δd.o.f.	index region 1	index region 2	index region 3
single disk	0	0	3.09 ± 0.12		
a	2.8	2	2.98 ± 0.12	3.35 ± 0.10	
b	4.2	2	2.88 ± 0.31	3.14 ± 0.15	
c	2.2	2	2.86 ± 0.40	3.29 ± 0.10	
d	1.6	4	2.92 ± 0.22	3.29 ± 0.21	2.95 ± 0.17

As shown in table 5.4, there are no significant improvement in likelihood in splitting the disk into to or more parts as suggested from the ΔTS values which indicate a significance in sub-splitting less than 2σ. This means that there is no evidence of spectral variations across the γ-ray emitting region. In addition, the indeces of the subregions are all compatible within statistical uncertainties.

Then I perform also an analysis over the full energy range from 100 MeV

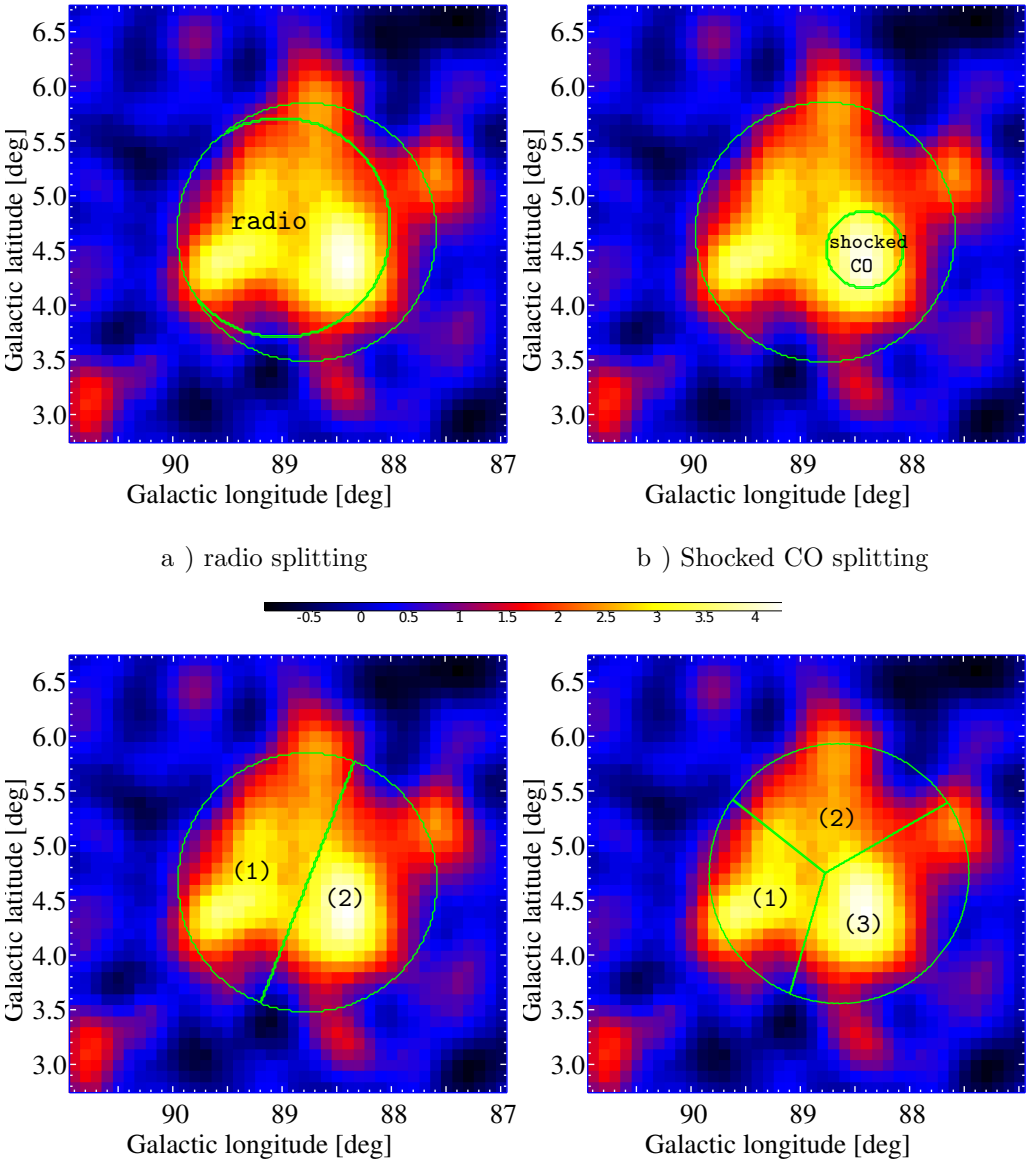

a) radio splitting

b) Shocked CO splitting

d) half disk splitting

e) splitting as Reichardt et al. (2012)

Figure 5.11: Emission associated with HB 21 as in fig. 5.4c overlaid with the boundaries of the templates used in the search for spectral variations across the remnant described in 5.2.6.

to 300 GeV. Each subregion is fitted using a log-parabolic function as the uniform disk and normalization and indeces are set as free parameters. Also in this case, I report the results in table 5.5 where also the fit parameters of the log-parabola are reported.

Table 5.5: Likelihood values and spectral indices for the models described in §5.2.6, splitting the single bestfit disk in different subregions. For each case I report the number of d.o.f. and the spectral indices. Analysis performed above 100 MeV.

model considered	ΔTS	Δd.o.f.	α	β
single disk	0	0	2.54 ± 0.05	0.39 ± 0.04
a	13	3	$\alpha_{radio} = 2.41 \pm 0.09$	$\beta_{radio} = 0.37 \pm 0.06$
			$\alpha_{other} = 3.48 \pm 0.89$	$\beta_{other} = 0.74 \pm 0.39$
b	13.4	3	$\alpha_{CO} = 2.27 \pm 0.06$	$\beta_{CO} = 0.38 \pm 0.04$
			$\alpha_{other} = 2.61 \pm 0.21$	$\beta_{other} 0.43 \pm 0.03$
c	8	3	$\alpha_1 = 2.47 \pm 0.06$	$\beta_1 = 0.36 \pm 0.03$
			$\alpha_2 = 2.64 \pm 0.09$	$\beta_2 = 0.45 \pm 0.03$
d	3	6	$\alpha_1 = 2.35 \pm 0.15$	$\beta_1 = 0.38 \pm 0.10$
			$\alpha_2 = 2.75 \pm 0.29$	$\beta_2 = 0.39 \pm 0.17$
			$\alpha_3 = 2.53 \pm 0.18$	$\beta_3 = 0.43 \pm 0.13$

Also in this case I don't see any evidence of spectral variation across the remnant: the only evidence is marginal, less than 3σ and the values of the indices are compatible within the statistical errors. In this case, as in the fit above 1 GeV, I do not consider systematic uncertainties because they are irrelevant: they don't add any new information on spectral indeces variations.

In conclusion, I do not confirm the claim by Reichardt et al. (2012) of a softer spectrum toward the clouds NW and A. Spectral variations are not significant ($< 3\sigma$), even considering statistical uncertainties only. More data and a better handling of the current dominating uncertainties related to the modeling of interstellar emission (that were neglected in the study of Reichardt et al., 2012) are required in order to further probe for possible γ-ray spectral variations across HB 21.

Chapter 6

Radio data analysis and non-thermal modeling of HB 21

Radio data are useful to constrain non-thermal emission models of HB 21. This because particles emitting in radio via synchrotron emission. From their spectrum, we can infer the electron distribution. Then, electrons, interacting with the CMB photons and the material around HB 21, produce γ-ray radiation. In this chapter, using also the WMAP data (§6.1), I will describe the non-thermal modeling of HB 21 (§6.3) and a comparison with other SNR detected by *Fermi* (§6.4).

6.1 WMAP analysis: observations and analysis

The radio morphology of HB 21 is shown in figure 5.8a and has the shape of a large oblate shell. It has large angular diameter and high radio flux, so it is a favorable target for observations with radio telescopes. High-resolution imaging reveals bright filaments and indentations along the periphery (Leahy and

Roger, 1998). The 7-year all-sky data of the *Wilkinson Microwave Anisotropy Probe* (WMAP) are used to extend the radio spectrum of HB 21 above 10 GHz. Five bands are analyzed with effective central frequencies (ν_{eff}) of 23 to 93 GHz Jarosik et al. (2011).

The RoI is a square $4^\circ \times 4^\circ$ centered in the radio coordinates of HB 21. For the modeling a spatial template plus a sloping planar baseline was used, following Hewitt et al. (2012). For the spatial template we use the map of HB 21 from the Sino-German 6-cm (at 4.8 GHz) survey (Gao et al., 2011, resolution of $9.5'$), shown, as overlay, in figure 5.8a.

On the background, there is a point source: 3C 418 (Hill, 1974). To include it, a separate, free-normalized point source was included in the model to account for the bright nearby extragalactic source. The templates are smoothed to the WMAP beam at each band (Weiland et al., 2011) and fit to the data.

Figure 6.1 shows an example of the WMAP skymap, best-fit model and residual map for the Q band (61 GHz). Table 6.1 lists the beam sizes and fitted fluxes with errors estimated from the root mean square (RMS) of the fit residuals. The addition of a template for 3C 418 does not produce a significant change in the measured fluxes of HB 21.

The global radio spectrum of HB 21 from 38 MHz to 93 GHz is shown in figure 6.2. This WMAP analysis was included along with published flux densities from the literature (Kothes et al., 2006, and references therein). It is evident that a spectral break is present in the spectrum at high frequencies. The radio spectrum was first fitted with a single power law, $S(\nu) = S_0\nu^{-\alpha}$ and to find a flux normalization at 1 GHz of $S_0 = 201 \pm 3$ Jy and an index $\alpha = 0.50 \pm 0.02$. The fitted index is significantly steeper than $\alpha = 0.38$ determined from fitting only the data below 10 GHz because it does not

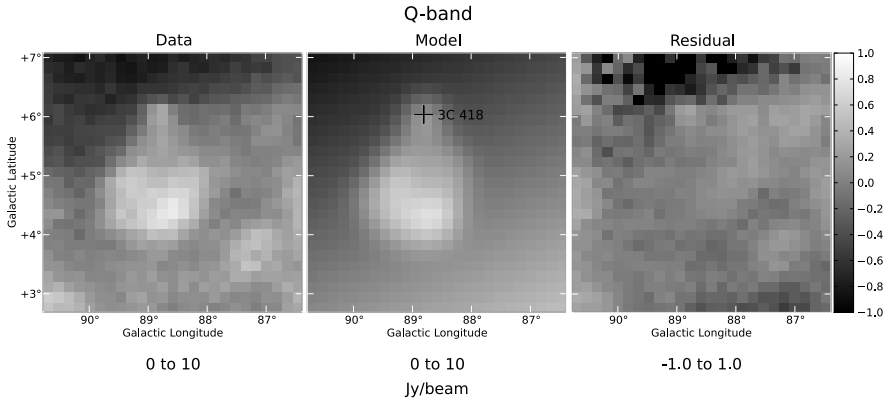

Figure 6.1: Example of the template fit to the WMAP data within a 4° square region of HB 21 in the Q band (61 GHz). The three panels present the 7-year skymap image (left), the model resulting from a fit of the radio template plus a sloping planar baseline and a point source at the position of 3C 418 marked by a cross (center), and the fractional residuals (defined as the fit residual divided by the model). The upper and lower limits of the linear color bar are given beneath each image; data and model are on the same scale.

Table 6.1: WMAP Flux Density for HB 21. Five bands are analyzed with effective central frequencies (ν_{eff}) of 23 to 93 GHz (see section 6.1).

Band	ν_{eff} [GHz]	beam FWHM [°]	Flux density [Jy]
K	22.7	0.93	34 ± 3
Ka	33.0	0.68	24 ± 4
Q	40.6	0.53	20 ± 5
V	60.5	0.35	17 ± 8
W	93.0	0.23	56 2σ upper limit.

account for the break at high frequencies.

Then a spectral break of $\Delta\alpha = 0.5$ at a frequency ν_b was included in the spectral model. This is appropriate for synchrotron losses in a homogeneous source of continuously injected electrons, as expected for middle-aged SNRs (Leahy and Roger, 1998; Reynolds, 2009, section 2.1). Including one additional free parameter, the model produce a good fit to the radio spectrum. The spectral break has a significance of 5.3σ by applying the F-test to compare the χ^2 fit to that of the simple power-law. The best fit parameters for the radio spectrum of HB 21 are $\alpha = 0.38 \pm 0.02$ and $\nu_b = 5.9 \pm 1.2$ GHz. Additionally, the spectrum was also fitted using a power law with an exponential cutoff of the form, $S(\nu) = S_0 \nu^\alpha \exp(\nu/\nu_c)$. This produces nearly as good a fit, with $\alpha = 0.34 \pm 0.02$, $\nu_c = 29 \pm 4$ GHz, and a significance of 5.2σ.

The radio index, α, is related to the particle index, Γ_p, by $\Gamma_p = 2\alpha + 1$. The observed radio index below the break $\alpha = 0.38$ gives $\Gamma_p \sim 1.8$, which is similar to the spectral index obtained with the *Fermi* LAT data in §5.2.5. We explore physical mechanisms which could explain both the γ-ray and radio

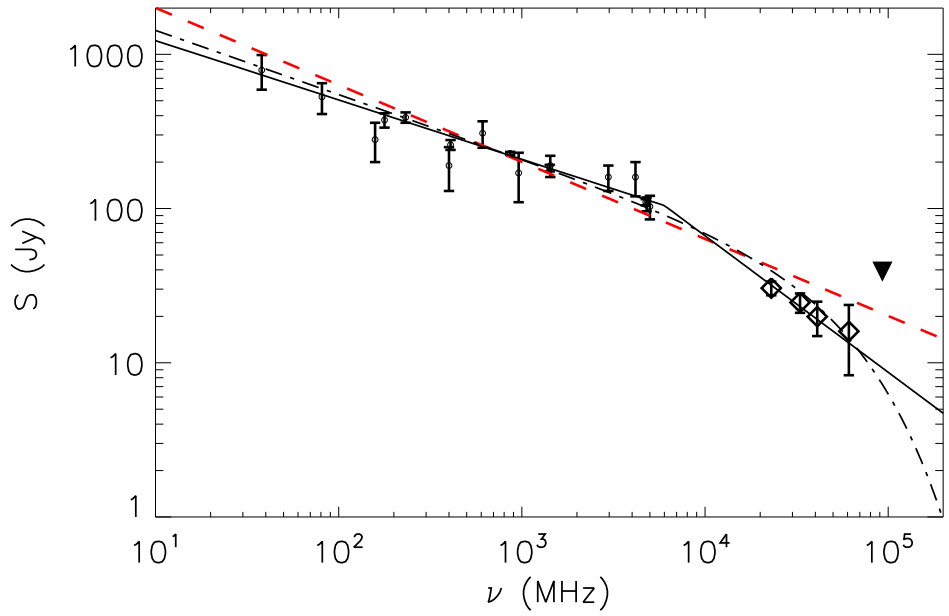

Figure 6.2: Integrated radio flux density of HB 21 as a function of frequency. Data points below 10 GHz, circles, are from the literature (see Kothes et al., 2006, and references therein). The new WMAP data points are shown as open diamonds and presented in table 6.1. The upper limit is shown as a downward filled triangle. The dashed red line shows a power-law fit to the entire radio spectrum. The solid black line shows a fit to the data assuming a spectral break as described in the text. The dot-dashed black line shows the fit assuming an exponential cutoff.

spectra in the discussion in §6.3.

The observed break in the high-frequency spectrum cannot be explained by spectral variations across HB 21. Leahy (2006) studied spectral variations using radio observations at 408 and 1420 MHz. Manual fits to 36 individual regions across the SNR show variations between 0.2-0.8, with a mean spectral index of 0.45 and a standard deviation of 0.16. The brightest regions tend to have an index that is flatter than average and than the canonical spectral index (0.5) from diffusive shock acceleration. Thus, fitting the radio spectral index of the flux from the entire remnant leads to an even flatter global index of 0.38.

6.2 Physical environment around HB 21and emission mechanism

Before starting with the non-thermal modeling of HB 21 spectrum, a deeper knowledge of the physical environment around the emitted area is needed.

The presence of optical [SII] but not oxygen line emission indicates slow shocks < 100 km s^{-1} into ambient densities of at least 2.5 cm^{-3} (Mavromatakis et al., 2007). Shocked CO filaments are observed with densities of order $\sim 10^2 - 10^4$ cm^{-3} and small filling factors ≤ 0.1 (Koo et al., 2001). For neutral gas, the mean ambient H I density for the expanding shell is ~ 8 cm^{-3} at the considered distance. Reichardt et al. (2012) estimated the molecular mass within HB 21 by integrating all CO line emission between the velocity range from +0 to 20 km s^{-1}. This estimate likely includes molecular gas outside the SNR, but is a conservative upper limit. Adopting a distance of 1.7 kpc as discussed in section 5.1.1, the maximum molecular mass is 5.5×10^4 $M_\odot$, the diameter of the SNR is 55 pc, and the maximum

volume-averaged molecular gas density is 25 cm^{-3}. Therefore, we assume a gas density of 15 cm^{-3}, noting that this is uncertain by a factor of a few.

To model the source we have to understand which are the physical mechanism that can produce γ-ray emission in SNRs. There are three primary mechanisms which can be classified into two scenarios: the hadronic scenario and the leptonic scenario. In the so-called hadronic scenario the emission is dominated by γ-ray radiated through the decay of π^0 mesons produced in collisions between accelerated nuclei with the ambient gas (see §2.4.4). In the leptonic scenarios γ-ray emission results either from IC scattering of relativistic electrons on low-energy photon fields such as the CMB (§2.4.2), or non-thermal bremsstrahlung (§2.4.3). As the matter density increases, the bremsstrahlung contribution will rise and dominate over the IC at densities $\gtrsim 1$ cm^{-3}, unless the photon field is greatly amplified above the CMB. HB 21 appears to have a high enough gas density that bremsstrahlung is expected to dominate over IC emission. In modeling the non-thermal spectrum of HB 21 we explored models in which the assumed physical conditions are modified such that each of these three emission mechanisms is dominant.

6.3 Non-thermal modeling

We have identified spatially extended γ-ray emission coincident with SNR HB 21 indicating the presence of relativistic particles. Determining the mechanism responsible for γ-ray emission is crucial in order to measure the underlying particle population accelerated by the SNR. To do so, we model emission from the remnant using `isis`, the *Interactive Spectral Interpretation System* (Houck and Denicola, 2000). Non-thermal models of emission from relativistic particles are included for arbitrary particle momentum distribu-

tions (Houck and Allen, 2006) which are then fit to radio and γ-ray data. The included prescriptions are in agreement with the results from Sturner et al. (1997).

To constrain the emitting particle distribution we simultaneously fit radio and γ-ray emission from non-thermal electrons and protons. We analyze two different scenario: first we analyze the one-zone model in which the emission originates from an area equal to the best-fit γ-ray disk (see §6.3.1). But HB 21 is knowing to interact with molecular clouds (§5.1.3) so we also analyze the hypothesis in which the emission is from two different area (see §6.3.2).

6.3.1 One-zone model

Initially, we adopt the simplifying assumption that all emission originates from a region characterized by a constant matter density and magnetic field strength. This single emitting zone is assumed to be equal to the size of the remnant derived from the best-fit γ-ray disk. Additionally, the population of accelerated nuclei and electrons is assumed to be described by the same particle distribution, here assumed to follow a power-law with an exponential cutoff of the form

$$\frac{dN}{dp} \approx \eta_{\mathrm{e},p} p^{-\Gamma_{\mathrm{p}}} \times \exp\left(-\frac{p}{p_{max}}\right) \tag{6.1}$$

where the ratio η_e/η_p gives the ratio of electrons to protons and p the momentum. The normalization and maximum energy cutoff are left as free parameters, and adjusted to fit the data. An exponential cutoff in the momentum spectra of electrons is expected when energy losses exceed the rate of energy gain from shock acceleration Webb et al. (1984). In practice, we find that we do not have sufficient spectral coverage to differentiate strongly between an exponential cutoff or a broken power law.

One-zone models for all three scenarios are presented as SED fits in figure 6.3.

Parameters are given in table 6.2, including the total energy of accelerated particles integrated above 1 GeV for protons, and above 511 keV for electrons. We adjusted the ratio of electrons-to-protons to differentiate between bremsstrahlung- and hadronic-dominated models. A ratio $\eta_{\rm e}/\eta_{\rm p} \sim 0.01$ is seen in cosmic rays at Earth around 10 GeV (Gaisser, 1991), but an even lower ratio ~ 0.001 may be expected from diffusive shock acceleration models (Reynolds, 2009). We cannot robustly constrain $\eta_{\rm e}/\eta_{\rm p}$ through our fits, so we choose characteristic values for each scenario. While the chosen parameters are not unique in their ability to fit the broadband spectrum, they are representative.

Table 6.2: One-zone model parameters

Model	index	p_{max} [GeV/c]	n_H [cm^{-3}]	B_{tot} [µG]	$\eta_{\rm e}/\eta_{\rm p}$	$W_{\rm e}$ [erg]	$W_{\rm p}$ [erg]
IC	1.76	100	0.1	2	1	1.3×10^{50}	2.1×10^{51}
brems.	1.76	19	15	24	0.1	6.4×10^{48}	3.0×10^{48}
π^0-decay	1.76	8.1	15	140	0.001	3.0×10^{49}	1.1×10^{47}

Under our simple assumptions, a single zone with a single particle distribution for both electrons and protons, we find that only hadronic models can reproduce both the observed radio and γ-ray spectra. For $\eta_{\rm e}/\eta_{\rm p} = 0.001$ we find a momentum cutoff of 10 GeV/c and a magnetic field of ~ 90 µG. Decreasing $\eta_{\rm e}/\eta_{\rm p}$ results in a higher magnetic field strength to simultaneous fit the synchrotron normalization and break in the radio. Bremsstrahlung domi-

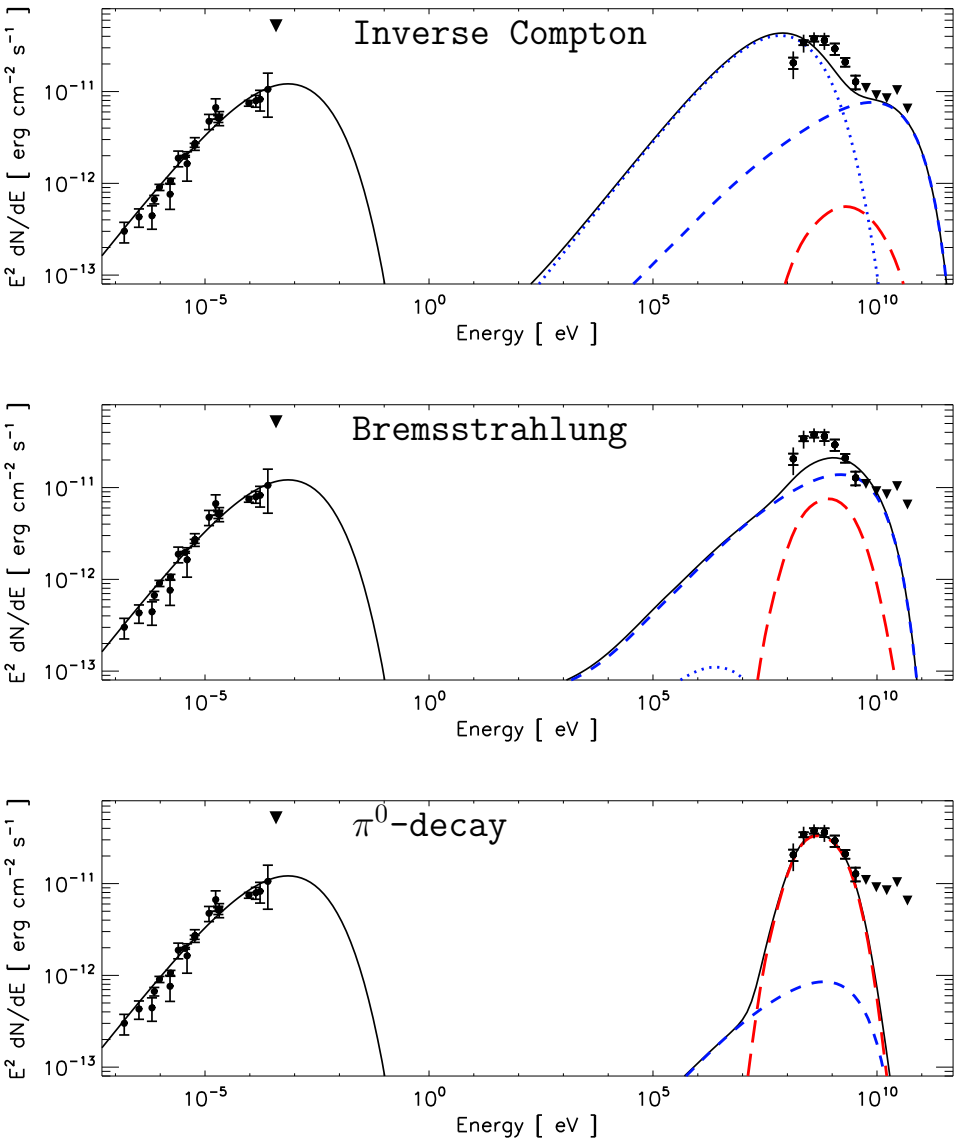

Figure 6.3: Single-zone models for which IC (top), bremsstrahlung (middle) and π^0-decay (bottom) are the dominant emission mechanism (see table 6.2 for parameters). In each model the radio data are fit with a synchrotron component, shown as a black curve. The individual contributions of π^0-decay (long dashed), bremsstrahlung (short dashed), and IC emission from CMB (dotted) are shown. The sum of the γ-ray emission is shown by the solid curve. The leptonic and hadronic components are colored blue and red, respectively.

nates over neutral pion decay when $\eta_e/\eta_p \geq 0.05$, but there is no combination of magnetic field strength and momentum cutoff that can simultaneously produce the observed SED from one electron population, as can be seen in figure 6.3. To produce a model in which IC emission dominates, we must adopt a density of ~ 0.1 cm^{-3}, which is well below gas density estimates. Therefore an IC-dominated model is unlikely, and furthermore, cannot produce a good fit to the data. The energetics of our hadronic model indicate $\sim 3 \times 10^{49}$ erg in accelerated cosmic ray protons and nuclei, which is comparable to that estimated for other old SNRs in a dense environment detected by *Fermi*.

The failure of leptonic models is largely due to an inability to fit both the observed spectral breaks in the radio and γ-ray. To explain synchrotron emission at a peak frequency ν from an electron in a magnetic field B, requires the electron have an energy (Reynolds, 2009)

$$E = 14.7 \left(\frac{\nu_{\mathrm{GHz}}}{B_{\mu\mathrm{G}}} \right). \tag{6.2}$$

For the observed radio break at ~ 6 GHz and γ-ray break at ~ 1 GeV to be explained by the same electron population requires a magnetic field of ~ 1 mG, which is far in excess of the magnetic field expected for a SNR in such an evolved stage (unless the density is very high $\gtrsim 10^4$ cm^{-3}). However, molecular clouds have a well-known multi-phase structure, so the density of HB 21 is unlikely to be uniform, and the one-zone approximation may be overly simplistic.

6.3.2 Two-zone model

As told before, one-zone model is too simplistic for HB 21, since it interacts with MCs. We therefore try to relax the single-zone assumption by modeling the radio and γ-ray emission as dominated by distinct regions. Allowing

the normalization and spectrum of the radio emission to be separately fit from γ-rays is physically motivated. Radio emission is observed from dense filaments, but globally may be dominated by diffuse gas that fills a larger volume. For SNRs W 44 and IC 443 the observed proton index from π^0-decay emission is softer than the electron index inferred from the radio spectrum (Ackermann et al., 2013). Results are reported in figure 6.4 and, for all the fit details, table 6.3.

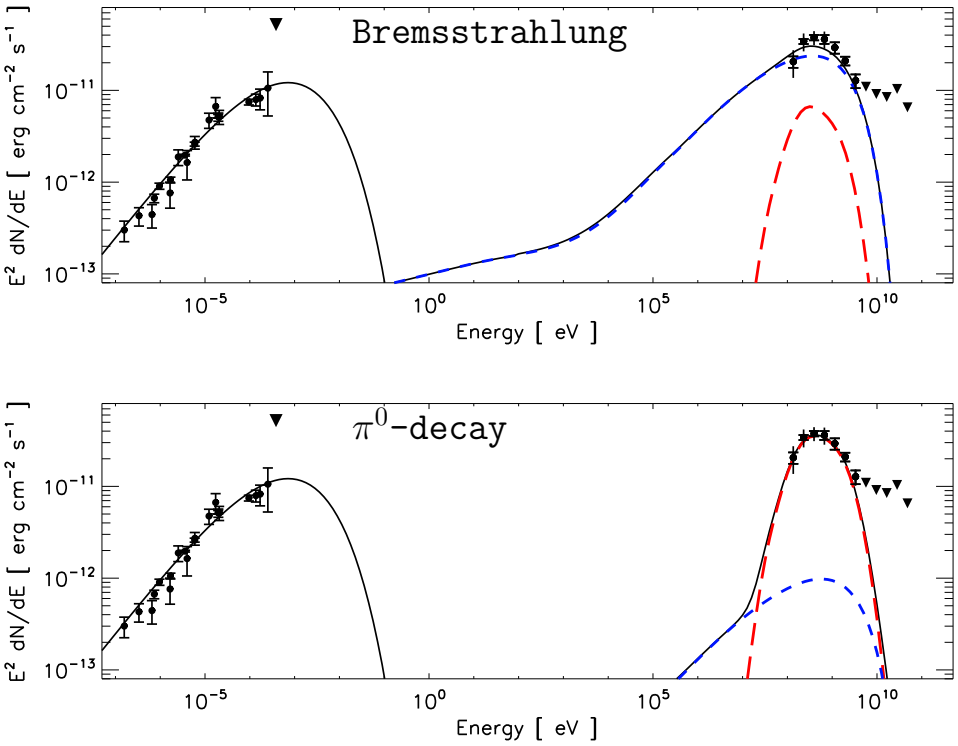

Figure 6.4: Two-zone models for which Bremsstrahlung (top) and π^0-decay (bottom) are the dominant emission mechanism, as in figure 6.3 (see table 6.3 for model parameters).

In this two-zone scenario, we found that both bremsstrahlung- and hadronic-dominated models can fit the data. The cutoff in the accelerated particle

Table 6.3: Two-zone model parameters

Model	index 1	$p_{max,1}$ [GeV/c]	index 2	$p_{max,2}$ [GeV/c]	η_e/η_p	W_e [erg]	W_p [erg]
brems.	1.76	4	1.76	8	0.1	6.7×10^{48}	3.2×10^{48}
π^0-decay	2.0	9	1.76	4	0.001	3.5×10^{49}	1.6×10^{47}

spectrum responsible for γ-rays need not match that responsible for the radio emission, due to the different physical conditions. It is also possible that high-energy CR electrons may cool in the dense filaments formed by shock-interaction with molecular clumps, or that CR protons may have largely escaped from the SNR (Aharonian and Atoyan, 1996; Malkov et al., 2011). In the latter case, we would expect that nearby clouds could be illuminated by the escaping CRs, but the geometry of the clouds in relation to HB 21 is not well known. While multi-zone models appear as feasible as single zone models, they are not well constrained due to the poor spatial resolution of the data at γ-rays and high-frequency radio. The energy in CRs in bremsstrahlung-dominated two-zone models is several times 10^{48} erg, with a comparable energy in accelerated nuclei and leptons.

6.4 Comparison with other SNRs detected by *Fermi*

HB 21 is not the only one SNR interacting with MCs detected by the *Fermi* LAT. Here we briefly discuss HB 21 in comparison to other γ-ray SNRs in order to see similarities and differences among them. The total luminosity of

HB 21 above 100 MeV at a distance of 1.7 kpc is $(3.3 \pm 0.6) \times 10^{34}$ erg s^{-1}. Other γ-ray-detected MM SNRs, such as W 44 and IC 443, have luminosities of $\sim 10^{35}$ erg s^{-1} and associated cloud masses of $> 10^4$ $M_\odot$. While the total CO line emission along the line of sight to HB 21 indicates a large cloud mass, this could be due to the Cygnus OB7 complex, which lies along the line of sight at a similar velocity to HB 21, but at a distance of only 0.8 kpc, between us and the SNR. It is therefore possible that the low luminosity of HB 21 is due to the SNR currently encountering only a relatively small reservoir of material.

Flat radio indices, as for HB 21, are observed for other γ-ray detected SNRs known to be interacting with molecular clouds, such as IC 443 and W 44. Leahy (2006) proposed two mechanisms to produce the observed flat spectrum: ionization losses due to emission from regions of high density, and low-frequency absorption by thermal electrons in the post-shock cooling regions. Alternatively, Uchiyama et al. (2010) proposed that re-acceleration takes place in the compressed cloud, resulting in a hardening of the spectrum of existing accelerated particles. Though it is likely interacting with a less-dense environment than HB 21, the latter model was shown to plausibly explain radio and γ-ray emission from SNR S147 (Katsuta et al., 2012).

HB 21 shows a cutoff or break in the γ-ray spectrum, as shown in the spectral analysis i section 5.2.5, mirroring that of the underlying particle spectrum, which is typical of middle-aged SNRs detected by the LAT (e.g. the Cygnus Loop, Katagiri et al. 2011, and W28, Abdo et al. 2010). This is in agreement with the circumstantial evidence for HB 21 itself to be a middle-aged/old remnant. Given the long timescales for radiative losses via proton-proton collision, bremsstrahlung or synchrotron losses for GeV particles, it is unlikely that such spectral curvature is produced by radiative losses.

Several mechanisms have been proposed, including runaway CRs illuminating nearby clouds (Gabici et al., 2009), the aforementioned re-acceleration in highly-compressed shocks at the interaction sites (Uchiyama et al., 2010), and magnetic damping of Alfven waves in a partially ionized medium that leads to a break in the particle spectrum (Malkov et al., 2011). All these mechanisms appear viable for the case of HB 21, and could produce different particle distributions for electrons and protons remaining in the SNR. Given the many shared similarities with other MM SNRs, HB 21 appears to be an extension of this γ-ray class to lower luminosities.

Chapter 7

Summary and future perspectives

SNRs are advocated to be the main accelerators of Galactic CRs. Proving this hypothesis is of fundamental importance for modern astronomy and astrophysics to better understand the role of CRs in the interstellar medium. One way to achieve this goal is through mwl observations of SNRs to understand which are the mechanisms and processes giving rise to the observed non-thermal emission. An interesting case is provided by SNRs interacting with molecular clouds because the escaping particle accelerated by SN shocks can interact with the surrounding material: their emission spectrum can provide further information on the CR acceleration mechanism.

In my thesis, I performed the *Fermi* LAT analysis of the region around HB 21, a MM SNR interacting with molecular clouds. I detected a significant γ-ray emission ($\sim 29\sigma$) associated with the remnant. The emission is best modeled by a disk centered at $(l, b) = (88.^{\circ}75 \pm 0.^{\circ}04, +4.^{\circ}65 \pm 0.^{\circ}06)$, with a radius $r = 1.^{\circ}19 \pm 0.^{\circ}06$, with a systematic uncertainty on the position of $\sim 0.^{\circ}25$ and on the radius of $\sim 0.^{\circ}24$, so it is well-resolved by the LAT for energies greater than 1 GeV. The γ-ray emission extends over the whole area of the non-thermal radio shell, larger than the X-ray emitting thermal core.

The emission in γ-rays may extend beyond the radio shell in a region rich of interstellar matter in the northwestern part of the SNR.

Further, the brightest γ-ray emitting region coincides with known shocked molecular clumps. Both results suggest that collisions of shock-accelerated particles with interstellar matter are responsible for the observed γ-ray emission. No spectral variations across the γ-ray-emitting region that would further support this hypothesis were detected with the current observations.

The spectrum is best modeled by a curved function, indicative of a cutoff or break in the spectrum of the accelerated particles, typical of middle-aged and old SNRs in a dense interstellar environment. The total γ-ray luminosity of HB 21 above 100 MeV is estimated to be $(3.3 \pm 0.6) \times 10^{34}$ erg s^{-1}, fainter than other SNRs interacting with molecular clouds detected by the LAT. This can be explained by the lower mass of the molecular clouds supposed to be interacting with the remnant.

Reichardt et al. (2012) recently reported a lower luminosity for HB 21. We assume a distance of 1.7 kpc, based on the arguments of Byun et al. (2006), while their work assumes a nearer distance of 0.8 kpc adopted in numerous earlier works. Taking this difference into account, our values of the 0.110 GeV flux and the luminosity of SNR HB 21 are in agreement. Even considering statistical uncertainties only, we do not find any significant evidence for spectral variations across the SNR, as suggested for cloud NW and A in their work.

We complemented the γ-ray analysis by exploiting the WMAP 7 yr observations from 23 to 93 GHz, obtaining the first detections of HB 21 at these energies.

By combining WMAP with lower-energies radio observations, we found that the radio spectral index of HB 21 steepens significantly above 10 GHz.

This spectral feature in the radio helps to constrain the relativistic electron spectrum and the allowed physical parameters in a simple non-thermal radiation models.

An IC origin of the γ-ray emission is disfavored because it would require unrealistically low interstellar densities to prevent bremsstrahlung from dominating. Decay of π^0 due to nuclei interactions can reproduce the data well. Bremsstrahlung and synchrotron emission from a single population of energetic electrons cannot reproduce both the γ-ray and radio SEDs.

Based on the most likely values for the ISM densities over the volume of the remnant, in the hadronic-dominated scenario, accelerated nuclei contribute a total energy of $\sim 3 \times 10^{49}$ erg. This is reduced to several times 10^{48} erg under a two-zone bremsstrahlung-dominated model, with a comparable energy in leptonic CRs.

The energy densities of the accelerated particles are consistent with the SNR paradigm, requiring SNRs to convert $\sim 10^{50}$ erg of the explosion energy into non-thermal nuclei and electrons.

7.1 Future perspectives

In this thesis, I evaluated also the systematic uncertainties due to the limited knowledge of the behavior of the interstellar emission model. Alternative models and the method are developed in the *Fermi* collaboration and, in this work and other articles of the *Fermi* collaboration, the new method is tested. This is a first step along the *First* Fermi *SNRs Catalog* whose work is in progress. It will collect all the SNRs detected by *Fermi*including also for all reported sources their multi-wavelength behaviour, the morphological analysis in γ-ray and their modeling.

A deeper look into the physics of particle acceleration in SNRs will be possible with the upcoming new generation of γ ray telescopes, most notably the Cherenkov Telescope Array (CTA) (Acharya and et al, 2013). The increased sensitivity of CTA is likely to lead to the discovery of a considerable number of other SNRs that are in the process of accelerating CRs in our Galaxy. The high angular resolution will allow us to measure the spectrum of γ ray emission from different regions of the same SNR in order to achieve a better description of the dependence of the acceleration process upon the environment in which acceleration takes place.

As shown in our analysis, in some SNRs there is the presence of a spectral break in the spectrum. Using data from *Fermi* and CTA, one can try to explain the origin of these spectral breaks.

Another interesting feature to study is the evolution of the γ-ray spectrum in function of the SNR environment and age: the presence of molecular clouds or dense environment can affect the evolution of SNRs.

Acknowledgements

My thanks to all the other present and former members of the Fermi LAT group in Padova, as well as to people I met in the Physics Department and the INFN section.

I would like to thank my supervisor Prof. Denis Bastieri. I would also like to express my gratitude to Luigi Tibaldo for sharing his knowledge with me and to supervise my work.

I am deeply indebted to the Fermi LAT collaboration: none of my achievements would have been possible without their huge effort to sustain the mission and the interpretation of the data. I want to thank especially the members of the Galactic group and in particular those who directly contributed to the works reported in this dissertation. I am particularly thankful to John W.Hewitt who perform the radio analysis and the non-thermal modeling on HB 21. My thanks also to Jean Ballet for reviewing the paper on HB 21.

I gratefully thank all my friends and my family for their support, encouragement and patience. To my parents who have always stood beside me, for so much my love.

Acronyms

ACD Anti-Coincidence Detector

A_{eff} effective area

BSPR Blind Search Pattern Recognition

CC Core Collapse

CSPR Calorimeter-Seeded Pettern Recognition

CAL Calorimeter

CMB Cosmic Microwave Background

CPF Charged Particles in the Field-of-View

CR cosmic ray

CSM circumstellar medium

CTA Cherenkov Telescope Array

DGE diffuse Galactic γ-ray emission

DM Dark Matter

d.o.f. degrees of freedom

DSA diffusive shock acceleration

EA effective area

EGB extragalactic γ-ray background

FoM figure of merit

FoV Field of View

GCR Galactic CR

GBM Gamma-ray Burst Monitor

GRB Gamma-ray Burst

IACT Imaging Atmospheric Cherenkov Telescope

IEM interstellar emission model

IC Inverse Compton

IRF Instrument Response function

ISRF Interstellar radiation field

IR infrared

ISM Interstellar Medium

LAT Large Area Telescope

LK Likelihood

MC Monte Carlo

MC molecular cloud

MHD magneto-hydrodynamic

MM mixed morphology

NLDSA nonlinear DSA

PC Parametric Correction

PMT photomultiplier Tube

PSF Point Spread Function

PWN Pulsar wind nebula

RMS root mean square

RSG red supergigant

RoI Region of Interest

SAA South Atlantic Anomaly

SED spectral energy distribution

SN supernova

SNR Supernova Remnant

SP Shower Profile

SRT Westerbork Synthesis Radio Telescope

SSD single-sided Silicon Strip Detectors

ST Science Tools

TKR tracker

TS Test Statistics

UHECR ultra high energy cosmic ray

UIB unidentified background

WIMP Weakly Interacting Massive Particle

WLS wavelength shifting fibers

Bibliography

A. A. Abdo, M. Ackermann, M. Ajello, et al. Fermi large area telescope measurements of the diffuse gamma-ray emission at intermediate galactic latitudes. *Phys. Rev. Lett.*, 103:251101, Dec 2009a. doi: 10.1103/PhysRevLett.103.251101. URL `http://link.aps.org/doi/10.1103/PhysRevLett.103.251101`.

A. A. Abdo, M. Ackermann, M. Ajello, et al. Fermi lat observation of diffuse gamma rays produced through interactions between local interstellar matter and high-energy cosmic rays. *The Astrophysical Journal*, 703(2):1249, 2009b. URL `http://stacks.iop.org/0004-637X/703/i=2/a=1249`.

A. A. Abdo, M. Ackermann, M. Ajello, et al. Fermi Large Area Telescope Observations of the Supernova Remnant W28 (G6.4-0.1). *ApJ*, 718:348–356, July 2010. doi: 10.1088/0004-637X/718/1/348.

A. A. Abdo, M. Ajello, A. Allafort, et al. Fermi Large Area Telescope Second Gamma-ray Pulsars Catalog. *ApJs*, 2013. in press (2PC).

M. Ackermann, M. Ajello, A. Allafort, et al. A Cocoon of Freshly Accelerated Cosmic Rays Detected by Fermi in the Cygnus Superbubble. *Science*, 334:1103–, November 2011. doi: 10.1126/science.1210311.

M. Ackermann, M. Ajello, A. Albert, et al. The Fermi Large Area Telescope on Orbit: Event Classification, Instrument Response Functions, and Calibration. *ApJs*, 203:4, November 2012a. doi: 10.1088/0067-0049/203/1/4.

M. Ackermann, M. Ajello, A. Allafort, et al. In-flight measurement of the absolute energy scale of the Fermi Large Area Telescope. *Astroparticle Physics*, 35:346–353, January 2012b. doi: 10.1016/j.astropartphys.2011.10.007.

M. Ackermann, M. Ajello, A. Allafort, et al. The cosmic-ray and gas content of the Cygnus region as measured in γ-rays by the Fermi Large Area Telescope. *A&A*, 538:A71, February 2012c. doi: 10.1051/0004-6361/201117539.

M. Ackermann, M. Ajello, W. B. Atwood, et al. Fermi-LAT Observations of the Diffuse γ-Ray Emission: Implications for Cosmic Rays and the Interstellar Medium. *ApJ*, 750:3, May 2012d. doi: 10.1088/0004-637X/750/1/3.

M. Ackermann, M. Ajello, A. Allafort, et al. Detection of the Characteristic Pion-Decay Signature in Supernova Remnants. *Science*, 339:807–811, February 2013. doi: 10.1126/science.1231160.

O. Adriani, G. C. Barbarino, G. A. Bazilevskaya, et al. An anomalous positron abundance in cosmic rays with energies 1.5-100GeV. *Nature*, 458:607–609, April 2009. doi: 10.1038/nature07942.

F. Aharonian, A. G. Akhperjanian, A. R. Bazer-Bachi, et al. H.E.S.S. Observations of the Supernova Remnant RX J0852.0-4622: Shell-Type Morphology and Spectrum of a Widely Extended Very High Energy Gamma-Ray Source. *ApJ*, 661:236–249, May 2007. doi: 10.1086/512603.

F. A. Aharonian. *Very High Energy Cosmic Gamma Radiation: a Crucial Window on the Extreme Universe*. World Scientific Publishing, 2004.

F. A. Aharonian and A. M. Atoyan. On the emissivity of $\pi\hat{}0\hat{}$-decay gamma radiation in the vicinity of accelerators of galactic cosmic rays. *A&A*, 309: 917–928, May 1996.

E. Amato and P. Blasi. Non-linear particle acceleration at non-relativistic shock waves in the presence of self-generated turbulence. *MNRAS*, 371: 1251–1258, September 2006. doi: 10.1111/j.1365-2966.2006.10739.x.

B. Aschenbach. Discovery of a young nearby supernova remnant. *Nature*, 396:141–142, November 1998. doi: 10.1038/24103.

W. B. Atwood, A. A. Abdo, M. Ackermann, et al. The Large Area Telescope on the Fermi Gamma-Ray Space Telescope Mission. *ApJ*, 697:1071–1102, June 2009. doi: 10.1088/0004-637X/697/2/1071.

W. I. Axford, E. Leer, and G. Skadron. The acceleration of cosmic rays by shock waves. In *International Cosmic Ray Conference*, volume 11 of *International Cosmic Ray Conference*, pages 132–137, 1977.

M. G. Baring. Diffusive Shock Acceleration : the Fermi Mechanism. In Y. Giraud-Heraud and J. Tran Thanh van, editors, *Very High Energy Phenomena in the Universe; Moriond Workshop*, page 97, 1997.

M. G. Baring, D. C. Ellison, and F. C. Jones. The injection and acceleration of particles in oblique shocks - A unified Monte Carlo description. *ApJ*, 409:327–332, May 1993. doi: 10.1086/172666.

A. R. Bell. The acceleration of cosmic rays in shock fronts. I. *MNRAS*, 182: 147–156, January 1978.

R. D. Blandford and J. P. Ostriker. Particle acceleration by astrophysical shocks. *ApJl*, 221:L29–L32, April 1978. doi: 10.1086/182658.

P. Blasi. Cosmic Ray Acceleration in Supernova Remnants. In S. Giani, C. Leroy, and P. G. Rancoita, editors, *Cosmic Rays for Particle and Astroparticle Physics*, pages 493–506, June 2011. doi: 10.1142/9789814329033_0061.

P. Blasi. The Origin of Galactic Cosmic Rays. *ArXiv e-prints*, November 2013.

R. C. Bohlin, B. D. Savage, and J. F. Drake. A survey of interstellar H I from L-alpha absorption measurements. II. *ApJ*, 224:132–142, August 1978. doi: 10.1086/156357.

D.-Y. Byun, B.-C. Koo, K. Tatematsu, and K. Sunada. Interaction between the Supernova Remnant HB 21 and Molecular Clouds. *ApJ*, 637:283–295, January 2006. doi: 10.1086/498232.

D. Caprioli, P. Blasi, E. Amato, and M. Vietri. Dynamical Effects of Self-Generated Magnetic Fields in Cosmic-Ray-modified Shocks. *ApJl*, 679: L139–L142, June 2008. doi: 10.1086/589505.

G. L. Case and D. Bhattacharya. A New Sigma -D Relation and Its Application to the Galactic Supernova Remnant Distribution. *ApJ*, 504:761, September 1998. doi: 10.1086/306089.

J. M. Cordes and T. J. W. Lazio. NE2001.I. A New Model for the Galactic Distribution of Free Electrons and its Fluctuations. *ArXiv Astrophysics e-prints*, July 2002.

T. M. Dame and P. Thaddeus. A wide-latitude CO survey of molecular clouds in the northern Milky Way. *ApJ*, 297:751–765, October 1985. doi: 10.1086/163573.

T. M. Dame and P. Thaddeus. A Molecular Spiral Arm in the Far Outer Galaxy. *ApJl*, 734:L24, June 2011. doi: 10.1088/2041-8205/734/1/L24.

T. M. Dame, D. Hartmann, and P. Thaddeus. The Milky Way in Molecular Clouds: A New Complete CO Survey. *ApJ*, 547:792–813, February 2001. doi: 10.1086/318388.

F. de Palma, T. J. Brandt, G. Johannesson, L. Tibaldo, and for the Fermi LAT collaboration. A Method for Exploring Systematics Due to Galactic Interstellar Emission Modeling: Application to the Fermi LAT SNR Catalog. *ArXiv e-prints*, April 2013.

C. D. Dermer. Secondary production of neutral pi-mesons and the diffuse galactic gamma radiation. *A&A*, 157:223–229, March 1986.

C. D. Dermer. The Extragalactic γ Ray Background. In S. Ritz, P. Michelson, and C. A. Meegan, editors, *The First GLAST Symposium*, volume 921 of *American Institute of Physics Conference Series*, pages 122–126, July 2007. doi: 10.1063/1.2757282.

C. D. Dermer, J. D. Finke, R. J. Murphy, et al. On the Physics Connecting Cosmic Rays and Gamma Rays: Towards Determining the Interstellar Cosmic Ray Spectrum. *ArXiv e-prints*, March 2013.

L O'C Drury. An introduction to the theory of diffusive shock acceleration of energetic particles in tenuous plasmas. *Reports on Progress in Physics*, 46 (8):973, 1983. URL `http://stacks.iop.org/0034-4885/46/i=8/a=002`.

R. Enomoto, T. Tanimori, T. Naito, et al. The acceleration of cosmic-ray protons in the supernova remnant RX J1713.7-3946. *Nature*, 416:823–826, April 2002. doi: 10.1038/416823a.

J. A. Esposito, S. D. Hunter, G. Kanbach, and P. Sreekumar. EGRET Observations of Radio-bright Supernova Remnants. *ApJ*, 461:820, April 1996. doi: 10.1086/177104.

S. Gabici, F. A. Aharonian, and S. Casanova. Broad-band non-thermal emission from molecular clouds illuminated by cosmic rays from nearby supernova remnants. *MNRAS*, 396:1629–1639, July 2009. doi: 10.1111/j.1365-2966.2009.14832.x.

T. K. Gaisser, R. J. Protheroe, and T. Stanev. Gamma-Ray Production in Supernova Remnants. *ApJ*, 492:219, January 1998. doi: 10.1086/305011.

T.K. Gaisser. *Cosmic Rays and Particle Physics*. Cambridge University Press, 1991. ISBN 9780521339315.

X. Y. Gao, J. L. Han, W. Reich, et al. A Sino-German $\lambda 6$ cm polarization survey of the Galactic plane. V. Large supernova remnants. *A&A*, 529: A159, May 2011. doi: 10.1051/0004-6361/201016311.

D. A. Green. A revised Galactic supernova remnant catalogue. *Bulletin of the Astronomical Society of India*, 37:45–61, March 2009.

I. A. Grenier, J.-M. Casandjian, and R. Terrier. Unveiling Extensive Clouds of Dark Gas in the Solar Neighborhood. *Science*, 307:1292–1295, February 2005. doi: 10.1126/science.1106924.

J. W. Hewitt, M.-H. Grondin, M. Goumard-Lemoine, et al. Fermi LAT and WMAP Observations of the Puppis A SNR. *ApJ*, 2012. in print.

L. E. Hill. Observations of the supernova remnant HB21 at 1.4 GHz. *MNRAS*, 169:59–70, October 1974.

J. C. Houck and G. E. Allen. Models for Nonthermal Photon Spectra. *ApJs*, 167:26–39, November 2006. doi: 10.1086/507951.

J. C. Houck and L. A. Denicola. ISIS: An Interactive Spectral Interpretation System for High Resolution X-Ray Spectroscopy. In N. Manset, C. Veillet, and D. Crabtree, editors, *Astronomical Data Analysis Software and Systems IX*, volume 216 of *Astronomical Society of the Pacific Conference Series*, page 591, 2000.

Y.-L. Huang and P. Thaddeus. Molecular clouds and supernova remnants in the outer galaxy. *ApJ*, 309:804–821, October 1986. doi: 10.1086/164649.

G. H. Janssen, B. W. Stappers, R. Braun, et al. Discovery and timing of the first 8gr8 Cygnus survey pulsars. *A&A*, 498:223–231, April 2009. doi: 10.1051/0004-6361/200811482.

N. Jarosik, C. L. Bennett, J. Dunkley, et al. Seven-year Wilkinson Microwave Anisotropy Probe (WMAP) Observations: Sky Maps, Systematic Errors, and Basic Results. *ApJs*, 192:14, February 2011. doi: 10.1088/0067-0049/192/2/14.

F. C. Jones. Calculated Spectrum of Inverse-Compton-Scattered Photons. *Physical Review*, 167:1159–1169, March 1968. doi: 10.1103/PhysRev.167.1159.

P. M. W. Kalberla, W. B. Burton, D. Hartmann, et al. The Leiden/Argentine/Bonn (LAB) Survey of Galactic HI. Final data release of

the combined LDS and IAR surveys with improved stray-radiation corrections. *A&A*, 440:775–782, September 2005. doi: 10.1051/0004-6361:20041864.

T. Kamae, T. Abe, and T. Koi. Diffractive Interaction and Scaling Violation in pp$\rightarrow \pi^0$ Interaction and GeV Excess in Galactic Diffuse Gamma-Ray Spectrum of EGRET. *ApJ*, 620:244–256, February 2005. doi: 10.1086/426935.

T. Kamae, N. Karlsson, T. Mizuno, T. Abe, and T. Koi. Parameterization of γ, $e^{+/-}$, and Neutrino Spectra Produced by p-p Interaction in Astronomical Environments. *ApJ*, 647:692–708, August 2006. doi: 10.1086/505189.

H. Kang and T. W. Jones. Self-similar evolution of cosmic-ray-modified quasi-parallel plane shocks. *Astroparticle Physics*, 28:232–246, October 2007. doi: 10.1016/j.astropartphys.2007.05.007.

H. Kang, P. P. Edmon, and T. W. Jones. Nonthermal Radiation from Cosmic-Ray Modified Shocks. *ApJ*, 745:146, February 2012. doi: 10.1088/0004-637X/745/2/146.

H Katagiri, L Tibaldo, J Ballet, et al. Fermi Large Area Telescope Observations of the Cygnus Loop Supernova Remnant. *The Astrophysical Journal*, 741:44, November 2011.

J. Katsuta, Y. Uchiyama, T. Tanaka, et al. Fermi Large Area Telescope Observation of Supernova Remnant S147. *ApJ*, 752:135, June 2012. doi: 10.1088/0004-637X/752/2/135.

B.-C. Koo and C. Heiles. A survey of H I 21 centimeter emission lines toward supernova remnants. *ApJ*, 382:204–222, November 1991. doi: 10.1086/170709.

Bon-Chul Koo, Jeonghee Rho, William T Reach, JaeHoon Jung, and Jeffrey G Mangum. Shocked Molecular Gas in the Supernova Remnant HB 21. *ApJ*, 552(1):175–188, May 2001.

R. Kothes, K. Fedotov, T. J. Foster, and B. Uyanıker. A catalogue of Galactic supernova remnants from the Canadian Galactic plane survey. I. Flux densities, spectra, and polarization characteristics. *A&A*, 457:1081–1093, October 2006. doi: 10.1051/0004-6361:20065062.

K. Koyama, K. Kinugasa, K. Matsuzaki, et al. Discovery of Non-Thermal X-Rays from the Northwest Shell of the New SNR RX J1713.7-3946: The Second SN 1006? *Publications of the Astronomical Society of Japan*, 49: L7–L11, June 1997.

G. F. Krymskii. A regular mechanism for the acceleration of charged particles on the front of a shock wave. *Akademiia Nauk SSSR Doklady*, 234:1306–1308, June 1977.

J. Lande, M. Ackermann, A. Allafort, et al. Search for Spatially Extended Fermi Large Area Telescope Sources Using Two Years of Data. *ApJ*, 756: 5, September 2012. doi: 10.1088/0004-637X/756/1/5.

J. S. Lazendic and P. O. Slane. Enhanced Abundances in Three Large-Diameter Mixed-Morphology Supernova Remnants. *ApJ*, 647:350–366, August 2006. doi: 10.1086/505380.

D. A. Leahy. Radio Spectral Index Variations in HB 21. *ApJ*, 647:1125–1130, August 2006. doi: 10.1086/505521.

D. A. Leahy and R. S. Roger. Radio Spectral Index Variations in the Cygnus Loop. *ApJ*, 505:784–792, October 1998. doi: 10.1086/306212.

M. S. Longair. *High Energy Astrophysics*. Cambridge university press, third edition, 2011.

D. R. Lorimer, A. J. Faulkner, A. G. Lyne, et al. The Parkes Multibeam Pulsar Survey - VI. Discovery and timing of 142 pulsars and a Galactic population analysis. *MNRAS*, 372:777–800, October 2006. doi: 10.1111/j.1365-2966.2006.10887.x.

M. A. Malkov, P. H. Diamond, and R. Z. Sagdeev. Mechanism for spectral break in cosmic ray proton spectrum of supernova remnant W44. *Nature Communications*, 2:194, February 2011. doi: 10.1038/ncomms1195.

J. R. Mattox, D. L. Bertsch, J. Chiang, et al. The Likelihood Analysis of EGRET Data. *ApJ*, 461:396–407, April 1996. doi: 10.1086/177068.

F Mavromatakis, E M Xilouris, and P Boumis. The optical properties of the G89.0+4.7 (HB 21) supernova remnant. *A&A*, 461(3):991–997, January 2007.

P. L. Nolan, A. A. Abdo, M. Ackermann, et al. Fermi Large Area Telescope Second Source Catalog. *ApJs*, 199:31, April 2012. doi: 10.1088/0067-0049/199/2/31.

T. G. Pannuti, J. Rho, K. J. Borkowski, and P. B. Cameron. Mixed-morphology Supernova Remnants in X-rays: Isothermal Plasma in HB21 and Probable Oxygen-rich Ejecta in CTB 1. *The Astronomical Journal*, 140:1787–1805, December 2010. doi: 10.1088/0004-6256/140/6/1787.

G. Pivato, J. W. Hewitt, L. Tibaldo, et al. Fermi LAT and WMAP Observations of the Supernova Remnant HB 21. *ApJ*, 779:179, December 2013. doi: 10.1088/0004-637X/779/2/179.

T. A. Porter, S. W. Digel, I. A. Grenier, and et al. The Diffuse Galactic Gamma-Ray Emission Model for GLAST LAT. *International Cosmic Ray Conference*, 2:521–524, 2008.

R. Protassov, D. A. van Dyk, A. Connors, V. L. Kashyap, and A. Siemiginowska. Statistics, Handle with Care: Detecting Multiple Model Components with the Likelihood Ratio Test. *ApJ*, 571:545–559, May 2002. doi: 10.1086/339856.

I. Reichardt, E. de Oña-Wilhelmi, J. Rico, and R. Yang. An extended source of GeV gamma rays coincident with the supernova remnant HB 21. *A&A*, 546:A21, October 2012. doi: 10.1051/0004-6361/201219947.

S. P. Reynolds. Models of Synchrotron X-Rays from Shell Supernova Remnants. *ApJ*, 493:375, January 1998. doi: 10.1086/305103.

S. P. Reynolds. Supernova Remnants at High Energy. *ARA&A*, 46:89–126, September 2008. doi: 10.1146/annurev.astro.46.060407.145237.

S. P. Reynolds. Synchrotron-Loss Spectral Breaks in Pulsar-Wind Nebulae and Extragalactic Jets. *ApJ*, 703:662–670, September 2009. doi: 10.1088/0004-637X/703/1/662.

I. S. Shklovskii. On the Nature of the Crab Nebulas Optical Emission. *Doklady Akad. Nauk SSSR*, 90:983, 1953.

P. Slane, B. M. Gaensler, T. M. Dame, et al. Nonthermal X-Ray Emission from the Shell-Type Supernova Remnant G347.3-0.5. *ApJ*, 525:357–367, November 1999. doi: 10.1086/307893.

P. Slane, J. P. Hughes, R. J. Edgar, et al. RX J0852.0-4622: Another Non-

thermal Shell-Type Supernova Remnant (G266.2-1.2). *ApJ*, 548:814–819, February 2001. doi: 10.1086/319033.

D. A. Smith, L. Guillemot, F. Camilo, et al. Pulsar timing for the Fermi gamma-ray space telescope. *A&A*, 492:923–931, December 2008. doi: 10.1051/0004-6361:200810285.

F. W. Stecker. Cosmic gamma rays. *NASA Special Publication*, 249, 1971.

A. W. Strong and I. V. Moskalenko. Propagation of Cosmic-Ray Nucleons in the Galaxy. *ApJ*, 509:212–228, December 1998. doi: 10.1086/306470.

A. W. Strong, I. V. Moskalenko, and V. S. Ptuskin. Cosmic-Ray Propagation and Interactions in the Galaxy. *Annual Review of Nuclear and Particle Science*, 57:285–327, November 2007. doi: 10.1146/annurev.nucl.57.090506.123011.

S. J. Sturner, J. G. Skibo, C. D. Dermer, and J. R. Mattox. Temporal Evolution of Nonthermal Spectra from Supernova Remnants. *ApJ*, 490:619, December 1997. doi: 10.1086/304894.

J. H. Taylor and J. M. Cordes. Pulsar distances and the galactic distribution of free electrons. *ApJ*, 411:674–684, July 1993. doi: 10.1086/172870.

Y. Uchiyama, R. D. Blandford, S. Funk, H. Tajima, and T. Tanaka. Gamma-ray Emission from Crushed Clouds in Supernova Remnants. *ApJl*, 723:L122–L126, November 2010. doi: 10.1088/2041-8205/723/1/L122.

M. Vietri. *Astrofisica delle alte energie*. Bollati Boringhieri, 2006.

A. Vladimirov, D. C. Ellison, and A. Bykov. Nonlinear Diffusive Shock Acceleration with Magnetic Field Amplification. *ApJ*, 652:1246–1258, December 2006. doi: 10.1086/508154.

W. Voges, B. Aschenbach, T. Boller, et al. The ROSAT all-sky survey bright source catalogue. *A&A*, 349:389–405, September 1999.

H. J. Völk, E. G. Berezhko, and L. T. Ksenofontov. Magnetic field amplification in Tycho and other shell-type supernova remnants. *A&A*, 433: 229–240, April 2005. doi: 10.1051/0004-6361:20042015.

R.-B. Wang and K. Hirotani. Death Line of Gamma-Ray Pulsars with Outer Gaps. *ApJ*, 736:127, August 2011. doi: 10.1088/0004-637X/736/2/127.

G. M. Webb, L. O. Drury, and P. Biermann. Diffusive shock acceleration of energetic electrons subject to synchrotron losses. *A&A*, 137:185–201, August 1984.

J. L. Weiland, N. Odegard, R. S. Hill, et al. Seven-year Wilkinson Microwave Anisotropy Probe (WMAP) Observations: Planets and Celestial Calibration Sources. *ApJs*, 192:19, February 2011. doi: 10.1088/0067-0049/192/2/19.

K. C. Westfold. The Polarization of Synchrotron Radiation. *ApJ*, 130:241, July 1959. doi: 10.1086/146713.

S. S. Wilks. The Large-Sample Distribution of the Likelihood Ratio for Testing Composite Hypotheses. *The Annals of Mathematical Statistics*, 9(1): pp. 60–62, 1938. ISSN 00034851. URL `http://www.jstor.org/stable/2957648`.

F. Yusef-Zadeh, M. Wardle, J. Rho, and M. Sakano. OH (1720 MHz) Masers and Mixed-Morphology Supernova Remnants. *ApJ*, 585:319–323, March 2003. doi: 10.1086/345932.

Juan Zhang, Qiang Yuan, and Xiao-Jun Bi. Galactic diffuse gamma raysre-calculation based on new measurements of the cosmic electron spectrum. *The Astrophysical Journal*, 720(1):9, 2010. URL `http://stacks.iop.org/0004-637X/720/i=1/a=9`.

Contents